

MECHANISMS THAT CONTROL THE LATITUDE
OF JET STREAMS AND SURFACE WESTERLIES

GANG CHEN

A DISSERTATION
PRESENTED TO THE FACULTY
OF PRINCETON UNIVERSITY
IN CANDIDACY FOR THE DEGREE
OF DOCTOR OF PHILOSOPHY

RECOMMENDED FOR ACCEPTANCE
BY THE PROGRAM IN
ATMOSPHERIC AND OCEANIC SCIENCES

SEPTEMBER 2007

© Copyright by Gang Chen, 2007.

All Rights Reserved

Abstract

Observations and climate models have shown that the extratropical zonal mean zonal winds experience a latitudinal shift with an equivalent barotropic structure from surface westerlies to upper tropospheric jets, in response to several major climate forcings including increasing greenhouse gases, stratospheric ozone depletion, volcanic forcing, and the ENSO (El Niño and Southern Oscillation) cycle. We have performed a number of idealized model experiments to study the mechanisms for these jet movements, using more generic forcings such as changes in surface friction and prescribed zonal torques. Our studies suggest that these jet movements in idealized models and possibly during climate change can be explained by quasi-linear Rossby wave propagation in the upper troposphere and wave activity absorption near the critical latitudes, where the eastward propagation speed of eddies equals the background zonal mean zonal wind.

We first vary the strength of surface friction in an idealized dry model of the troposphere. The midlatitude jet is displaced poleward when the surface friction is reduced. If the friction on the zonal mean flow is reduced instantaneously, the response reveals two distinctive adjustment time scales. In the fast adjustment over the first 10-20 days, there is an increase in the barotropic component of zonal winds and a substantial decrease in the eddy kinetic energy; the shift in the surface westerlies and jet latitude occurs in a slower adjustment. The space-time eddy momentum flux spectra suggest that the key to the shift is a poleward movement in the subtropical critical latitude associated with the faster eastward phase speeds in the dominant midlatitude eddies.

We further explore the tropospheric jet shift to a prescribed zonal torque in a model with high stratospheric resolution. The jet moves in opposite directions for the torques on the jet's equatorward and poleward flanks in the troposphere. This can be explained by different ways of modifying the critical latitudes of wave activity

absorption. However, the jet moves in the same direction for the torque in the extratropical stratosphere irrespective of the latitude of the torque. The stratospheric eddies play the key role in transferring zonal wind anomalies downwards into the troposphere. We argue that these stratospheric zonal wind anomalies can affect the tropospheric jet by altering the eastward propagation of tropospheric eddies.

The tropospheric eddies display a trend towards faster eastward phase speeds in the observations and model simulations for the late 20th century, and in the model projections for the 21st century. We argue that the increased lower stratospheric or upper tropospheric zonal winds, associated with stratospheric ozone depletion or global warming, can be sufficient to increase eddy phase speeds so as to shift the circulation polewards. The trend is very similar in structure to the internal inter-annual variability due to atmospheric eddy-mean flow interactions, rather than the SST-forced variability during the ENSO cycle. This suggests that the observed and simulated shifts of surface westerlies can be more related to the processes associated with the extratropical internal variability such as the variations in the stratospheric polar vortex, rather than those for the tropical-extratropical interactions.

Acknowledgements

First and foremost, I would like to thank my thesis advisor, Isaac Held, whose door was always open whenever I needed any guidance in my research. I especially enjoyed plenty of personal conversations, from which I learned considerably from his deep and comprehensive understandings in climate science and atmospheric dynamics. I am also very thankful for his numerous helps on my scientific writings and valuable suggestions to improve this thesis.

Next, I thank the members on my general and thesis committee, Isidoro Orlanski, Geoff Vallis, Steve Garner and Lorenzo Polvani (Columbia) for their advices on various stages of my study in Princeton. In particular, I appreciate greatly the discussions with my thesis reader, Isidoro Orlanski, for sorting out some challenging questions in this thesis. I am very grateful to Walter Robinson (UIUC), Paul Kushner (U. Toronto) and Gabriel Lau for sharing their wisdom and experience on this research subject. I also acknowledge academic advices from directors of graduate studies in AOS program in the past five years, George Philander, Anand Gnanadesikan, and Geoff Vallis.

I have also benefitted from postdocs and fellow graduate students in AOS and GFDL community. I learned a lot of practical statistical techniques and details of the most comprehensive climate model and real atmosphere (that often are not covered in class) from Jian Lu, and the latest development in theories of baroclinic adjustment and geostrophic turbulence from Pablo Zurita-Gotor. I was fortunate to know two role models of senior graduate students, Dargan Frierson and Edwin Gerber, who were always generous in giving out suggestions in my study and postdoc job hunting. Also, I enjoyed frequent interactions with other postdocs and students, Zhang shaoqing, Huang xianglei, Tian Baijun, Yang huiyan, Seoung Soo Lee, Huang Yi, and so on.

Last, I would like to thank my parents and my sister who always believe in me and support my study in Princeton.

Contents

Abstract	iii
Acknowledgements	v
1 Introduction	1
1.1 Motivations	1
1.2 Wave propagation and the associated zonal momentum transfer	3
1.3 Various viewpoints on the jet movements during climate change	9
1.4 Outline	12
2 The Importance of Barotropic Shears in the Troposphere	14
2.1 Introduction	14
2.2 Mean drag versus eddy drag	18
2.3 The transient response to a change in the mean drag	24
2.4 The eddy flux cospectra and the critical latitude shift	28
2.5 A shallow water model of upper troposphere	34
2.6 Conclusions and Discussions	43
2.7 Appendix A: The atmospheric energetics	46
2.8 Appendix B: The shallow water model of upper troposphere	47
2.8.1 The conceptual model	47
2.8.2 The numerical model	50
2.9 Appendix C: The space-time spectral analysis	54

3	The Downward Influence of the Stratosphere	57
3.1	Introduction	57
3.2	The idealized dry model	61
3.2.1	The model configuration	61
3.2.2	The control simulation	62
3.3	A sensitivity study	63
3.4	Response to the tropospheric forcing	68
3.5	Response to the stratospheric forcing	78
3.6	The jet response to the orographic GWD parameterization	84
3.7	Conclusions and discussions	89
3.8	Appendix A: The Eliassen-Palm (EP) fluxes	93
3.9	Appendix B: The Empirical Orthogonal Function (EOF) analysis	94
4	Observations and Climate Models	96
4.1	Introduction	96
4.2	Reanalysis and models	99
4.3	The linear trends in the late 20th century	100
4.3.1	Reanalysis data	100
4.3.2	GFDL climate models	103
4.4	The interannual variability	109
4.4.1	The ENSO-induced variability	110
4.4.2	The internal variability	121
4.5	The projected trends in the 21th century	128
4.6	Conclusions and Discussions	135
5	Conclusions	137

Chapter 1

Introduction

1.1 Motivations

The tropospheric jet streams are one of most prominent features in the global atmospheric circulation. The jet streams are intense westerly (eastward) winds meandering about nearly zonal axes in the upper troposphere. In particular, the jets are characterized by strong vertical and meridional wind shears: the vertical shears provide an optimal environment for cyclogenesis through baroclinic instability, and the meridional shears form a narrow jet axis and steer the cyclonic storm systems and the associated poleward heat and moisture transports. The jet streams can be roughly divided into the subtropical jet and polar front jet. The former can be understood as generated by the poleward flow in the Hadley cell; the latter results from the heat and momentum transport by cyclonic eddies in the polar front regions, and the two types of jets are often merged. In the latitudes of the polar front jet or the merged subtropical and polar front jet, westerly winds are found at the surface, which play an important role in driving the underlying oceanic circulation.

The latitudinal movements of jet streams are highly correlated with major large-scale patterns of climate variability. El Niño episodes are associated with an equa-

torward shift of the East Asian jet stream (e.g. Trenberth et al., 1998). The North Atlantic Oscillation is characterized by changes in the intensity and location of the North Atlantic jet stream (e.g. Marshall et al., 2002). The leading annular modes of the extratropical circulation in both hemispheres represent the north-south vacillation of the midlatitude jets (e.g. Thompson and Wallace, 2000).

An understanding of the factors that control the latitude of the surface westerlies and tropospheric jets has risen to central importance in climate theory, due to observations of a poleward shift in recent years in the Southern Hemisphere (e.g. Thompson and Solomon, 2002) and the prediction of poleward movement in both hemispheres in response to global warming in the future (e.g. Fyfe et al., 1999; Kushner et al., 2001; Miller et al., 2006). This poleward shift, accompanied by zonal wind changes of an equivalent barotropic structure in the troposphere, is often referred to as a shift towards a more positive phase of an annular mode (e.g. Thompson et al., 2000). A recent study with satellite observations has confirmed that the tropospheric jet streams in both hemispheres have moved poleward for about 1 degree of latitude in the last 27 years (Fu et al., 2006). Idealized models generate poleward shifts in the westerlies in response to increases in stratospheric temperature gradients (Polvani and Kushner, 2002; Kushner and Polvani, 2004; Haigh et al., 2005), increases in surface temperature gradients (Son and Lee, 2005), increases in water vapor and the associated latent heating (Frierson et al., 2006), and increases in the height of the tropopause (Williams, 2006). Comprehensive GCM experiments also generate poleward shifts in response to the development of the ozone hole in the Southern hemisphere (Gillett and Thompson, 2003), and in response to stratospheric cooling/tropospheric heating (Rind et al., 2005a). An understanding of the observed and projected shifts in the westerlies will require critical evaluation of models of all these effects.

This poleward shift of upper-tropospheric jets and surface westerlies can have a serious impact on global climate, including midlatitude precipitation, polar ice sheets,

and oceanic currents. As the jet streams steer the extratropical cyclonic storm systems, the poleward jet shift can redistribute precipitation in the midlatitudes (e.g. Yin, 2005). The positive trend in the Southern Hemisphere annular mode is associated with warming on the Antarctic Peninsula and cooling in the interior of Antarctic continent (e.g. Thompson and Solomon, 2002). Also, the North Atlantic Oscillation displays a significant correlation with the variability of sea ice transport through the Fram Strait (e.g. Kwok and Rothrock, 1999). Meanwhile, Fyfe and Saenko (2005) suggest that the surface westerly shift induced by anthropogenic forcing explains about half of the observed poleward shift of the Antarctic Circumpolar Current seen since the 1950s. Furthermore, many puzzling features of the glacial-interglacial CO₂ cycles may be explained by the poleward shifts of westerlies and the associated wind driven circulations in response to increasing atmospheric CO₂ concentration (Toggweiler et al., 2006).

1.2 Wave propagation and the associated zonal momentum transfer

We first describe the picture of baroclinic wave propagation in the extratropics that is critical to the generation of the midlatitude jet. Figure 1.1 shows the observed December-March and zonally averaged zonal wind and Eliassen Palm (EP) flux divergence (Edmon et al., 1980). The tropospheric zonal winds are characterized by upper tropospheric westerly jets, surface westerlies in the midlatitudes and surface easterlies in the tropics. The distribution of surface winds is crucial for the budget of global atmospheric angular momentum, which is transferred into the atmosphere in the tropics and lost to the Earth surface in the midlatitudes. The EP flux vectors represent the direction of wave propagation; the resulting zonal momentum transfer is in the opposite direction to Rossby wave like disturbance. The figure shows that baro-

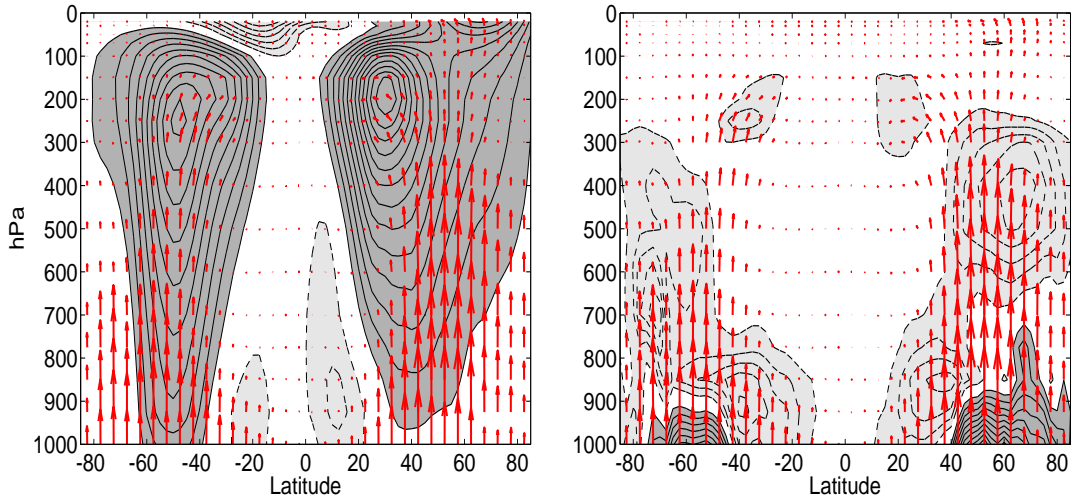


Figure 1.1: The December-March and zonally averaged (left) zonal wind and (right) Eliassen Palm flux divergence averaged from 1959-2002 in ERA-40. The contour intervals are (left) 3 m/s and (right) 2 m/s/day. The red arrows denote the EP vectors. The dark (light) shading denotes positive (negative) values.

clinic waves diverge from near the surface in midlatitudes and propagate upwards, and, despite a large amount of wave activity absorption in the middle troposphere, some waves are deflected equatorward in the upper troposphere (Edmon et al., 1980). The equatorward wave propagation is converged and absorbed in the subtropical upper troposphere in both hemispheres, decelerating the subtropical zonal winds and thus transferring angular momentum into the extratropics. As such, the zonal wind structures and the jet latitude can be thought of as being determined by the sources and sinks of wave propagation in the upper troposphere.

To quantify the wave propagation and associated zonal momentum transfer, we describe a conceptual barotropic model for the upper troposphere (Held and Phillips, 1987, 1990; Held, 2000; Vallis, 2006). The basic picture is depicted in Fig. 1.2. Rossby waves can be thought of as being randomly stirred by baroclinic instability in the midlatitudes, and propagate meridionally into the subtropical and subpolar regions, where the waves become nonlinear and result in the absorption of wave activity. The wave activity source and sink are related to the zonal wind acceleration

in the midlatitudes, and deceleration in the subtropical and subpolar regions. The quantitative relationship is shown as follows.

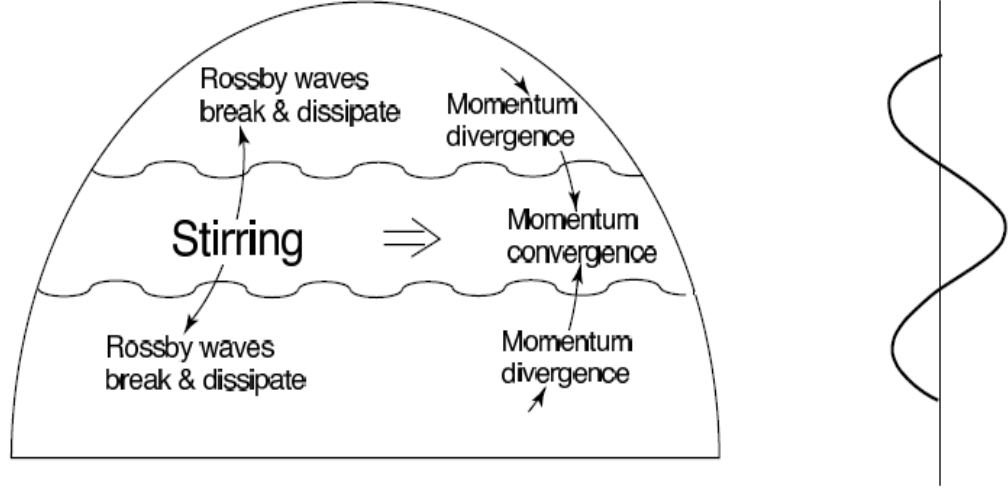


Figure 1.2: A schematic diagram for the generation of midlatitude jets from Vallis (2006). The figure shows the propagation of Rossby waves and zonal momentum transfer on the left, and the corresponding zonal wind change on the right.

Consider the nondivergent barotropic vorticity equation on a midlatitude beta-plane, linearized about the sheared zonal flow $\bar{u}(y)$.

$$\frac{\partial \zeta'}{\partial t} + \bar{u} \frac{\partial \zeta'}{\partial x} + v' \gamma = 0 \quad (1.1)$$

$$\zeta' = \left(\frac{\partial^2}{\partial x^2} + \frac{\partial^2}{\partial y^2} \right) \psi' \quad (1.2)$$

$$(u', v') = \left(-\frac{\partial \psi'}{\partial y}, \frac{\partial \psi'}{\partial x} \right) \quad (1.3)$$

$$\gamma = \beta - \frac{\partial^2 \bar{u}}{\partial y^2} \quad (1.4)$$

where overbars denote the zonal means, primes denote the deviations from zonal means. ζ' is the vorticity, ψ' is the streamfunction, and γ is the background vorticity gradient.

Assuming that γ is positive everywhere, we define a positive-definite quantity

quadratic in wave amplitude, pseudomomentum P .

$$P = \frac{\overline{\zeta'^2}}{2\gamma} = \frac{\gamma\overline{\eta'^2}}{2}, \quad \zeta' = -\gamma\eta' \quad (1.5)$$

Where η' is the meridional particle displacement. The equation of pseudomomentum conservation can be written as,

$$\frac{\partial P}{\partial t} = -\overline{v'\zeta'} \quad (1.6)$$

Using the nondivergent condition $\partial u/\partial x + \partial v/\partial y \equiv 0$, the zonal mean vorticity flux is equal to the eddy momentum flux convergence.

$$\overline{v'\zeta'} = \frac{1}{2} \frac{\partial(\overline{v'^2 - u'^2})}{\partial x} - \frac{\partial(\overline{v'u'})}{\partial y} = -\frac{\partial(\overline{v'u'})}{\partial y} \quad (1.7)$$

Meanwhile, we have the zonal mean zonal momentum equation, using $\bar{v} \equiv 0$ in the nondivergent flow.

$$\frac{\partial \bar{u}}{\partial t} = -\frac{\partial(\overline{v'u'})}{\partial y} \quad (1.8)$$

Therefore, in the absence of forcing and dissipation, the zonal mean flow is related to the pseudomomentum as follows,

$$\frac{\partial \bar{u}}{\partial t} + \frac{\partial P}{\partial t} = 0 \quad (1.9)$$

Consider the barotropic decay of the midlatitude disturbance (Held, 1985; Held and Phillips, 1987). As the wave enters the initially quiescent regions, given that γ is positive everywhere, the pseudomomentum increases and zonal wind decreases, whereas the zonal wind increases in the regions where the disturbance propagates away. However, to maintain this zonal wind change, the wave propagation should be

irreversible. Wave dissipation occurs near the critical latitude, where the eastward propagation speed of eddies is equal to the zonal mean flow, and the wave amplitude increases considerably such that the background vorticity gradient is homogenized. Nonlinear wave breaking results in a cascade of vorticity variance to smaller scales, where it is eventually dissipated.

As the atmosphere consists of waves of various scales and phase speeds, a prerequisite for this quasi-linear perspective is that the pseudomomentum distribution in various modes is orthogonal. Following Held (1985), we examine the wave solution for Eq. (1.1) of the following form.

$$\psi' = \text{Re}[\tilde{A}\psi(y) \exp(ik(x - ct))] \quad (1.10)$$

and the corresponding eigenvalue equation is,

$$(\bar{u}\nabla_k^2 + \gamma)\psi(y) = c\nabla_k^2\psi(y), \quad \nabla_k^2 = \left(\frac{\partial^2}{\partial y^2} - k^2\right) \quad (1.11)$$

Here $\psi(y) = 0$ at the north and south boundaries ($y = 0, L$). If $\bar{u} = 0$, the modes are simply Rossby waves, $\psi(y) = \sin(l_n y)$, with $l_n = n\pi/L$, and the phase speeds are $c_n = -\beta/(k^2 + l_n^2)$.

Substituting the particle displacement η' in Eq. (1.5) into the eigenvalue equation, we have

$$(\bar{u}\gamma + \gamma\nabla_k^{-2}\gamma)\eta' = c\gamma\eta' \quad (1.12)$$

Suppose the wave field consists of two modes $\eta' = b_1\eta'_1 + b_2\eta'_2$, and the orthogonality of modes is satisfied provided that the global integrals of pseudomomentum of two

modes are additive.

$$\frac{1}{L} \int_0^L \frac{\gamma \overline{\eta'^2}}{2} dy = \frac{|b_1|^2}{L} \int_0^L \frac{\gamma \overline{\eta_1'^2}}{2} dy + \frac{|b_2|^2}{L} \int_0^L \frac{\gamma \overline{\eta_2'^2}}{2} dy \quad (1.13)$$

This can be proved by showing that the cross-term vanishes in the global average. A manipulation of Eq. (1.12) yields.

$$\begin{aligned} \frac{1}{L} \int_0^L \eta_1 (\bar{u} \gamma + \gamma \nabla_k^{-2} \gamma) \eta_2 dy - \frac{1}{L} \int_0^L \eta_2 (\bar{u} \gamma + \gamma \nabla_k^{-2} \gamma) \eta_1 dy \\ = (c_1 - c_2) \frac{1}{L} \int_0^L \eta_1 (\gamma \eta_2) dy, \quad c_1 \neq c_2 \end{aligned} \quad (1.14)$$

The left hand side of the equation is zero, and therefore pseudomomentum can be decomposed into the contributions from individual modes. One should note that the modal orthogonality does not hold for energy and enstrophy, and therefore it is not very useful to think in terms of instantaneous energy or enstrophy distribution in various modes.

Typically, the wave spectrum consists of a set of discrete modes and a continuum of singular modes. While the neutral discrete modes propagate freely at all latitudes, with phase speeds smaller than the zonal wind minimum, the neutral continuum modes have the phase speeds between the zonal wind maximum and minimum, propagating between the critical latitudes or the turning latitude. As the continuum modes are singular at the critical latitudes, they are absorbed in presence of the dissipation, and then transfer zonal momentum from the critical layer into the midlatitude jet. This continuum is the key information in the latitude-phase speed spectrum we will discuss in the following chapters.

1.3 Various viewpoints on the jet movements during climate change

In this section, we summarize various perspectives of views on the jet movements during climate change. A statistical view is that the jet movement can be described by the leading annular mode of internal variability (Thompson et al., 2000; Miller et al., 2006). This is built on the fluctuation-dissipation theorem that the climate response to an infinitesimal forcing resembles the dominant mode of natural variability in the climate system (Leith, 1975). But in this thesis, we focus on the physical mechanisms by which the jets emerge. While the subtropical jet is driven by tropical heating and follows angular momentum conserving winds in the axisymmetric and inviscid limit (Held and Hou, 1980), the eddy-driven jet results from nonlinear mixing of meridional temperature gradients by cyclonic eddies in the polar front regions (e.g. Panetta, 1993). The poleward movement of surface westerlies and storm tracks is implicated in the separation of the eddy-driven jet from the subtropical jet.

S. Lee and collaborators have studied the dynamical relationship of the subtropical jet and polar front jet in a series of papers with an idealized multiple-level primitive equation model. With the linear stability and initial value approaches, Lee and Kim (2003) and Kim and Lee (2004) show that the strength of the subtropical jet can influence the latitude of the most unstable baroclinic waves and the eddy-driven jet, and that when the subtropical jet is relatively weak, the polar front jet is separated from the subtropical jet, due to the emergence of inter-jet disturbance.

Son and Lee (2005, 2006) continue to study the statistically steady solutions as a function of tropical heating and high-latitude cooling. Presumably, the tropical heating controls the strength of the subtropical jet and the high-latitude cooling modifies the meridional width of the extratropical baroclinically unstable zone. In the regime of large tropical heating and small high-latitude cooling, the model atmosphere dis-

plays a single subtropical jet and the dominant internal variability represents the meridional meandering of the jet. In contrast, in the regime of small tropical heating and large high-latitude cooling, the eddy-driven jet is separated and the wind variability is dominated by the poleward propagation of zonal wind anomalies. It is also shown that the climate response has a greater projection on the leading mode of internal variability for the meandering jet regime and the high latitude cooling. Lee et al. (2007) suggest the poleward propagation of zonal wind anomalies can be understood in terms of linear Rossby wave propagation, and nonlinear wave breaking near the critical latitude.

Poleward shift of the storm track and eddy-driven jet may be related to an expansion of the Hadley cell. Assuming that the edge of subtropical descents is the latitude where the vertical wind shear first becomes baroclinically unstable, one can estimate the Hadley cell width by matching the angular momentum conserving zonal wind with the critical wind shear of baroclinic instability in the two layer model (Held, 2000). Despite this very simple assumption, this scaling provides a plausible estimate for the Hadley cell expansion under global warming (Lu et al., 2007). This scaling suggests that the Hadley cell extent depends on the static stability and tropopause height in the subtropics, and that the Hadley cell expansion may be the result of increasing atmospheric static stability due to enhanced water vapor content in the warming climate (Frierson et al., 2006). In an idealized moist GCM, Frierson et al. (2007) also provide a prediction for the poleward shift of storm tracks, when the water vapor content is increased in the model, by tracking the latitude of maximum meridional temperature gradient from the moist static energy balance.

More explicitly, it has been argued that the interaction of the subtropical and eddy-driven jets depends on the wave activity absorption and the resulting zonal wind change near the critical latitude. A number of studies (Chang, 1995, 1998; Robinson, 2002; Seager et al., 2003) suggest that the midlatitude jet variability associated with

the ENSO cycle can be interpreted by the modification of tropical heating/cooling on the subtropical winds, and the subsequent changes in the equatorward wave propagation and refraction. While this argument emphasizes the importance of the critical latitude and refractive index for linear Rossby wave propagation, other nonlinear factors can still play a role in the jet movements with the ENSO variability. For example, Orlanski (2003) suggests that the nonlinear wave breaking can transition from an anticyclonic wave breaking regime to a cyclonic regime for sufficiently strong baroclinic eddies, and result in an equatorward jet shift. Abatzoglou and Magnúsdóttir (2006) find that the planetary wave breaking in the North Hemisphere is increased considerably during La Niña years, which can also influence the structure of the subtropical jet.

Furthermore, the variability of the stratospheric flow can have a substantial impact on the tropospheric jet. It is observed that large anomalies of stratospheric zonal winds can propagate downwards into the troposphere and affect the tropospheric weather systems (Baldwin and Dunkerton, 1999, 2001; Thompson et al., 2005), and the downward propagation can increase the persistence and predictability of the tropospheric flow (Baldwin et al., 2003). Rind et al. (2005a,b) show that the positive annular mode trends can be generated in a comprehensive climate model in response to stratospheric cooling and tropospheric warming or changes in the low- and high-latitude sea surface temperatures. These forcings can affect the propagation and refraction of tropospheric waves, but the relative importance of these forcings and the underlying mechanisms remain inconclusive. Recently, Lorenz and DeWeaver (2007) find that the IPCC AR4 models predict a consistent poleward jet shift, accompanied by a strengthening and a poleward and upward shift of transient eddy kinetic energy and momentum flux. They can simulate qualitatively similar changes in a simple GCM by directly raising the tropopause height, and argue that the poleward jet shift under global warming is driven by a rise in the tropopause height due to tropospheric

warming and stratospheric cooling. But the physical mechanism is still not clear by which the tropopause height is related to the latitude of tropospheric jet.

In this thesis, we find that the tropospheric eddies display a trend towards faster eastward phase speeds in the observations and model simulations for the late 20th century, and in the model projections for the 21st century. According to idealized model studies with more generic forcings, we argue that the increased lower stratospheric or upper tropospheric zonal winds, associated with stratospheric ozone depletion or global warming, can be sufficient to increase eddy phase speeds so as to shift the circulation polewards.

1.4 Outline

In chapter 2, we study the sensitivity of the latitude of surface westerlies with respect to surface friction. We argue that the poleward jet shift seen in a model, when the strength of surface friction is reduced, is due to the increased eastward propagation of tropospheric eddies associated with the accelerated midlatitude jet. This mechanism is supported by a stochastically stirred shallow water model that simulates the dynamics of the upper troposphere. The content of this chapter appears in Chen et al. (2007). In chapter 3, we examine the tropospheric jet response to a prescribed zonal torque in the troposphere or in the stratosphere. The tropospheric jet shifts poleward for a westerly torque in the extratropical stratosphere, and for a westerly torque on the poleward flank of the jet in the troposphere. We suggest that the downward influence of the stratosphere is through modifying the eastward propagation of tropospheric eddies. In chapter 4, we have further explored the interannual variability and long-term trend in the latitude of surface westerlies in the observations and climate models. The results are consistent with the tropospheric phase speed mechanism gained from idealized model studies. Part of chapter 4 appears in Chen and Held

(2007). Finally, we provide a brief summary for this dissertation in chapter 5.

Chapter 2

The Importance of Barotropic Shears in the Troposphere

2.1 Introduction

In this chapter, we examine the key processes that control the latitude of surface westerlies. Particularly, we examine a simple way of shifting the westerlies in an idealized model of the troposphere: changing the strength of surface friction. As the strength of surface drag is reduced, the surface westerlies and the midlatitude jet move polewards (Robinson (1997), hereafter R97). We use this problem as a test case for our understanding of the controls on the midlatitude eddies and the associated mean flows, as it remains a challenge to identify and isolate cleanly the dynamical mechanisms underlying this shift. Our hope is that the understanding gained will help in the analysis of some of the factors of more direct relevance for climate sensitivity mentioned in the introduction.

The sensitivity to surface friction is itself potentially relevant to an understanding of model biases. There is considerable dynamical similarity between the response to changes in surface friction and the response to changes in orographic gravity wave

drag (Robinson, 1997), which is introduced into GCMs to take into account the effects of subgrid scale orography on the atmosphere. As orographic gravity wave drag is introduced, it prevents the excessive strength of the low level westerlies, but these westerlies are simultaneously displaced equatorward (e.g. Stephenson, 1994). The westerlies are often biased equatorward in comprehensive GCMs (Russell et al., 2006), so this added displacement is generally undesirable. A better understanding of the effects of various types of momentum exchange with the surface on the latitude of the westerlies should be of value for model development.

The surface westerlies can be thought of as marking the location of the dominant region of baroclinic eddy generation: to the extent that wave activity radiates away from this source, eddy momentum fluxes converge into this region, and this momentum is removed from the atmosphere by surface friction through the generation of surface westerlies, as is discussed in chapter 1. Using a global two level primitive equation model, R97 argues that a reduction in surface drag results, first of all, in an enhancement of the barotropic component of the flow, with relatively modest changes in the baroclinic component. But these changes in barotropic meridional shears then modify the eddy heat and momentum fluxes in such a way as to move them polewards, along with the surface westerlies balanced by the momentum flux convergence.

One starting point for thinking about this issue is the analysis of linear baroclinic normal modes and nonlinear baroclinic eddy life cycles. As the barotropic shear increases, linear baroclinic instability is suppressed and eddy fluxes tend to be more confined meridionally, effects referred to as the "barotropic governor" (James, 1987). R97 suggests that this mechanism is more active on the equatorward side of the midlatitude storm track, resulting in stronger suppression on the equatorward side and poleward displacement of the eddies.

Barotropic meridional shear can have a strong effect on baroclinic eddy life cycles and the resulting mean flow modification. Simmons and Hoskins (1980) and Thorn-

croft et al. (1993) vary the barotropic shear on the equatorward flank of the jet in the initial condition, and obtain two distinct types of life cycle (LC). In LC1, the wave breaking is primarily on the anticyclonic side of the jet, and the final jet position moves to the poleward flank of the initial jet. In LC2, with enhanced cyclonic shear in the initial condition, waves break on the cyclonic side of the jet, and the jet is displaced slightly equatorward. The relationship between the type of life cycles and the jet latitude is also found in the longtime integrations of an idealized dry GCM by Akahori and Yoden (1997). Therefore, changes in the factors that control eddy life cycles which favor LC1 over LC2, such as the increased anticyclonic shear equatorward of the jet, should shift the jet polewards. Hartmann and Zuercher (1998) gradually increase the barotropic shear and find that the transition from LC1 to LC2 is abrupt at a critical value of the strength of the added shear. Thorncroft et al. (1993) and Hartmann and Zuercher (1998) suggest that the type of the wave breaking and the direction of the jet shift can be understood in terms of Rossby wave refraction and reflection. Orlanski (2003), in contrast, finds that a transition from LC1 to LC2 can be obtained in a shallow water model by increasing the amplitude of the forcing, and shows high resolution life cycles in dry and moist 3D atmospheres that highlight this amplitude effect.

The mid-latitude storm tracks are composed of many growing and decaying waves, often having a non-modal character. Rather than thinking in term of linear modes or nonlinear life cycles initialized with normal modes, one can try to think in terms of stochastically generated variability (see the review by Delsole (2004)). As shown by Delsole (2001), the climatological eddy momentum fluxes can be rather well simulated in the simplest linear stochastically driven barotropic model. It is natural to ask if a model of this type can be constructed to help explain the sensitivity of the westerlies to surface friction.

We have examined the sensitivity of the circulation to surface friction in the ide-

alized dry GCM presented in Held and Suarez (1994), hereafter HS, confirming the robustness of the conclusions in R97. We then attempt to capture the essence of this shift in a stochastically stirred nonlinear shallow water model. The changes in the space-time spectra in the idealized GCM suggest to us that an increase in the characteristic eastward phase speed of the eddies is a key component of the response. This increase in phase speed can be attributed to the increase in the barotropic component of the flow following the decrease in surface drag. We examine the consequence of this increase in phase speed by manipulating the stirring in the shallow water model. The result is indeed a poleward shift in the convergence of the eddy momentum flux that we can think of, at least qualitatively, as due to a shift in the subtropical critical latitude.

The chapter is organized as follows. In section 2.2, we describe the climatological jet shift as a function of surface friction in the HS model, particularly comparing the relative importance of the drag on zonal mean winds and the drag on the eddies. In section 2.3, we examine the transient response to an instantaneous change in the surface drag and the resulting changes in eddy-mean flow interaction, distinguishing between relatively fast and slow components of the response. In section 2.4, we examine the eddy flux spectra as a function of latitude and angular phase speed, and speculate on the importance of the shift in the subtropical critical latitude. In section 2.5, we describe the shallow water model of the upper troposphere. We offer brief discussions and conclusions in section 2.6. Finally, we review the energy cycle of the atmosphere in Appendix A, the details of the shallow water model configuration in Appendix B, and the space-time spectral analysis in Appendix C. The contents of this chapter appear in Chen et al. (2007).

2.2 Mean drag versus eddy drag

We use a spectral dry dynamical core, forced by zonally symmetric Newtonian relaxation to the prescribed equilibrium temperature field and damped by Rayleigh friction near the surface, as in HS. The model is run at T42 and T85 horizontal resolutions with 20 equally spaced sigma levels in the vertical. The model output is sampled daily, and the time averaged results are averaged over the last 1600 days of 2000 day integrations.

In the HS formulation, the boundary layer in the momentum equation is simply represented by linear Rayleigh damping in the lower troposphere. The vertical structure of the damping rate is prescribed, decreasing linearly from its value at the surface to zero at $\sigma = 0.7$. This vertical structure is unchanged in all of our simulations. References in the following to the damping time scale refer to the value at the surface. The hyperdiffusion (∇^8) is set so that the diffusive damping time of the smallest retained spherical harmonic is 0.1 days.

Whereas linear friction damps the zonal mean flow and the zonally asymmetric eddies equally in HS, R97 shows that the jet shift is mainly controlled by the friction on the zonal mean in the two-layer model examined. Hence, we separate the boundary layer drag into the drag on the zonal mean flow (mean drag) and the drag on the eddies (eddy drag).

$$D = -\frac{\bar{u}}{\tau_{fz}} - \frac{u'}{\tau_{fe}} \quad (2.1)$$

$$= -\frac{u}{\tau_f}, \quad (\text{only if } \tau_{fe} = \tau_{fz}) \quad (2.2)$$

Overbars and primes denote the zonal means and the deviations from zonal means; τ_{fz} is the mean damping time and τ_{fe} is the eddy damping time. We use the symbol τ_f when the damping times τ_{fz} and τ_{fe} are equal. As in HS, the control value for the frictional damping time at the surface is 1.0 day.

We first examine the resolution dependence of the model sensitivity to the surface drag. Figure 2.1 shows the surface (lowest model level) winds at T42 and T85 resolutions for experiments in which τ_f is increased to 1.5 and decreased to 0.5. We also show simulations in which τ_{fe} is varied over this same range, holding τ_{fz} fixed at the control value, and in which τ_{fz} is varied holding τ_{fe} fixed. The strength of the subgrid scale diffusion is modified when the resolution is changed so as to maintain the same diffusive damping time for the smallest resolved spherical harmonic.

We conclude that T42 is sufficient for our study. In both T42 and T85, as the eddy/mean/total damping time increases (surface friction decreases), the extratropical westerlies and tropical easterlies are intensified, and the extratropical westerlies are displaced poleward. The only significant departure is for the case of increased eddy damping, where there is a larger equatorward shift in the higher resolution model. Also evident from this figure is that the effects of the change in drag are captured relatively well by changing the mean drag only, as in R97.

Using the T42 model, the changes of the atmospheric circulation are displayed in Figs 2.2 and 2.3 as a function of mean drag, eddy drag and total drag, varying the damping time over the range 0.25 to 1.75 in increments of 0.25. We show the upper tropospheric zonal mean winds ($\sigma=0.275$) and the lower tropospheric zonal mean winds ($\sigma = 0.875$) in Fig. 2.2, and the globally averaged eddy and zonal mean kinetic energies in Fig. 2.3. As the mean drag is reduced, the poleward movement of the surface westerlies is continuous over the entire range of damping rates displayed. The upper level eddy driven jet moves polewards continuously as well. For small mean drag, the eddy driven jet in the upper troposphere separates distinctly from the subtropical jet, which is weak in this model due, in part, to the weakness of the tropical heating. Zonal mean kinetic energy K_M is naturally strengthened as the mean drag is reduced, but the eddy kinetic energy K_E is weakened, as expected from the barotropic governor mechanism. Inspection of the model energy cycle (not shown)

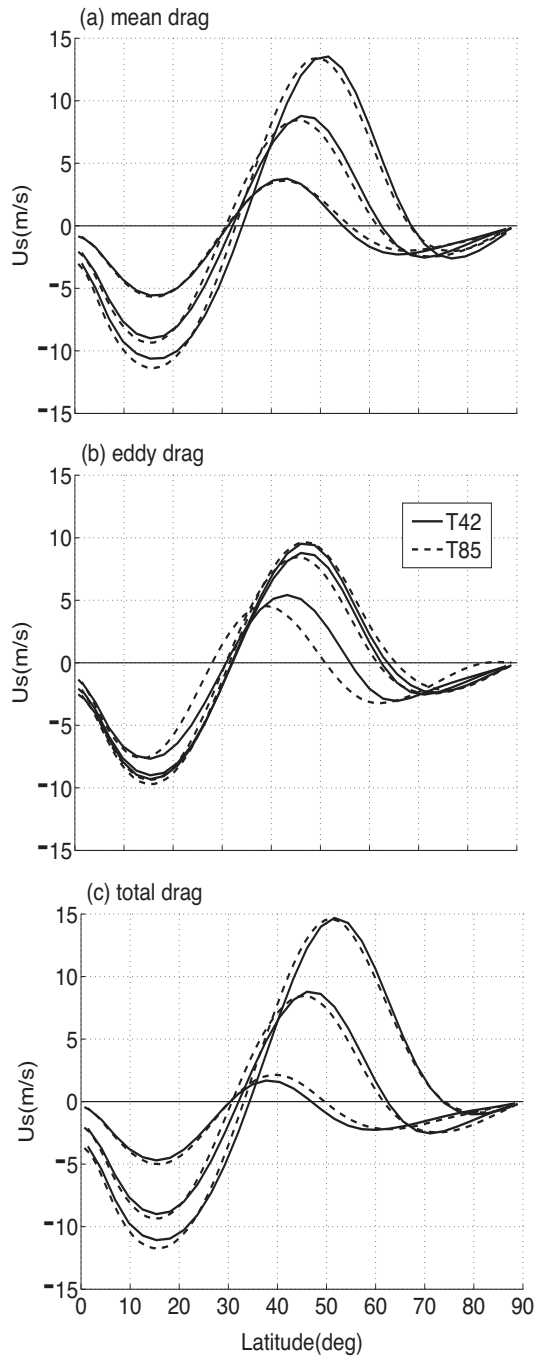


Figure 2.1: The time and zonally averaged surface winds ($\sigma = 0.975$) as a function of (a) mean drag, (b) eddy drag, (c) total drag at T42 and T85 resolutions. The mean/eddy/total frictional damping times are 0.5, 1.0 and 1.5 day. As the damping time increases (surface friction decreases), both the extratropical westerlies and tropical easterlies are intensified, and the extratropical westerlies are displaced poleward.

indicates that the conversion of potential to kinetic energy changes only slightly, while the barotropic conversion increases, despite the reduction in eddy kinetic energy, due to the increased meridional shears.

The dependence on eddy damping is more complex. There is an equatorward movement as the drag is increased from its control value, but this movement is fairly abrupt as a function of the damping rate; as the drag is decreased from the control value, there is relatively little movement. The abruptness is related to the separation of the storm track from the subtropical jet as the damping is reduced. Before this separation, the flow attempts to squeeze an eddy source and the associated surface westerlies into high latitudes, but this is ill-defined. This abrupt character here might be responsible for the difference in the T42 and T85 resolutions as the eddy damping is increased in Fig 2.1b. Also it may be related to that found in the jet mergers discussed in the QG context (Panetta, 1993; Lee, 1997), and by Lee (2005) for a spherical primitive equation model.

If the changes in damping parameters are small, we should be able to predict the changes in climate as the total drag is modified from the corresponding runs in which the mean drag and eddy drag are modified separately. For example, for the globally averaged eddy or zonal mean kinetic energy,

$$\frac{\partial E(\tau_f)}{\partial \tau_f} \delta \tau_f \approx \frac{\partial E(\tau_{fz}, \tau_{fe} = \tau_0)}{\partial \tau_{fz}} \delta \tau_{fz} + \frac{\partial E(\tau_{fz} = \tau_0, \tau_{fe})}{\partial \tau_{fe}} \delta \tau_{fe} \quad (2.3)$$

where τ_0 is the control value of surface drag, and the higher order terms are neglected. As seen in Fig. 2.3, this linear decomposition matches the total drag runs rather well. A key observation is that the effects of the mean drag and eddy drag on K_E are opposite and largely cancel when the two parameters are varied simultaneously. Therefore, when one varies the total drag, one is seeing the combined effects of two rather different dynamical mechanisms. Despite its seeming artificiality, we follow

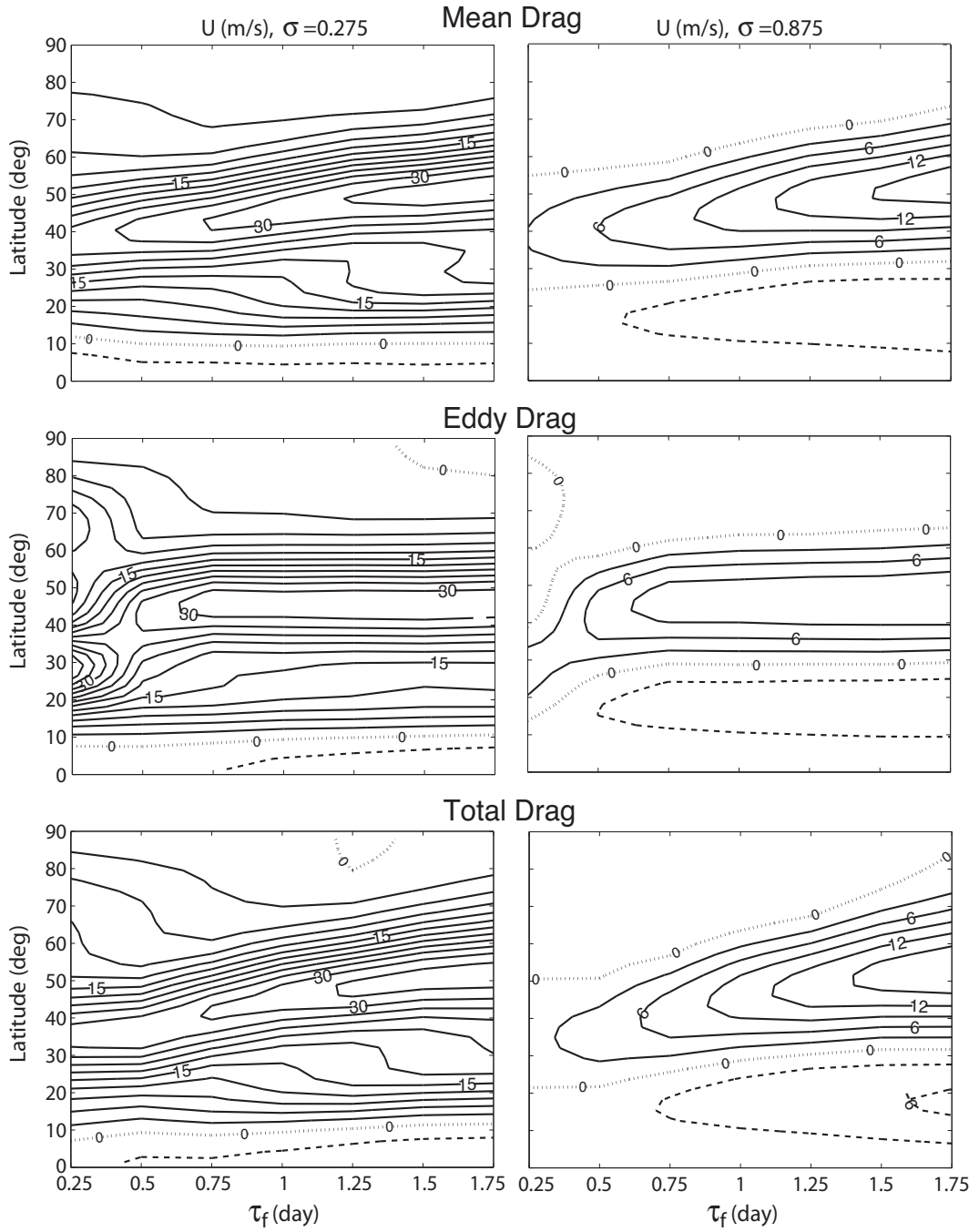


Figure 2.2: The time and zonally averaged zonal winds at (left) $\sigma=0.275$ and (right) $\sigma=0.875$ as a function of (top) mean drag, (middle) eddy drag and (bottom) total drag. The contour interval is 3 m/s.

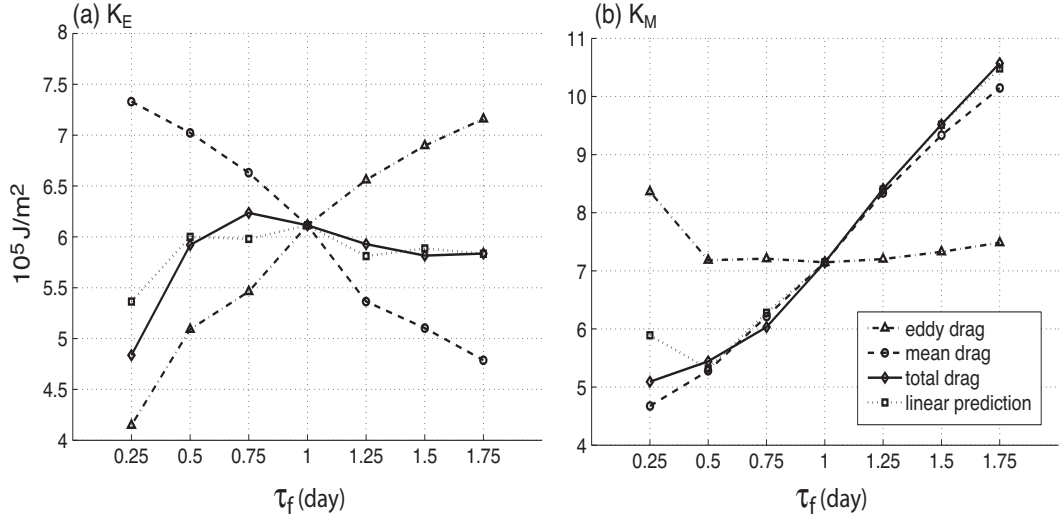


Figure 2.3: The time and globally averaged (a) eddy kinetic energy and (b) zonal mean kinetic energy as a function of eddy drag, mean drag, total drag, and the linear decomposition. The linear prediction is described in the text.

R97 in finding it important to separate these two mechanisms. The effects of varying mean damping are responsible for a large fraction of the total response, and do not involve the rather abrupt behavior of the model when eddy damping is increased. Therefore, we choose to focus on the effects of mean damping.

If one linearizes Eq. (2.1) about the control values of the time and zonally averaged zonal winds $\langle \bar{u}_0 \rangle$ and surface drag τ_0 , and assumes that the deviations are small, one obtains.

$$-\delta\left(\frac{\bar{u}}{\tau_{fz}}\right) \approx -\langle \bar{u}_0 \rangle \delta\left(\frac{1}{\tau_{fz}}\right) - \frac{\delta\bar{u}}{\tau_0} \quad (2.4)$$

The first term is equivalent to the addition of a constant zonal mean torque proportional to the control surface winds and applied within the boundary layer. To test whether this term dominates the results, rather than changing the surface friction, we add a torque to the model of the strength and structure corresponding to this first term, using the frictional damping difference between the 1.0 and 1.5 day. The surface wind response to this torque is compared in Fig. 2.4 with the surface wind

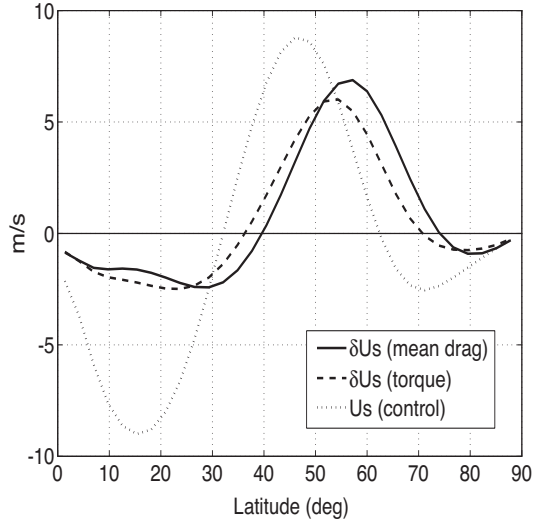


Figure 2.4: The time and zonally averaged surface wind ($\sigma=0.975$) response to the constant torque described in the text using the damping time change from 1.0 to 1.5 day, compared with the surface wind change as the mean drag is reduced from 1.0 to 1.5 day. The torque is proportional to the time and zonal mean surface wind in the control run (dotted).

change as the mean drag is reduced from 1.0 to 1.5 day. While the response of surface winds is slightly less poleward and weaker in the case of the imposed torque, the two cases agree rather well. This result implies that the surface wind displacement can be thought of, qualitatively at least, as a response to an imposed zonal mean torque.

2.3 The transient response to a change in the mean drag

Although we perturb the surface friction on the eddies and zonal mean flow separately, the equilibrated response does not answer the question of cause and effect in the eddy-mean flow interaction. As a start in addressing causality, it is useful to examine the adjustment of the eddies and zonal means in the time-dependent response to a sudden reduction in the mean drag. Starting from the equilibrated state with the 0.5 day mean drag, we increase the mean damping time to 1.5 day and run the model until

it equilibrates. The same experiment is repeated with 30 different initial conditions selected from the run with 0.5 day damping. The evolution of the ensemble mean is displayed in Fig. 2.5.

The figure illustrates vividly two distinctive adjustment time scales. In days 0-15, the fast adjustment, the mean kinetic energy, K_M , increases in response to the weaker mean drag while the eddy kinetic energy, K_E , decreases. Thus, the barotropic governor effects act quickly, but with little effect on the jet position. The poleward jet shift occurs mostly in the slow adjustment, days 15-300, accompanied by further increase in the zonal mean kinetic energy with an e-folding time of roughly 50 days.

Figure 2.6 shows the vertical structure of zonal wind changes during the fast and slow adjustments. In days 0-15, the extratropical winds at all levels in the troposphere follow the increase of the surface westerlies. If the eddy fluxes were held fixed, the response of zonal winds would be purely barotropic (Robinson, 2000). However the vertical shear in the zonal winds also increases somewhat, a response that we attribute to the reduction in the eddy kinetic energy and poleward heat flux due to the barotropic governor. The poleward shift during the slow adjustment also displays an equivalent barotropic structure outside of the tropics, as expected from the response to a latitudinal displacement of the eddy-driven component of the wind field forced by a shift of the upper level eddy momentum flux convergence (Robinson, 2000). The equilibrated response is the consequence of the initial rapid barotropic acceleration at the jet latitude and the following slow poleward jet shift.

Consistent with the surface winds, the poleward movement of the eddy momentum flux convergence (Fig. 2.5d) occurs primarily during the slow response. The increase in barotropic component of the flow and the reduction in eddy kinetic energy occur before there is a substantial poleward displacement. There is also some reduction in the magnitude of the momentum flux initially, after which there is slow recovery.

Because the eddy energy reduction is so rapid and large, if the barotropic governor

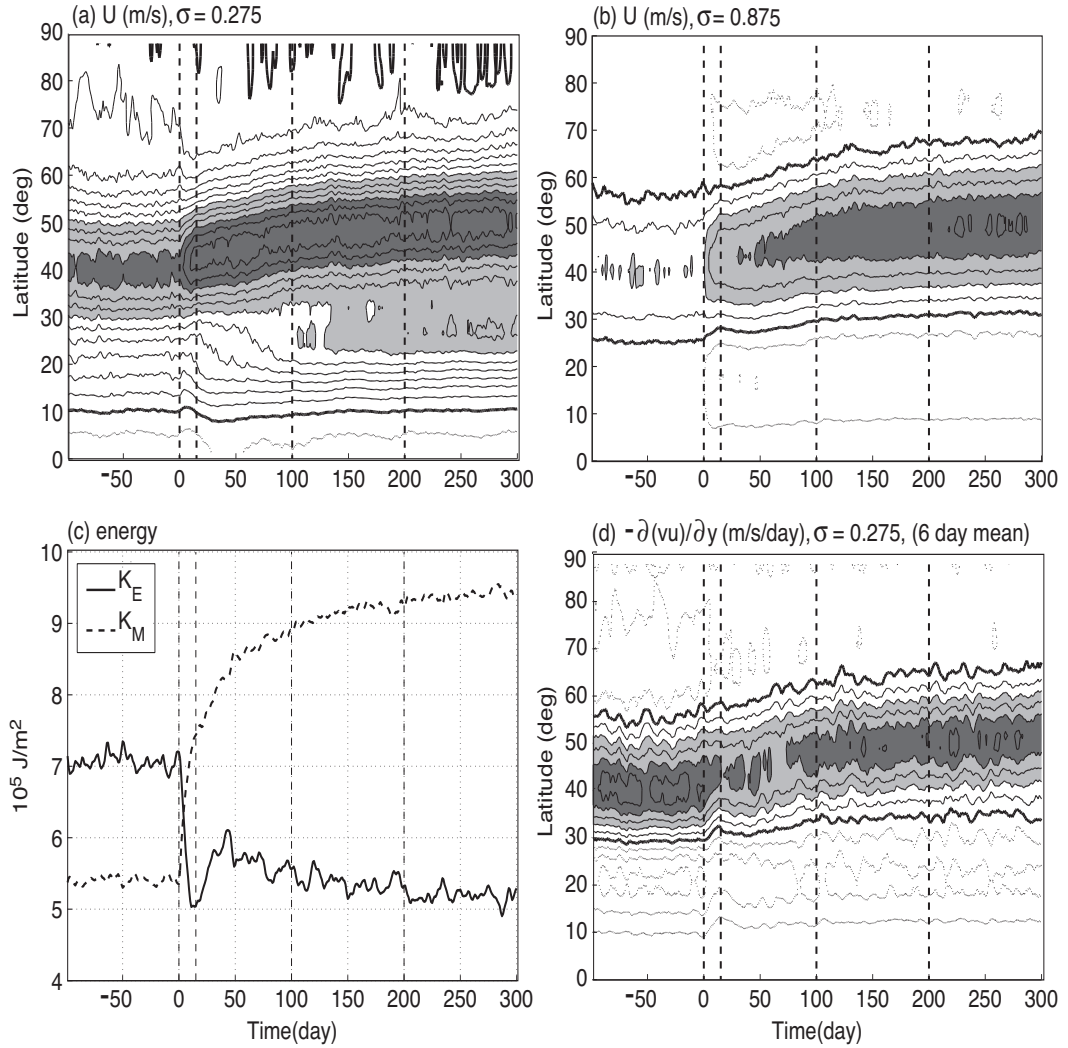


Figure 2.5: The ensemble means of the transient response: zonal mean zonal winds at (a) $\sigma=0.275$ and (b) $\sigma=0.875$, (c) global mean energies, and (d) zonal mean eddy momentum flux convergence at $\sigma=0.275$. The mean damping time increases from 0.5 to 1.5 day on day 0. The second vertical dashed line indicates day 15. In (a), (b) and (d), the solid (dotted) contours denote positive (negative) values, and thick solid contours denote zeros. The contour interval is 3 m/s for (a) and (b), 1 m/s/day for (d). The figures are plotted using daily data, except for (d) which is smoothed by a 6 day running mean.

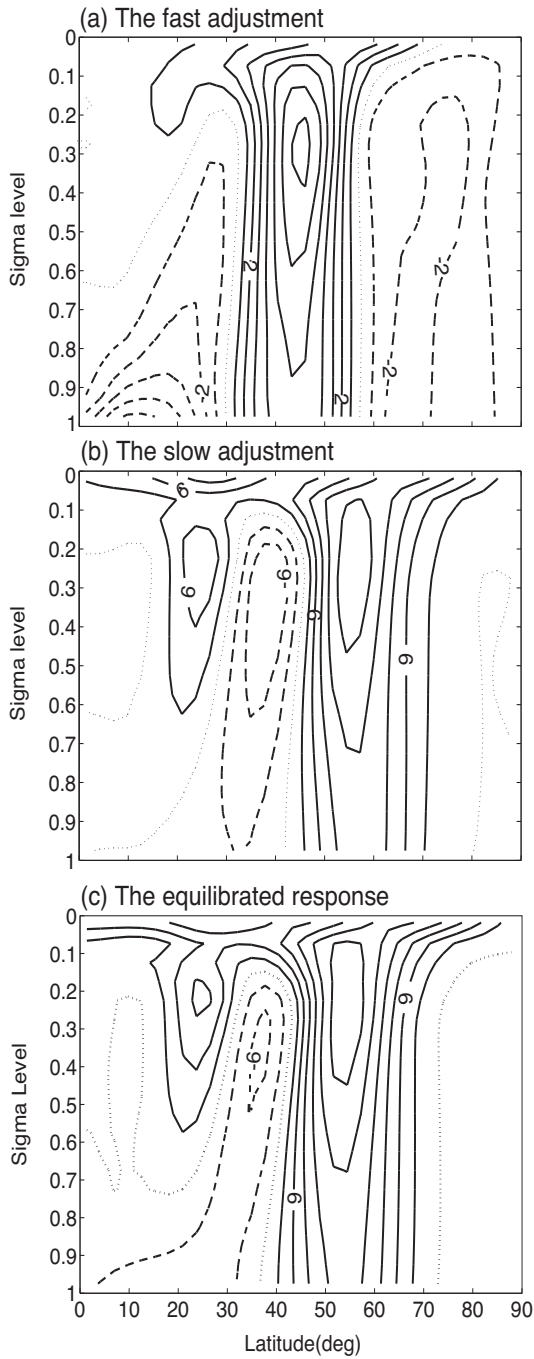


Figure 2.6: The vertical structure of zonal wind changes during (a) the fast adjustment (days 0-15) and (b) the slow adjustment (days 15-300) in the transient response as in Fig. 2.5, in comparison with (c) the equilibrated response (1.5 day drag minus 0.5 day drag). The contour intervals are 1 m/s for (a), 3 m/s for (b) and (c).

were central to the forcing of the poleward shift, we might expect a more rapid response of the zonal mean jet. This suggests that the barotropic governor mechanism, responsible for the eddy energy reduction, may not be directly linked to the poleward displacement.

Given the two-phase character of the adjustment, with slow poleward displacement, we believe that the idealization described in R97, with an initial phase in which the mean flow adjusts in place to the drag, with no change in eddy activity, is still useful, even though there are, in fact, significant changes in eddy amplitude in this phase.

2.4 The eddy flux cospectra and the critical latitude shift

In order to characterize more fully the wave activity redistribution in the upper troposphere, we plot spectra of the upper tropospheric ($\sigma = 0.275$) momentum flux convergence as a function of latitude and angular phase speed (Randel and Held, 1991; Lee, 1997; Kim and Lee, 2004) in Fig. 2.7. We utilize angular phase speed rather than phase speed (c), because the former is conserved as a Rossby wave packet propagates meridionally in a zonally symmetric background flow. (In the figure we actually use $c_A = c/\cos\phi$, the angular phase speed multiplied by the radius of the Earth a .) To estimate the spectrum, we divide the model output into 10 periods of length $T = 160$ days. The resolution in phase speed space, Δc_A , is limited by the time period T and the zonal wavenumber m , $\Delta c_A = a(2\pi/T)/m$. Because of its large Δc_A , we ignore the very small contribution to the flux from $m = 1$ in this plot.

The spectra are primarily confined between two critical latitudes (where $\bar{u}/\cos\phi = c_A$) defined by the time mean flow at this upper tropospheric level, with the faster waves restricted to the regions near, and somewhat equatorward of, the jet maximum.

Since Rossby waves prefer to propagate equatorward on the sphere, and tend to break before they reach their linear critical latitudes, most of the wave activity diverging from midlatitudes converges close to, but somewhat poleward of, the subtropical critical latitude.

As the mean drag is reduced from 0.5 day to 1.5 day, the range of eddy angular phase speeds at the latitudes of 20-40° extends from -7~20 m/s to -5~30 m/s. The difference between these two spectra emphasizes the increase in equatorward propagation in waves with angular phase speeds of 10~30 m/s and the decrease with phase speeds of -7~10 m/s. The poleward movement of the divergence is especially associated with the faster phase speeds.

This increase of angular phase speed is a plausible consequence of the barotropic increase of extratropical westerly winds (Fig. 2.6a) that occurs during the fast adjustment. The subtropical zonal winds barely change, partly because they overlie weak surface winds near the transition from easterlies to westerlies, where the effect of the reduction in the mean drag is not strongly felt. The net effect of the increase in phase speed of the dominant eddies and the lack of increase in the subtropical upper level winds, is a poleward shift of the subtropical critical latitude.

More explicitly, assume that the fast response is purely barotropic in the latitudes between the surface westerly wind maximum and the critical latitude for the dominant waves. It is then reasonable to expect the phase speed of the dominant eddies to be modified by an amount equal to the surface wind change at the center of the storm track, located near the center of the surface westerlies (ϕ_w): $\delta c \approx \delta u_s(\phi_w)$. The change in the upper level winds near the critical latitude ϕ_c for these dominant waves, assuming a barotropic response, is $\delta u_s(\phi_c)$. The critical latitude moves poleward provided that $\delta u_s(\phi_w) > \delta u_s(\phi_c)$, or, assuming that these changes in the surface winds are approximately the unperturbed winds times the change in frictional time scale, $u_s(\phi_w) > u_s(\phi_c)$.

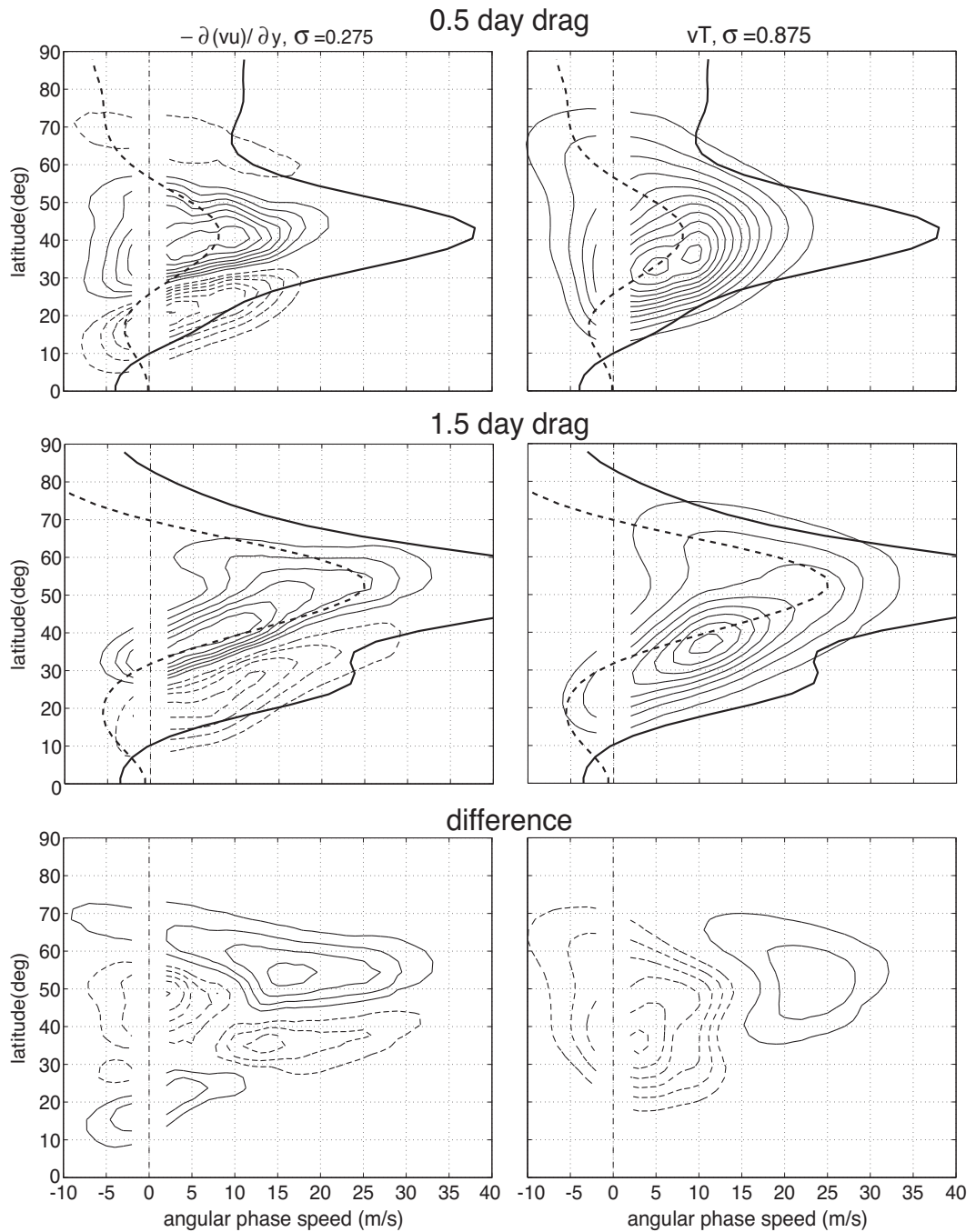


Figure 2.7: The (left) eddy momentum flux convergence spectra at $\sigma=0.275$ and (right) eddy heat flux spectra at $\sigma=0.875$ for (top) the 0.5 day drag, (middle) 1.5 day drag, (bottom) the difference (1.5 day drag minus 0.5 day drag) as a function of angular phase speed and latitude. The thick lines are the time and zonally averaged angular velocities at $\sigma=0.275$ (solid) and at $\sigma=0.875$ (dashed). The contour interval is 0.015 m/s/day for eddy momentum flux convergence, 0.05 Km/s for eddy heat flux, and zero lines are omitted.

To support the speculation described above, we plot the eddy spectral changes in the fast adjustment in Fig. 2.8. The space-time spectra are calculated by performing Fourier transforms over days 1-30, averaging among 30 ensemble members, and subtracting the spectra for the control simulation. Due to limitations of the spectral resolution, we show the results only for $m \geq 5$, but these are the dominant waves in the eddy momentum flux. It is seen that there is indeed a phase speed increase in the fast adjustment, and a slight poleward shift in the eddy momentum flux convergence. However, the magnitude of the increase in phase speed is less than half of that in the equilibrated state (note the smaller contour interval in Fig. 2.8). The implication is that some of the increase in phase speed accompanies the poleward displacement.

The eddy heat flux in the lower troposphere ($\sigma = 0.875$) displays a similar increase in dominant phase speeds and a poleward shift in the equilibrated response (Fig. 2.7) and a smaller increase in phase speeds in the fast transient response (Fig. 2.8). Our hypothesis is that this lower level eddy flux displacement is driven by the latitudinal displacement of the upper level disturbance. The underlying mechanism connecting the upper to the lower troposphere can be thought of in several ways. One can argue that baroclinic instability, as traditionally measured by the Eady growth rate in the lower troposphere, is directly modified by zonal winds and associated vertical shears generated by upper level eddy momentum fluxes. Alternatively, one can think of the near surface temperatures as being stirred by upper tropospheric potential vorticity anomalies, and use a diffusive eddy closure argument for the lower level eddy heat fluxes by defining the diffusivity to be proportional to the upper level stream function variance (Held, 1999).

While it seems plausible that the shift in phase speeds and the subtropical critical latitude is related to the displacement of the eddy fluxes, it is not straightforward to make a quantitative connection between the two, given the potentially complicated wave breaking processes in the upper troposphere and their feedback onto the lower

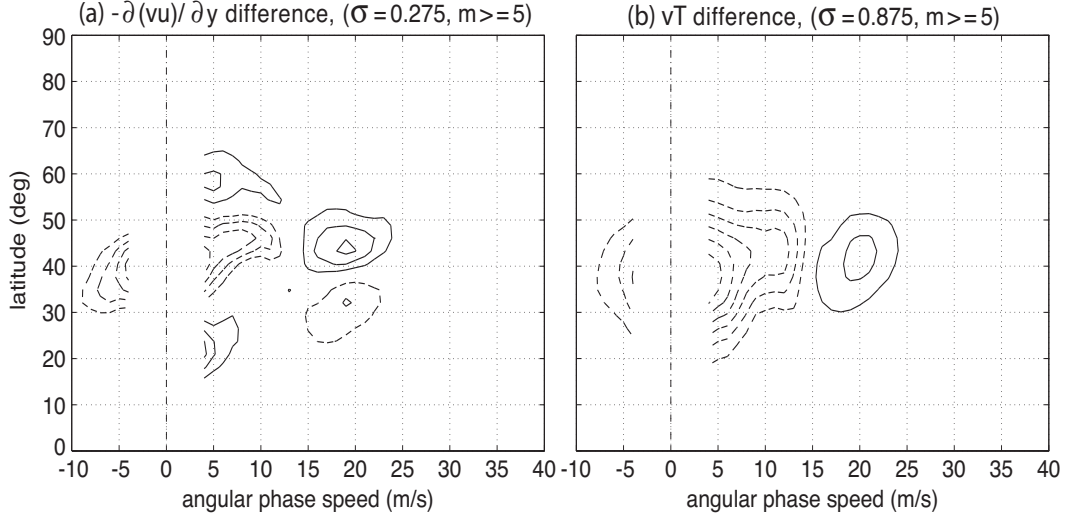


Figure 2.8: As for Fig. 2.7, but for the difference of the ensemble mean (a) eddy momentum flux convergence spectra at $\sigma=0.275$ and (b) eddy heat flux spectra at $\sigma = 0.875$ in the transient response (days 1~30 minus the control, where the spectra are calculated by performing Fourier transforms over 30-day periods, and averaging among 30 ensemble members). The spectra only consist of zonal wavenumbers $m \geq 5$. The contour interval is 0.0075 m/s/day for eddy momentum flux convergence, 0.025 Km/s for eddy heat flux.

tropospheric disturbances. Hartmann and Zuercher (1998) provide some interesting insights on this connection from the nonlinear life cycle point of view. For the case of stronger anticyclonic shear on the equatorward side of the initial jet (corresponding to smaller shear parameter in their paper), the eddy phase speed is faster, implying a more poleward critical latitude. However, the transition from LC2 to LC1, in favor of a poleward jet shift, occurs only at a threshold value, therefore it is unclear in these calculations if the phase speed change and the jet shift are closely connected.

We have also performed life cycle calculations with the control climatological mean winds, varying the barotropic component of the flow within the range of the changes in the mean drag experiments. All the calculations are initialized with the same finite amplitude normal mode perturbation of zonal wavenumber 5, which is the energy containing eddy scale in the control experiment. Figure 2.9 shows the zonally averaged zonal winds in the upper troposphere ($\sigma = 0.275$) at day 1 and day 20,

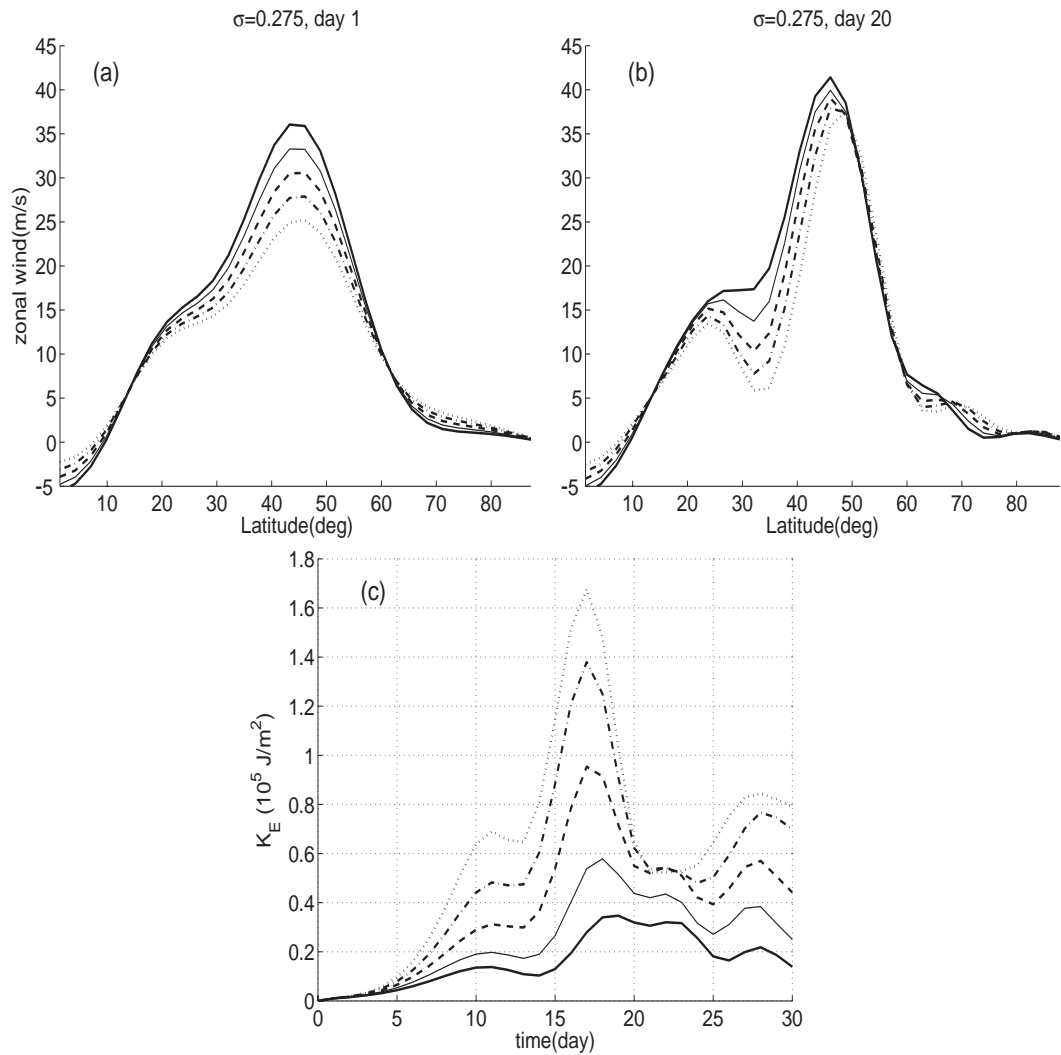


Figure 2.9: Baroclinic eddy life cycle calculations with the control climatological mean zonal winds, and the barotropic component of the flow is varied within the range of the changes in the mean drag experiments. The figure shows the zonal mean zonal winds at $\sigma=0.275$ on (a) day 1 and (b) day 20 in the life cycle, and (c) the global mean eddy kinetic energy as a function of time. The five lines represent the experiments with different initial barotropic shears.

and the global mean eddy kinetic energy as a function of time. The midlatitude jet displaces poleward from the initial jet latitude in all experiments, showing no sign of bifurcation but only the characters of LC1, and the zonal wind response is marked by the deceleration in the subtropics, implicative of the absorption of wave activities near their critical lines. The evolution of eddy kinetic energy shows a strong barotropic governor effect, that the maximum energy is observed in the case of the smallest barotropic meridional shear in the initial jet. We can easily calculate the eddy phase speeds in the linear stage of life cycle, and the larger initial barotropic shear (larger anticyclonic shear in the subtropics) is found to result in a faster eastward phase speed and the more poleward critical latitude, as we see in the mean drag experiments. However, the poleward shift is smaller in the case of larger barotropic flow, and the zonal wind deceleration in subtropics appears to be controlled by the strength instead of the latitude of the nonlinear wave breaking. Similar results are found in the experiments initialized with the most unstable mode in the climatological zonal winds ($m = 8$). One can attribute this apparent contradiction to full model experiments to the shortcomings of a single eddy life cycle, as it is also pointed out by Akahori and Yoden (1997) that there are some differences in the life cycles between the initial value approach and the longtime integrations. Given the inconclusive character of these life cycle results, we turn instead to a stirred shallow water model of the upper troposphere.

2.5 A shallow water model of upper troposphere

Motivated by the theory of jet creation described in the introduction, a simple model is constructed to study the wave activity redistribution and the associated jet shift in the upper troposphere. The notion is to idealize the upper troposphere as one shallow water layer forced by random stirring in the divergence field. Stirring in the divergence

equation is equivalent to specifying a stochastic component in the pressure gradient below the active layer. Models built on similar ideas have been used to study the eddy momentum fluxes and wave-mean flow interaction (Held and Phillips, 1990; Delsole, 2001; Orlanski, 2003; Vallis et al., 2004). Our model configuration is described in detail in Appendix B, and has the following characteristics:

- The model is nonlinear so as to directly simulate wave breaking.
- The upper layer is stirred by specifying a stochastic source to the divergence equation, so that the stirring does not modify the potential vorticity. We believe that this is more physical than directly stirring in the potential vorticity or vorticity field, in that this does not introduce an explicit source in the pseudomomentum conservation equation.
- The stirring has a space-time spectrum centered on a characteristic angular phase speed, and is localized in midlatitudes, with no feedback onto the stirring from the upper layer dynamics. In the calculations described, the stirring amplitude is modest in the sense that there is relatively little inverse cascade of energy.
- There is a lower layer with no eddies but with a zonal mean wind that is assumed to be equal to the eddy momentum flux convergence in the upper layer divided by a surface damping rate; these winds feed back onto the upper tropospheric winds via thermal wind balance. This allows us to separately modify the barotropic shears, by varying the surface damping, and the characteristic phase speed of the stirring.
- The interface between the two layers or, equivalently, the upper layer thickness, is relaxed to a specified radiative equilibrium value.
- The rigid top of the upper layer is given some latitudinal structure, increasing

the thickness of the upper layer in the tropics, to assist in generating a plausible control simulation.

Some features of the control simulation with this shallow water model are displayed in Fig. 2.10. This model generates poleward eddy thickness fluxes as well as eddy momentum fluxes that converge in midlatitudes. The equator-to-pole thickness gradient is reduced by the poleward eddy thickness flux and is restored by the relaxation towards radiative equilibrium. (In the absence of the stirring, the model generates a weak tropically confined Hadley cell.) Coherent Rossby wave packets are generated that resemble those in observations (cf. Lee and Held (1993); Chang and Yu (1999)). The lower layer winds balance the eddy momentum flux convergence, and have a reasonable structure and amplitude.

We study the model sensitivity with three independent model parameters: the mean drag on the lower layer flow, τ_f , the angular speed characterizing the stirring, \bar{u}_A , and the stirring amplitude A (Fig. 2.11).

As the mean drag is reduced, the lower layer westerlies increase proportionally and feed back on the upper layer jet by the thermal wind relationship, but no poleward displacement is observed. There is somewhat little effect on eddy kinetic energy of this increase in meridional shears in the shallow water model (Fig. 2.13), consistent with the view that the way that the barotropic governor reduces eddy amplitudes is not simply by increasing the efficiency of barotropic conversion, but through the baroclinic production that involves interfering with the coupling between upper and lower level disturbances.

As the stirring amplitude increases, eddy amplitudes naturally increase, and the surface westerlies and the jet are displaced polewards. The stronger stirring in the shallow water model leads to more zonal wind deceleration in the subtropics, so the shift in zonal winds is similar to what occurs in the LC1 life cycle. We have not forced the model strongly enough, or at small enough scales, to enter the regime described in

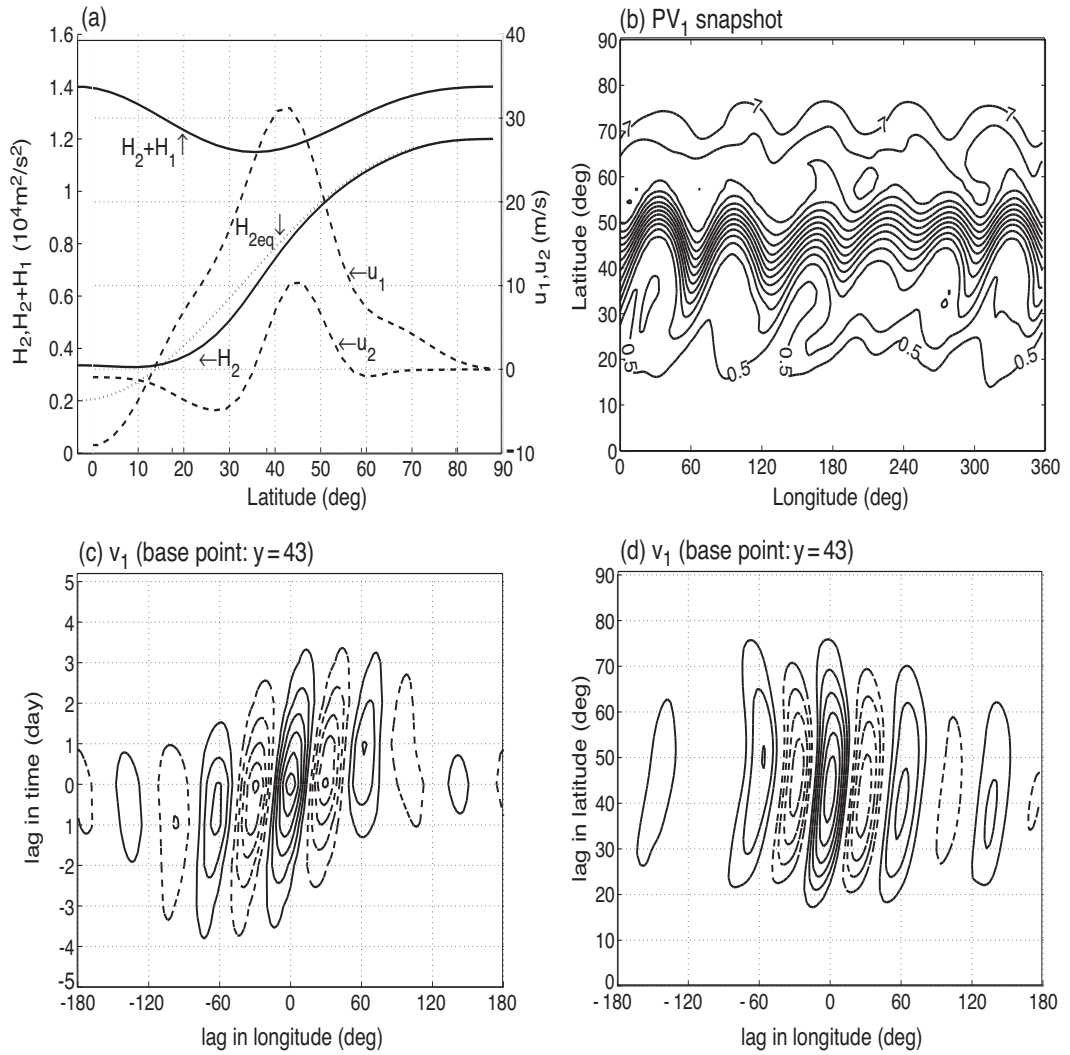


Figure 2.10: The characteristics of the control experiment in the shallow water model: (a) the time and zonally averaged zonal winds and thicknesses; (b) a potential vorticity snapshot; the lag correlation for the meridional wind at 43° in (c) time and longitude, and (d) latitude and longitude. The contour intervals are $0.5 \times 10^{-8} \text{m}^{-2} \text{s}$ for (b), 0.15 for (c) and (d).

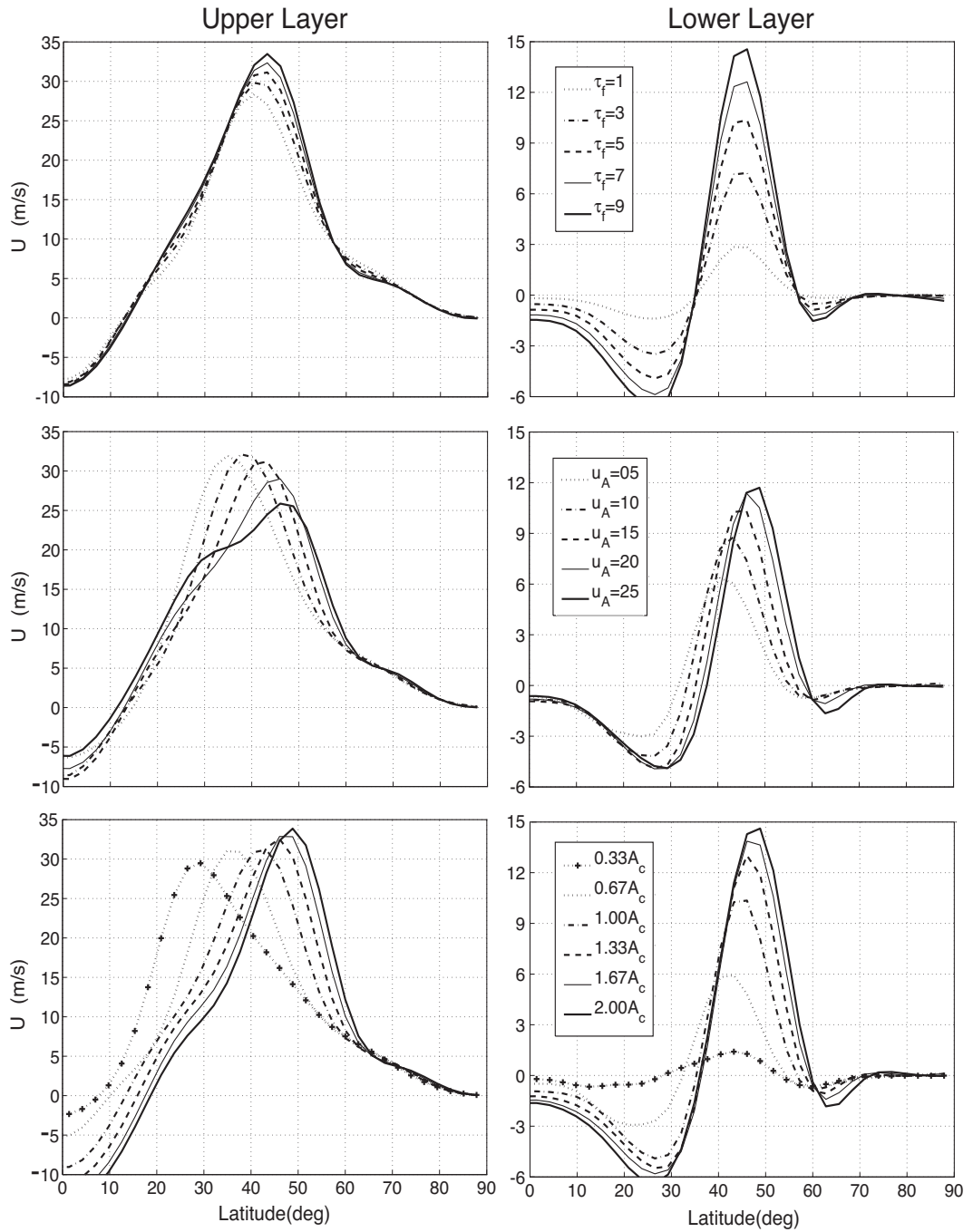


Figure 2.11: The parameter sensitivity study for the shallow water model: the time and zonally averaged zonal winds in the (left) upper layer and (right) lower layer as a function of (top) the mean surface drag, (middle) the prescribed angular speed of the eddy stirring and (bottom) the stirring amplitude.

Orlanski (2003) in which cyclonic wave breaking becomes prevalent. Inspection of the idealized GCM also suggests that this is the case in that model as well. We believe that it is easier to enter the cyclonic regime when modelling zonally asymmetric storm tracks with much stronger local jets.

As the eddies increase in strength, the stronger anticyclonic breaking in the subtropics moves the jet polewards. Since eddy amplitudes decrease as the mean drag is reduced in the idealized GCM, we cannot explain the poleward shift in this way. The shallow water model results do not provide any evidence that either the increase in meridional shears or the decreasing eddy energies are directly responsible for the jet shift.

In contrast, the jet shifts poleward in the shallow water model when the phase speeds in the stirring are increased, with qualitative resemblance to the behavior of the idealized GCM when the mean drag is reduced. The shallow water model eddy momentum flux convergence is plotted as a function of latitude and angular phase speed in Fig. 2.12 for two experiments with different stirring phase speeds. The spectral shift is comparable in structure to that in the GCM mean drag experiments (Fig. 2.7), with a poleward shift in the eddy momentum fluxes accompanying the increase in phase speed.

The three parameters have additionally been varied in a large range of values. As is seen in Fig. 2.11, this jet latitude is especially sensitive to the stirring amplitude, and so we use it as a reference parameter. We gradually increase the stirring amplitude A from $A_c/3$ to $5A_c/3$ by an increment of $A_c/3$ (where A_c is the control value), and for each value of A , we vary the mean drag and angular speed separately. We plot the latitudes of the westerly maximum in the upper layer and in the lower layer as a function of the global mean eddy kinetic energy for these experiments in Fig. 2.13. The latitude of the westerly maximum is obtained by first computing the meridional derivative of the time and zonally averaged zonal winds, and then interpolating for

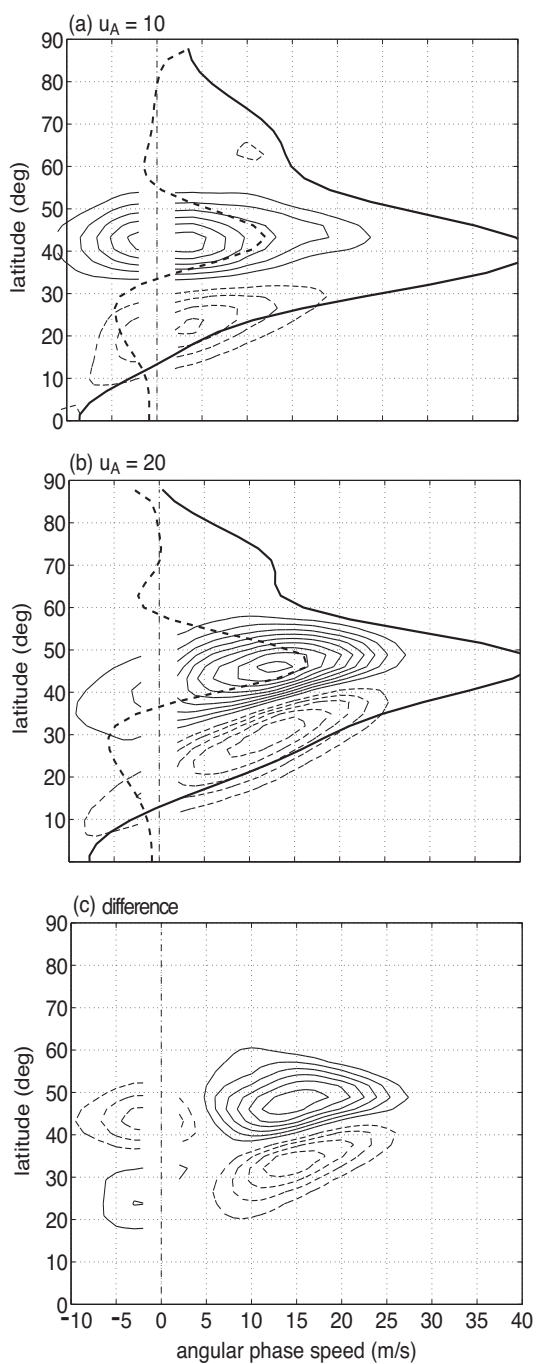


Figure 2.12: As in Fig. 2.7, but for the eddy momentum flux convergence spectra in the shallow water model: (a) $U_A = 10$ m/s, (b) $U_A = 20$ m/s, and (c) the difference ((b)-(a)). The thick lines are the time and zonally averaged angular velocities at the upper layer (solid) and in the lower layer (dashed). The contour interval is 0.0075 m/s/day.

the latitude of zero in the derivative.

The results confirm the robustness of the discussions above, in that the latitudes of westerly wind maxima in two layers are mostly a monotonic function of the model parameters except for several extreme cases. As the stirring amplitude increases, both the upper layer jet latitude and eddy kinetic energy increase for all the experiments, but the lower layer westerly transitions from an equatorward shift to a poleward shift for the smallest stirring amplitudes, as is also noticeable in Fig. 2.11. This transition is more evident in the case of smaller angular speeds prescribed in the stirring, and may be explained by that the critical latitude dynamics starts to take effect only when the eastward eddy phase speeds are sufficiently larger than the subtropical winds, which depends on the strengths of the subtropical eddy stress and the stochastic stirring.

As the mean drag is decreased, the lower layer westerlies stay roughly in the same latitudes for sufficiently large stirrings. The upper layer jet moves poleward slightly, due to the feedbacks from the increased lower level westerlies by the thermal wind relationship, but this is smaller than the effects of increased eddy phase speeds in this shallow water model. In contrast, as the eddy phase speeds are increased, the eddy kinetic energy remains roughly at the same level, but both the upper layer jet and lower layer westerly displace poleward. In summary, the latitude of the lower level westerlies is controlled by the strength and the eastward phase speed of eddies, rather than the barotropic shear altered by the surface friction in this shallow water model.

The size of the jet shift in this shallow water model is less than that in the mean drag runs with the idealized GCM. In Fig. 2.2, the jet shifts poleward 10 degrees as the barotropic wind increases by 10 m/s. But in Fig. 2.11, the jet shifts 10 degrees as \bar{u}_A increases by 20 m/s. In addition, as we have just seen, a reduction in eddy energy as occurs in the idealized GCM should further reduce the amplitude

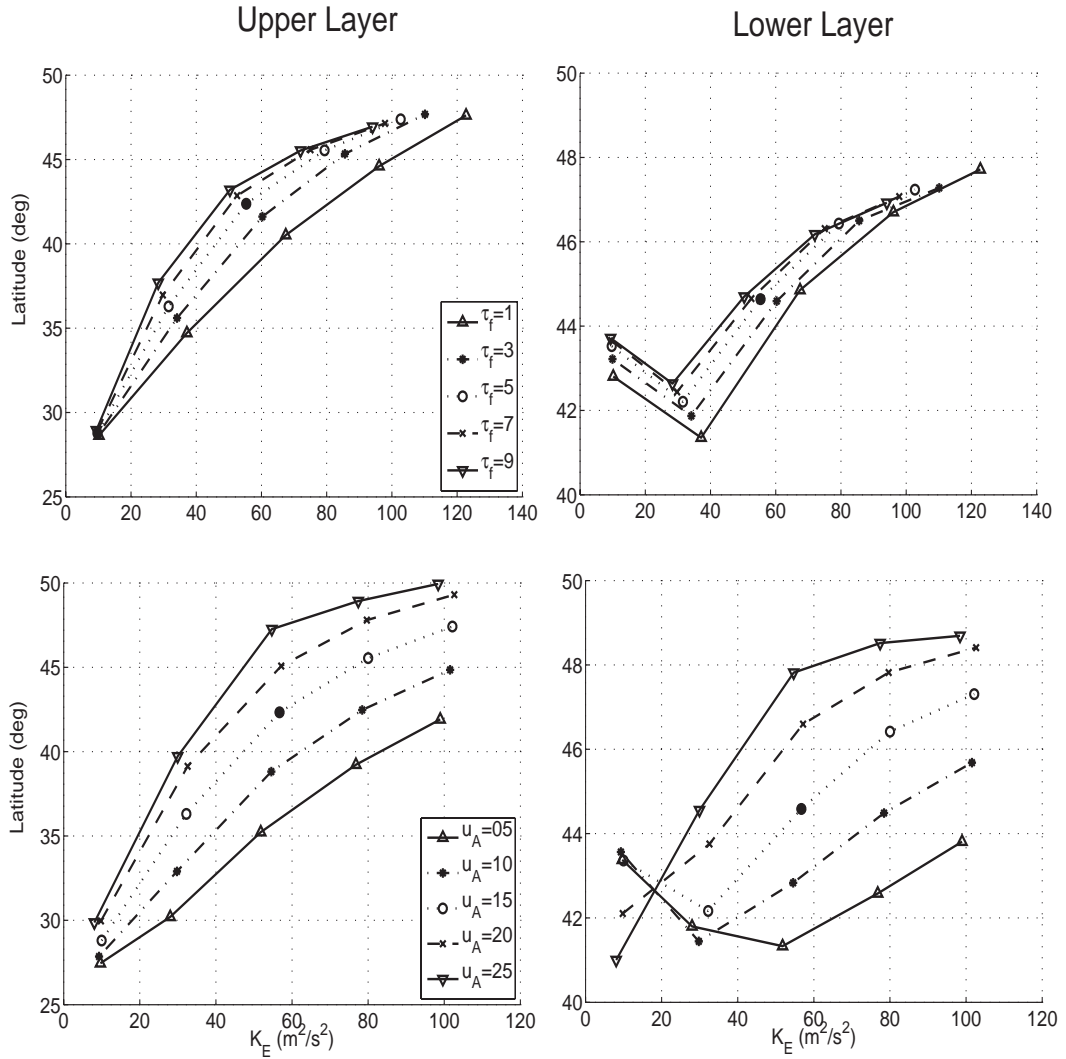


Figure 2.13: The latitudes of the westerly maximum (left) in the upper layer and (right) in the lower layer as a function of the global mean eddy kinetic energy, by varying the stirring amplitude and mean drag (Upper) and the stirring and angular speed (Lower). Each line in the figure denotes the experiments in which the stirring amplitude is increased, and the difference between lines denotes the effects of the mean drag or angular speed. The black closed circle denotes the control experiment.

of the shift. It is possible that this deficiency is due to problems in representing the upper troposphere as a single layer. However, we believe that the main deficiency in this model is that as the jet moves poleward, the stirring emanating from the lower troposphere should also move poleward, following the upper level eddy activity, as implied by the poleward shift of the lower tropospheric heat flux in the GCM (Fig. 2.7). The shallow water model, therefore, excludes an important positive feedback that amplifies the jet response to reduced drag in the full model.

Despite these limitations, we suspect that this shallow water model provides a useful approach towards understanding the jet shift. The model can be further elaborated in several ways, as, for example, by studying in greater detail the wave breaking in the shallow water model as the parameters in this model are varied, or by studying alternative ways of connecting the statistics of the stirring to the statistics of the upper level solution.

2.6 Conclusions and Discussions

The sensitivity to surface friction of the latitude of the surface westerlies and the associated eddy-driven mid-latitude jet is studied in an idealized dry GCM. This latitude is mainly determined by the friction on the zonal mean flow rather than the friction on the eddies, consistent with the conclusion from a two layer model in R97. We also find that the relatively small variation in eddy kinetic energy as the total drag is changed is the result of two competing large effects: a direct increase in eddy energy as the eddy drag is reduced; and an indirect reduction in eddy energy through the effect of meridional shears on baroclinic instability (the barotropic governor) as the mean drag is reduced. We focus on the effects of mean drag in this chapter. Motivated by examination of the space-time spectra of the eddies in the GCM, we construct a shallow water model to study the reaction of the upper tropospheric

dynamics to an increase in the eastward phase speed in the dominant midlatitude eddies. The shallow water calculations support the view that this increase in phase speed is a key ingredient in the poleward shift of the surface westerlies.

Our study suggests that the response of the atmosphere to the change of surface friction on the mean flow can be understood as follows:

- 1 As the surface drag is reduced, the zonal wind acceleration is barotropic and proportional to the surface wind in the extratropics. Meanwhile, the baroclinic eddies are weakened by the increased barotropic meridional shear, but neither the weakening eddies nor the increased meridional shears are directly implicated in the poleward shift.
- 2 The increase in the strength of the westerlies in the extratropics leads to faster eddy phase speeds, while the subtropical zonal winds barely change. Hence, the critical latitude for these eddies is displaced poleward.
- 3 The dynamics of the wave breaking in the upper troposphere, in the presence of this poleward shift in critical latitude, shifts the eddy momentum fluxes polewards, driving a poleward shift in the surface zonal winds and the eddy driven jet. This is particularly supported by the shallow water model results.
- 4 Eddy heat fluxes, and the associated upward EP fluxes tend to follow this upper level eddy activity. This shift in the baroclinic eddy production provides some positive feedback on the upper level shift.

Even when one focuses on the effects of mean drag, there are evidently competing tendencies that must be considered in analyzing the resulting climatic responses. The effects of the phase speed shift may be compensated, in part, by the effects of the reduction in the eddy energy due to the barotropic governor. When the strength of the stirring is reduced in the shallow water model, there is an equatorward displacement

of zonal winds, and we see a similar effect in nonlinear life cycle simulations. The critical latitude shift is apparently dominant over the effect of decreasing eddy energy in our mean drag experiments. We also note that to the extent that the atmosphere is at times in a cyclonic breaking regime due to high eddy amplitude and small eddy length scale as described in Orlanski (2003), a reduction in eddy energy could have the opposite effect of generating poleward movement.

We have confirmed that similar wind shifts occur in the idealized GCM when the change in mean drag is replaced by a prescribed torque approximating the change in mean drag in the GCM experiments. The interactive character of the drag and the zonal mean is not essential for the climatic response, consistent with the dynamics outlined above. It is then natural to inquire as to the dependence of the response on the structure of the imposed torque. We will address this problem in details in chapter 3.

The tropospheric eddy phase-speed mechanism is potentially relevant to many other cases in which the surface westerlies shift in latitude in response to some perturbation, since the strength of the zonal flow that controls the eddy phase speed can be affected by a variety of factors other than surface friction. As an example, tropospheric zonal winds can be modified by a stratospheric zonal torque due to planetary or gravity waves via the "downward control" mechanism (Haynes et al., 1991; Song and Robinson, 2004). The responses of zonal winds and EP fluxes in the troposphere to the idealized stratospheric perturbation in Polvani and Kushner (2002), are qualitatively very similar to the effects of surface drag. Changes in tropospheric phase speeds may play a role in this stratosphere-troposphere coupling context as well. They may also be relevant to the unforced annular mode variability of the tropospheric zonal winds.

The westerlies at the tropopause level in midlatitudes can also be increased by warming the tropical upper troposphere, as in global warming simulations, or by

cooling the polar stratosphere, as in the response to the ozone hole. The increased lower stratospheric and upper tropospheric mean winds may be sufficient to increase eddy phase speeds so as to shift the circulation polewards. These questions are to be explored in details in the following chapters.

2.7 Appendix A: The atmospheric energetics

We present the energy cycle of the large-scale atmospheric circulation described in Lorenz (1967). This approach describes the generation of midlatitude weather systems or storm tracks in a baroclinically unstable atmosphere with an equator-to-pole temperature gradient.

The energy in the atmosphere can be decomposed into eddy kinetic energy K_E , zonal mean kinetic energy K_M , eddy available potential energy P_E , and zonal mean available potential energy P_M .

$$K_E = \left\langle \frac{\overline{u'^2} + \overline{v'^2}}{2} \right\rangle \quad (2.5)$$

$$K_M = \left\langle \frac{\bar{u}^2}{2} \right\rangle \quad (2.6)$$

$$P_E = \left\langle -h \frac{\overline{\theta'^2}}{2} / \frac{\partial \bar{\theta}}{\partial p} \right\rangle \quad (2.7)$$

$$P_M = \left\langle -h \frac{\bar{\theta}_A^2}{2} / \frac{\partial \bar{\theta}}{\partial p} \right\rangle \quad (2.8)$$

Where overbars denote the zonal means, primes denote the deviations from zonal means, $\langle \rangle$ denotes the global average, (u, v) are the zonal and meridional winds, θ is the potential temperature, θ_A is the deviation from a reference temperature, and $h(p)$ is a parameter defined as $h(p) = \frac{R}{p}(p/p_0)^\kappa$.

In a baroclinic model, the energy flows from zonal mean available potential energy,

P_M , to zonal mean kinetic energy, K_M . The starting point is the *baroclinic production*.

$$C(P_M, P_E) = h \frac{\overline{v'\theta'}}{a} \frac{\partial \bar{\theta}}{\partial \phi} / \frac{\partial \bar{\theta}}{\partial p} \quad (2.9)$$

In particular, the energy conversion for the eddy kinetic energy, K_E , is,

$$\frac{\partial K_E}{\partial t} = - \langle h(\overline{\omega'\theta'}) \rangle - \langle \frac{(\overline{v'u'} \cos \phi)}{a} \frac{\partial}{\partial \phi} (\frac{\bar{u}}{\cos \phi}) \rangle - D(K_E) \quad (2.10)$$

Where the first term on the right hand side is the *baroclinic conversion* from eddy available potential energy to eddy kinetic energy, $C(P_E, K_E)$, the second term is the *barotropic conversion* from eddy kinetic energy to zonal mean kinetic energy, $C(K_E, K_M)$, and the last term is the dissipation in the planetary boundary layer. In the case of the "barotropic governor" (James and Gray, 1986; James, 1987), the barotropic meridional shears can alter the rate of barotropic conversion, but it is also possible that the rate of baroclinic conversion is weakened by directly suppressing the baroclinic production.

2.8 Appendix B: The shallow water model of upper troposphere

2.8.1 The conceptual model

The basis for the shallow water model is that Rossby waves are generated for the flow over a wavy lower boundary, providing the source of wave activity for Rossby wave propagation in the conceptual barotropic model in the introduction. More exactly, consider a layer of homogeneous, inviscid and incompressible fluid with a flat top boundary H_0 and a wavy lower boundary $h_s(x, y)$. The thickness of the fluid layer is $h(x, y) = H_0 - h_s(x, y)$. The configuration for the shallow water model is

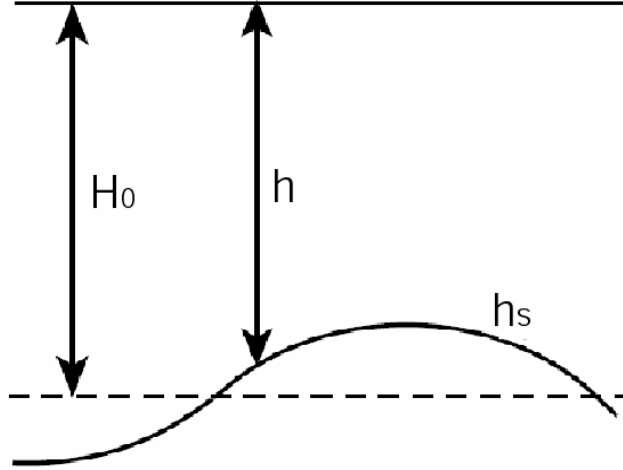


Figure 2.14: A schematic diagram for the shallow water model. The top boundary H_0 is flat, the lower boundary h_s is wavy in the zonal direction, and the layer thickness is $h = H_0 - h_s$.

illustrated in Fig. 2.14.

The zonal momentum and thickness equations for the shallow water model are,

$$\frac{\partial u}{\partial t} = (f + \zeta)v - \frac{\partial}{\partial x} \left(\frac{p}{\rho_0} + \frac{1}{2}(u^2 + v^2) \right) \quad (2.11)$$

$$\frac{\partial h}{\partial t} = \frac{\partial(uh)}{\partial x} + \frac{\partial(vh)}{\partial y} \quad (2.12)$$

Where p is the pressure at a fixed level and ρ_0 is density.

In the quasi-geostrophic approximation (small Rossby number ($f_0 \gg \beta y$) and $f_0 \bar{v}$ is not negligible for large f_0 , and the geostrophic flow is nondivergent), the zonally averaged equations are,

$$\frac{\partial \bar{u}}{\partial t} = f_0 \bar{v} + \overline{v' \zeta'} = f_0 \bar{v} - \frac{\partial(\overline{v' u'})}{\partial y} \quad (2.13)$$

$$\frac{\partial \bar{h}}{\partial t} = \frac{\partial(\overline{v h})}{\partial y} \quad (2.14)$$

We can also write down the Transformed Eulerian Mean (TEM) equations, by

defining the residual meridional circulation $\bar{v}_* \equiv \overline{vh}/H_0$.

$$\frac{\partial \bar{u}}{\partial t} = f_0 \bar{v}_* + \overline{v'q'} \quad (2.15)$$

$$\frac{\partial \bar{h}}{\partial t} = H_0 \frac{\partial \bar{v}_*}{\partial y} \quad (2.16)$$

Where the quasi-geostrophic shallow water potential vorticity is $q' = \zeta' - f_0 h'/H_0$.

Assuming that the top and lower boundaries are rigid, and that there are no mass flux at the northern and southern boundaries, we have zero total mass flux and zero potential vorticity flux.

$$\overline{vh} = \bar{v}\bar{h} + \overline{v'h'} = 0 \quad (2.17)$$

$$\overline{v'q'} = -\frac{\partial(\overline{v'u'})}{\partial y} - f_0 \frac{\overline{v'h'}}{H_0} = 0 \quad (2.18)$$

The eastward flow over topography generates a positive eddy thickness flux, in opposite to the westward deceleration by the mountain torque. The eddy thickness flux is balanced by an equatorward zonal mean flow, analogous to the upper-tropospheric branch of the Ferrell cell. More importantly, the eddy thickness flux generates the eddy momentum flux convergence that is the source of Rossby wave propagation. A numerical example of this model is described in Held and Phillips (1990). Moreover, the lower boundary in this model can also vary in time. In this regard, the lower boundary can be thought of as an isentropic surface, and one can mimic baroclinic instability by randomly stirring the isentropic interface. Here we describe a numerical version of this shallow water model with a stochastic stirring in the isentropic interface.

2.8.2 The numerical model

For simplicity, we consider two layers of an incompressible fluid with densities ρ_1, ρ_2 ($\rho_1 < \rho_2$) rather than two isentropic layers of a compressible ideal gas. The thicknesses of the two layers, multiplied by the reduced gravity $g^* \equiv g(\rho_2 - \rho_1)/\rho_1$ for convenience, are denoted by \mathcal{H}_1 and \mathcal{H}_2 . We allow ourselves the freedom of specifying a latitudinal dependence in the height of the upper boundary at z_{top} and also set $\mathcal{H}_{top} = g^* z_{top}$. The lower boundary is flat. Setting $S \equiv p_s/\rho_1$, where p_s is the surface pressure, the horizontal pressure gradient in the upper layer is

$$-\frac{1}{\rho_1} \nabla p_1 = -\nabla(S - \mathcal{H}_2) = -\nabla(S - (\mathcal{H}_{top} - \mathcal{H}_1)) \quad (2.19)$$

The pressure gradient in the lower layer is also proportional to ∇S , and this term is responsible for the interaction between the two layers.

We use Newtonian relaxation of the interface with strength κ_T , linear damping of momentum meant to represent vertical mixing with strength κ_M , and subgrid hyperdiffusion (∇^8) proportional to κ_v . The equations for the upper layer thickness, vorticity, and divergence are

$$\frac{\partial \mathcal{H}_1}{\partial t} = -\nabla \cdot (\mathbf{v}_1 \mathcal{H}_1) - \kappa_T (\mathcal{H}_1 - \mathcal{H}_{1eq}) - \kappa_v \nabla^8 \mathcal{H}_1 \quad (2.20)$$

$$\frac{\partial \zeta_1}{\partial t} = -\nabla \cdot (\mathbf{v}_1 (f + \zeta_1)) + F_{\zeta_1} - \kappa_M \zeta_1 - \kappa_v \nabla^8 \zeta_1 \quad (2.21)$$

$$\begin{aligned} \frac{\partial D_1}{\partial t} &= -\nabla \cdot ((f + \zeta_1) \mathbf{k} \times \mathbf{v}_1) - \nabla^2 \left(\frac{u_1^2 + v_1^2}{2} + S + \mathcal{H}_1 - \mathcal{H}_{top} \right) \\ &\quad + F_{D_1} - \kappa_M D_1 - \kappa_v \nabla^8 D_1. \end{aligned} \quad (2.22)$$

\mathcal{H}_{1eq} is the equilibrium thickness for the upper layer. Since the shape of the upper boundary is fixed in time, one can equivalently think of relaxing the interface to its

radiative equilibrium value. The forms chosen for \mathcal{H}_{1eq} and \mathcal{H}_{top} are

$$\mathcal{H}_{1eq} = \mathcal{H}_m + \Delta\mathcal{H}(\cos^6 \phi - 0.5) \quad (2.23)$$

$$\mathcal{H}_{top} = 2\mathcal{H}_m + \Delta\mathcal{H}(\cos^6 \phi - \cos^3 \phi) \quad (2.24)$$

The term (F_{ζ_1}, F_{D_1}) represents the vertical momentum fluxes associated with the diabatic mass fluxes, and is only applied to the zonal mean flow for simplicity. It takes the following form in the momentum equations, which can be thought of as the simplest upstream finite-differencing of vertical advection (Shell and Held, 2004).

$$F_{\bar{v}_1} = -(\bar{v}_1 - \bar{v}_2)\max(Q, 0) \quad (2.25)$$

where $Q = -\kappa_T(\bar{\mathcal{H}}_1 - \mathcal{H}_{1eq})/\bar{\mathcal{H}}_1$. This term, and the vertical mixing, are included to prevent excessive upper tropospheric easterlies at the equator. They have little direct effect on the solution in midlatitudes.

The surface pressure S has two parts, a zonal mean component that evolves in time to balance a zonal mean low level wind, and a stochastic eddy part that drives the eddy field. The zonal mean surface pressure is assumed to be in geostrophic balance with the zonal mean lower layer flow; this lower layer flow in turn is determined by predicting a barotropic zonal mean flow \bar{u}_{bt} driven by the eddy momentum fluxes in the upper layer:

$$\frac{\partial \bar{u}_{bt}}{\partial t} = -\frac{\bar{\mathcal{H}}_1}{\mathcal{H}_{top}} \frac{1}{a \cos^2 \phi} \frac{\partial(\overline{v'_1 u'_1} \cos^2 \phi)}{\partial \phi} - \frac{\bar{\mathcal{H}}_2}{\mathcal{H}_{top}} \kappa_f^* \bar{u}_2 - \kappa_v \nabla^8 \bar{u}_{bt} \quad (2.26)$$

$$\frac{1}{a} \frac{\partial \bar{S}}{\partial \phi} = -f \bar{u}_2, \quad \bar{u}_2 = \frac{1}{\mathcal{H}_2} (\mathcal{H}_{top} \bar{u}_{bt} - \bar{\mathcal{H}}_1 \bar{u}_1) \quad (2.27)$$

In Eq. (2.26), the surface drag coefficient is set to be a function of layer thicknesses

$\kappa_f^* = (\bar{\mathcal{H}}_1/\bar{\mathcal{H}}_2)\kappa_f$, and thus, in the steady state,

$$-\frac{1}{a \cos^2 \phi} \frac{\partial(\langle \overline{v'_1 u'_1} \rangle \cos^2 \phi)}{\partial \phi} = \kappa_f \langle \bar{u}_2 \rangle \quad (2.28)$$

where $\langle \rangle$ denotes the time average. By combining Eq. (2.27) with the geostrophic balance in the upper layer, we can obtain the thermal wind relationship in this shallow water model.

$$f(\bar{u}_1 - \bar{u}_2) = \frac{1}{a} \frac{\partial \bar{\mathcal{H}}_2}{\partial \phi} \quad (2.29)$$

The eddy surface pressure S' is assumed to be independent of the upper layer flow, and is generated by a stochastic process,

$$\frac{\partial \nabla^2 S'}{\partial t} = -\frac{\bar{u}_A}{a} \frac{\partial \nabla^2 S'}{\partial \lambda} - \frac{2\Omega}{a^2} \frac{\partial S'}{\partial \lambda} - r_s \nabla^2 S' + \sum_{m,l} \text{Re}(\tilde{\mathcal{E}}_{ml}(t) Y_{ml}(\lambda, \phi)) \quad (2.30)$$

Here \bar{u}_A is the prescribed angular speed, $r_s = 1/\tau_s$ is a frictional damping rate, $Y_{ml}(\lambda, \phi)$ is the spherical harmonic function with the zonal wavenumber m and total wavenumber l , and $\tilde{\mathcal{E}}_{ml}(t)$ is a stochastic forcing (where tilde denotes a complex number). We force the model only within a prescribed range of wavenumbers, and then localize the forcing in midlatitudes by multiplying by a gaussian function in latitude, $G(\phi_0, \phi_w)$ (where ϕ_0 is the maximum latitude, and ϕ_w is the meridional half-width).

$$\sum_{m,l} \tilde{\mathcal{E}}_{ml}(t) Y_{ml}(\lambda, \phi) = AG(\phi_0, \phi_w) \sum_{m,l} \tilde{W}_{ml}(t) Y_{ml}(\lambda, \phi) \quad (2.31)$$

where $\tilde{W}_{ml}(t)$ is generated by a gaussian random variable with unit variance, decorrelated in time and wavenumbers, and A is a parameter with which we control the amplitude of the stirring.

The equation (2.30) is discretized as,

$$\begin{aligned} \frac{\nabla^2 S'(i+1) - \nabla^2 S'(i-1)}{2\Delta t} &= -\frac{\bar{u}_A}{a} \frac{\partial \nabla^2 S'(i)}{\partial \lambda} - \frac{2\Omega}{a^2} \frac{\partial S'(i)}{\partial \lambda} - r_s \nabla^2 S'(i) \\ &+ (2\Delta t)^{-1/2} \sum_{m,l} \tilde{\mathcal{E}}_{ml}(i) Y_{ml}(\lambda, \phi) \end{aligned} \quad (2.32)$$

Where i denotes the i th time step, the factor $(2\Delta t)^{-1/2}$ is included to maintain the same variance as the time step is changed.

In spherical harmonic space, Eq. (2.30) can be written as follows,

$$\frac{\partial \tilde{S}_{ml}(t)}{\partial t} = -(i\omega_R + r_s) \tilde{S}_{ml} - \frac{a^2}{l(l+1)} \tilde{\mathcal{E}}_{ml}(t), \quad \omega_R = m \frac{\bar{u}_A}{a} - m \frac{2\Omega}{l(l+1)} \quad (2.33)$$

Thus, we obtain the frequency spectrum of the eddy surface pressure,

$$|\tilde{S}_{ml}(\omega)|^2 = \frac{a^4}{l^2(l+1)^2} \frac{|\tilde{\mathcal{E}}_{ml}(\omega)|^2}{(\omega - \omega_R)^2 + r_s^2}, \quad (2.34)$$

Here $|\tilde{\mathcal{E}}_{ml}(\omega)|^2$ is the variance of the white noise process. $|\tilde{S}_{ml}(\omega)|^2$ is reddened by the frictional damping r_s and is maximum at the frequency ω_R .

We adopt the following control values for this model, approximately following Held and Phillips (1990) and Vallis et al. (2004).

$$\begin{aligned} \kappa_T^{-1} &= 10 \text{ days}, \quad \kappa_M^{-1} = 100 \text{ days}, \quad \kappa_f^{-1} = 5 \text{ days}, \quad \kappa_s^{-1} = 2 \text{ days} \\ \mathcal{H}_m &= 0.7 \times 10^4 m^2 s^{-2}, \quad \Delta \mathcal{H} = 1.0 \times 10^4 m^2 s^{-2} \\ A_c(2\Delta t)^{-1/2} &= 1.5 \times 10^{-14}, \quad \Delta t = 1200 \text{ seconds} \\ \bar{u}_A &= 15 m/s, \quad \phi_0 = 45^\circ, \quad \phi_w = 15^\circ, \quad 5 \leq m \leq l \leq 12 \end{aligned} \quad (2.35)$$

The shallow water model is run at the same resolution and hyperdiffusion, and is sampled and averaged over the same time periods as is the idealized GCM.

2.9 Appendix C: The space-time spectral analysis

The space-time spectral analysis is a two dimensional harmonic analysis, and is most convenient if the spatial dimension is periodic such as a latitude circle. This approach is useful to detect modes of variability in which the spatial scales are correlated with the temporal scales, and therefore it is ideal to identify wavelike motions. The method was first introduced in Hayashi (1971), and has been widely used for studies of the characters of waves in the atmosphere.

For the time series $v(\lambda, t)$ as a function of longitude λ and time t , we first perform a Fourier transform in longitude at each time.

$$v(\lambda, t) = \sum_m \text{Re}[(C_m(t) - iS_m(t)) \exp(im\lambda)] \quad (2.36)$$

where m is the zonal wavenumber, and $C_m(t)$ and $S_m(t)$ are these cosine and sine coefficients. Then, we perform a Fourier transform to these coefficients in time.

$$C_m(t) = \sum_{\omega} \text{Re}[(A_{m,\omega} - iB_{m,\omega}) \exp(i\omega t)] \quad (2.37)$$

$$S_m(t) = \sum_{\omega} \text{Re}[(a_{m,\omega} - ib_{m,\omega}) \exp(i\omega t)] \quad (2.38)$$

The substitution into Eq. (2.36) yields the

$$v(\lambda, t) = \sum_m \sum_{\pm\omega} \text{Re}[(A_{m,\pm\omega} \mp b_{m,\pm\omega}) - i(\mp B_{m,\pm\omega} + a_{m,\pm\omega})] \times \exp(i(m\lambda \pm \omega t)) \quad (2.39)$$

Therefore, we obtain the spectral power density and the phase for the time series $v(\lambda, t)$ in the wavenumber and frequency space.

$$K_{m,\pm\omega}^v = (A \mp b)^2 + (\mp B - a)^2 \quad (2.40)$$

$$\phi_{m,\pm\omega}^v = \tan^{-1} \frac{(\mp B - a)}{(A \mp b)} \quad (2.41)$$

where + and - correspond to westward and eastward propagating waves, respectively.

If we have two time series $v(\lambda, t)$ and $u(\lambda, t)$, the cospectral power density is,

$$K_{m,\pm\omega}(v, u) = 2[(A^v \mp b^v)(A^u \mp b^u) + (\mp B^v - a^v)(\mp B^u - a^u)] \quad (2.42)$$

$$\text{or} = 2\sqrt{K_{m,\pm\omega}^v K_{m,\pm\omega}^u} \cos(\phi_{m,\pm\omega}^v - \phi_{m,\pm\omega}^u) \quad (2.43)$$

and the quadrature spectrum is

$$Q_{m,\pm\omega}(v, u) = 2\sqrt{K_{m,\pm\omega}^v K_{m,\pm\omega}^u} \sin(\phi_{m,\pm\omega}^v - \phi_{m,\pm\omega}^u) \quad (2.44)$$

Then the coherency spectrum is

$$Coh_{m,\pm\omega}^2(v, u) = \frac{K_{m,\pm\omega}^2(v, u) + Q_{m,\pm\omega}^2(v, u)}{K_{m,\pm\omega}^v K_{m,\pm\omega}^u} \quad (2.45)$$

Following Randel and Held (1991), we can transform the cospectra from wavenumber-frequency space to wavenumber-phase speed $c = (a \cos \phi)\omega/m$ space (angular phase speed $c_A = a\omega/m$). The power spectra in the phase speed space are defined such that the total power is conserved.

$$K_{m,\pm\omega} \Delta\omega = K_{m,\pm c} \Delta c \quad \text{or,} \quad K_{m,\pm\omega} \Delta\omega = K_{m,\pm c_A} \Delta c_A \quad (2.46)$$

and the spectra power density is,

$$K_{m,\pm c} = K_{m,\pm\omega} \frac{m}{a \cos \phi} \quad \text{or,} \quad K_{m,\pm c_A} = K_{m,\pm\omega} \frac{m}{a} \quad (2.47)$$

In practice, the time series is first tapered by a Hanning window $w(t) = 0.5 + 0.5 \cos(\pi t/T)$ (where $(0 \leq |t| \leq T)$). The power spectrum is additionally smoothed by

a normalized gaussian window at a given frequency. The final caveat is that only discrete wavenumbers exist in wavenumber-frequency or wavenumber-phase speed space, although smooth contours are drawn in the figures.

Chapter 3

The Downward Influence of the Stratosphere

3.1 Introduction

Recent observational studies suggest that the variability in the stratospheric flow has a substantial influence on the tropospheric circulation on various time scales. On the time scale of several weeks or months, large anomalies in the strength of the stratospheric polar jet are followed by similar signed anomalies in the tropospheric annular mode that can persist for up to 2 months in both hemispheres (Baldwin and Dunkerton, 1999, 2001; Thompson et al., 2005). In the long-term climate trend, the poleward shift of the Southern Hemisphere surface westerlies in recent decades has been attributed in part to the strengthening of the stratospheric polar vortex due to ozone depletion (e.g. Thompson and Solomon, 2002).

The stratospheric influence on the troposphere is also found in model simulations. The persistence and the trend of the Northern Hemisphere annular mode in a climate model can be strongly affected by the stratospheric polar vortex (Norton, 2003; Scaife et al., 2005). Despite the differences in model details and experiment

designs, a number of idealized models have generated a consistent downward influence of the stratosphere: as the subpolar stratospheric zonal winds are increased, the tropospheric jet displaces poleward, and this poleward displacement projects strongly onto the leading annular mode of intrinsic variability in the troposphere (Polvani and Kushner, 2002; Taguchi, 2003; Song and Robinson, 2004; Kushner and Polvani, 2004; Haigh et al., 2005).

However, the mechanism remains obscure by which the increased lower stratospheric winds lead to the tropospheric jet shift. Previous studies have mainly focused on the effects of the eddy-induced zonal forcings and vertical wind shears in the lower stratosphere. The former can induce a meridional residual circulation that extends downwards and closes in the planetary boundary layer, and this is a zonally symmetric pathway to redistribute momentum in the vertical, generally referred to as "downward control" (Haynes et al., 1991). The wind shears can either affect the vertical propagation and reflection of planetary waves (e.g. Chen and Robinson, 1992; Perlwitz and Harnik, 2003), or modify the baroclinic eddy life cycle in the troposphere (Wittman et al., 2007). But to generate the tropospheric jet shift with a deep annular mode like structure, the tropospheric eddies must be modified (Kushner and Polvani, 2004; Song and Robinson, 2004). This can also be seen in Thompson et al. (2006), in which, despite the downward extension of residual circulations due to stratospheric eddy-induced zonal forcings, the zonal wind changes in the troposphere decrease downwards.

Central to the tropospheric jet shift is the eddy momentum flux, which, in the zonal momentum balance, drives the barotropic component of zonal wind against the frictional damping near the surface. The eddy momentum flux diverges from the subtropics into the midlatitude jet in the upper troposphere, as the midlatitude eddies propagate equatorward and get absorbed near their subtropical critical latitudes, where the eddy phase speed equals the background zonal mean wind (see Held and

Phillips (1987) for a simple example). In a troposphere model, the midlatitude jet displaces poleward as the strength of surface friction is reduced (Robinson, 1997), and we argue in chapter 2 that the increased eastward propagation of midlatitude eddies, due to the accelerated midlatitude jet, play a key role in generating this poleward shift. It is then natural to ask whether increased lower stratospheric winds can modify tropospheric eddies in the same way. As the response to a change in surface friction can be approximated by prescribing a zonal torque to the model (see chapter 2), it is also of value to study the atmospheric response to the structure and location of a zonal torque. Alternatively, one can think of tropospheric annular mode as an internal mode that arises from the aforementioned eddy dynamics in the troposphere, and then think of the tropospheric response as a projection of the external forcing or stratospheric influence onto the internal mode (Song and Robinson, 2004; Ring and Plumb, 2007, hereafter SR and RP, respectively). But one can still think of tropospheric eddy phase speeds as an agent in linking the stratospheric influence with the tropospheric internal mode.

In this chapter, we study the response of the atmosphere to a prescribed zonal torque in a systematic manner. We first examine the process that gives rise to the tropospheric jet shift, when a zonal torque is applied in the troposphere, as in RP, and then explore the stratospheric influence on the tropospheric jet with a zonal torque in the stratosphere, as in SR. This study is also motivated by an attempt to understand the model sensitivity when tuning the orographic gravity wave drag (GWD) in climate models. While the orographic GWD is localized above the steep topography, an adjustment of the GWD profile in the vertical has an impact on the global circulation, including meridional shifts of the midlatitude jet (e.g. Stephenson, 1994). To the extent that the zonal mean response is mainly caused by the GWD on the zonal mean flow, it is of value to examine the jet sensitivity to the vertical level of a zonal torque in a simple model.

In this study, we use the idealized dry model described in Held and Suarez (1994) with enhanced stratospheric resolution. In contrast to previous model studies on stratosphere-troposphere coupling, this model does not have a stratospheric polar jet. This configuration minimizes stratospheric intrinsic variability and its influence on the troposphere in the control simulation, and helps to isolate the dynamical process that generates the model response to external forcings. The forced response in this model is similar to that in models with a stratospheric polar jet, suggesting that the insights we obtain here may also be relevant even when the stratosphere-troposphere coupling in the basic state is active.

The model results support the importance of the phase speeds and critical latitudes of tropospheric eddies on the jet shift in response to the prescribed zonal forcing. A westerly torque, when placed in the extratropical stratosphere or on the poleward flank of the jet in the troposphere, results in a poleward jet shift. This jet shift can be explained by the increased tropospheric eddy phase speeds, due to the eastward acceleration of the tropospheric torque or the downward influence of the stratospheric torque. When analyzing the contributions to the stratospheric influence in this model, we find that the changes in the stratospheric eddies play a more important role than the induced residual circulations.

The chapter is organized as follows. We first describe the characteristics of the idealized dry model and control simulation in section 3.2. Then, we present a sensitivity study of the tropospheric jet latitude with respect to the location of the zonal torque in section 3.3. Next, we examine the processes that give rise to the tropospheric jet shift for a tropospheric torque in section 3.4, and for a stratospheric torque in section 3.5. Particularly, we attempt to separate the direct response to external forcings from the projection onto the tropospheric internal variability. In section 3.6, we discuss the implications for the jet sensitivity with the orographic GWD parameterization in a climate model. We provide a brief summary and discussion in section 3.7. Finally,

we present a short summary for the Eliassen-Palm (EP) fluxes in Appendix A and the Empirical Orthogonal Function (EOF) analysis in Appendix B.

3.2 The idealized dry model

3.2.1 The model configuration

We employ the GFDL spectral atmospheric dynamical core. The model uses a sigma vertical coordinate, with the vertical differencing scheme described in Simmons and Burridge (1981). The sigma value on the k th half level $\sigma_{k+1/2}$ is defined by the following profile so as to attain a high resolution in the stratosphere.

$$\sigma_{k+1/2} = \exp(-\gamma(1 - k/N)^\alpha), \quad k = 0, \dots, N \quad (3.1)$$

Where N is the total number of model levels, γ and α are two constants. The values of γ and α are obtained by specifying the model upper boundary as $\sigma_{1/2} = \exp(-\gamma) = 1 \times 10^{-5}$ and the median vertical level as $\sigma_{N/2+1/2} = \exp(-\gamma 0.5^\alpha) = 0.1$. As a result, about half of the model levels lie in the stratosphere.

A sponge layer is applied in the top model levels to prevent artificial wave reflection at the upper boundary. Following Scott and Polvani (2006), we use linear Rayleigh damping only on the eddies in the momentum equations, as the damping on the zonal mean flow may induce unwanted downward influence. The damping coefficient is specified as $\kappa_{sp}((\sigma_{sp} - \sigma)/\sigma_{sp})^2$ (for $\sigma < \sigma_{sp}$), in which the lowest level of the sponge layer is $\sigma_{sp} = 5 \times 10^{-4}$, and the maximum damping rate is $\kappa_{sp}^{-1} = 0.5$ days.

The model is forced by zonally symmetric Newtonian relaxation to the prescribed equilibrium temperature field, with constant temperatures in the stratosphere, and damped by Rayleigh friction near the surface, as in Held and Suarez (1994). The model uses a flat lower boundary and excludes stationary planetary waves, but there

exist instantaneous planetary waves that are important for stratospheric signals to propagate downwards. The hyperdiffusion (∇^8) is set so that the diffusive damping time of the smallest retained spherical harmonic is 0.1 days. The model is run with T42 horizontal resolution and 40 vertical levels. The model output is sampled daily, and the time averaged results are averaged over the last 5200 days of the 6000-day integration. In all the simulations, the forcings and dampings are hemispheric symmetric, and the similarity between the climatologies in both hemispheres confirms the robustness of our results.

3.2.2 The control simulation

Figure 3.1 shows the time and zonally averaged zonal wind, and the regressions of the zonally averaged zonal wind and Eliassen-Palm (EP) flux divergence anomalies on the standardized annular mode index in the control experiment. The annular mode index here is defined as the first principal component of the zonally and daily averaged surface pressure in one hemisphere. The climatological mean zonal wind displays a tropospheric jet with the maximum wind at about the latitude 40° and sigma level $\sigma = 0.25$. The regression maps show that the midlatitude jet vacillates about the mean latitude with anomalous westerlies at 50° and easterlies at 30° , associated with anomalous baroclinic eddy generation near the surface and anomalous meridional wave propagation in the upper troposphere. The extratropical winds in the stratosphere are weak in the climatological mean and display relatively little variability, as expected from the isothermal radiative equilibrium temperature in the stratosphere. The EP vector regression map indicates that some of the tropospheric waves can propagate into the midlatitude lower stratosphere, and then get refracted back into the subtropical upper troposphere. In comparison with the statistics in Held and Suarez (1994), the mean tropospheric jet in this model is shifted slightly equatorward, and the low frequency jet vacillation is more persistent, as is also found

in Gerber et al. (2007).

We describe eddy characters with the latitude-phase speed spectrum described in Randel and Held (1991). The 5200-day time series is divided into 13 subsections of length $T = 400$ days and tapered by a Hanning window. Each subsection is transformed to the wavenumber and frequency space, and then converted to the wavenumber and angular phase speed space. In this figures, we use angular phase speeds multiplied by the Earth radius (phase speeds divided by $\cos \theta$) for comparison with the zonal winds. The resolution in angular phase speed space Δc_A is limited by the time period T and zonal wavenumber m , $\Delta c_A = a(2\pi/T)/m$ (where a is the Earth radius). Since the troposphere is dominated by medium-scale eddies ($4 \leq m \leq 7$) in the model, we neglect the small contribution of $m = 1$ to the tropospheric eddy spectra.

Figure 3.2 shows the eddy momentum flux convergence in the upper troposphere ($\sigma = 0.230$) and eddy heat flux in the lower troposphere ($\sigma = 0.843$) as a function of latitude and angular phase speed in the control experiment. The figure displays the familiar eddy momentum flux divergence slightly poleward of the subtropical critical latitudes, and momentum flux convergence into the midlatitude jet in the upper troposphere, as well as the poleward heat flux in the lower troposphere. Both the momentum and heat fluxes are dominated by eddies with angular phase speeds between 0 and 10 m/s, with a peak around 5 m/s. These dominant phase speeds are slower than the observed values in Randel and Held (1991), which might be related to the increased low frequency jet persistence in the model.

3.3 A sensitivity study

In this section, we examine the sensitivity of the tropospheric jet latitude to a time-independent and zonally symmetric zonal torque. The zonal torque is identical in

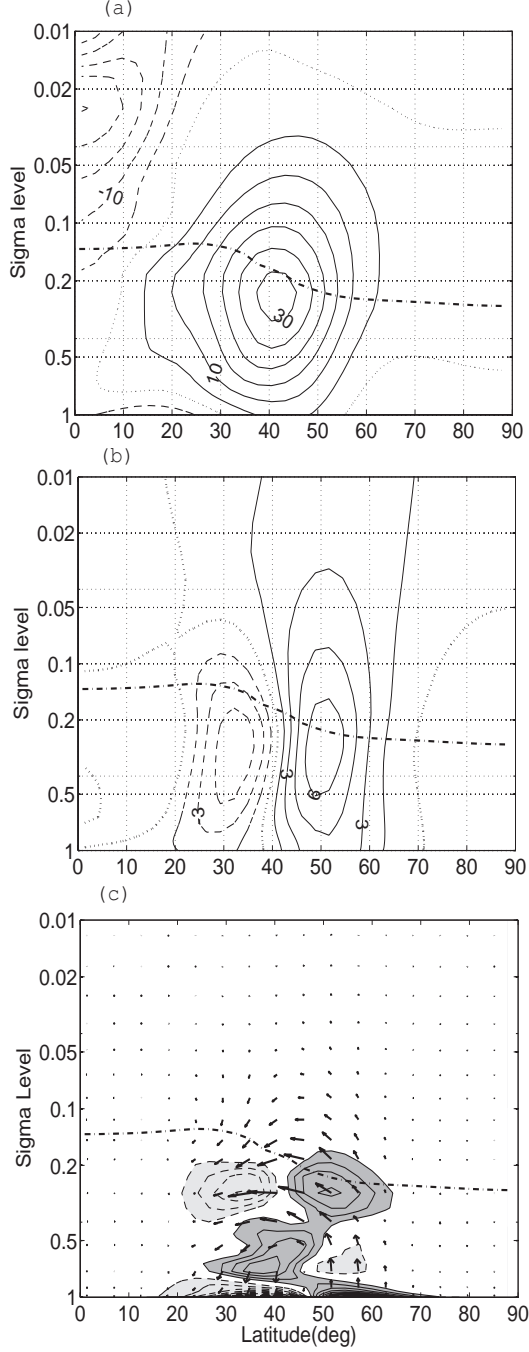


Figure 3.1: The control simulation: (a) the time and zonally averaged zonal wind, and the regressions of (b) the zonally averaged zonal wind and (c) EP flux divergence anomalies on the standardized annular mode index. The dashdotted lines in the plots are the tropopause level, estimated by the standard WMO lapse-rate criterion. The contour intervals are 5m/s for (a), 1.5m/s for (b), 0.5m/s/day for (c). The dark (light) shading in (c) denotes the EP flux divergence (convergence). The EP vectors in (c) denote the wave activity fluxes of $4 \text{ m/s/day} \times (\Delta\sigma, \Delta\phi)$ (where $(\Delta\sigma, \Delta\phi)$ are the lengths of the vectors projected on the vertical level and latitude, respectively), and the vectors are plotted on selected grid points representative of the wave activity pattern.

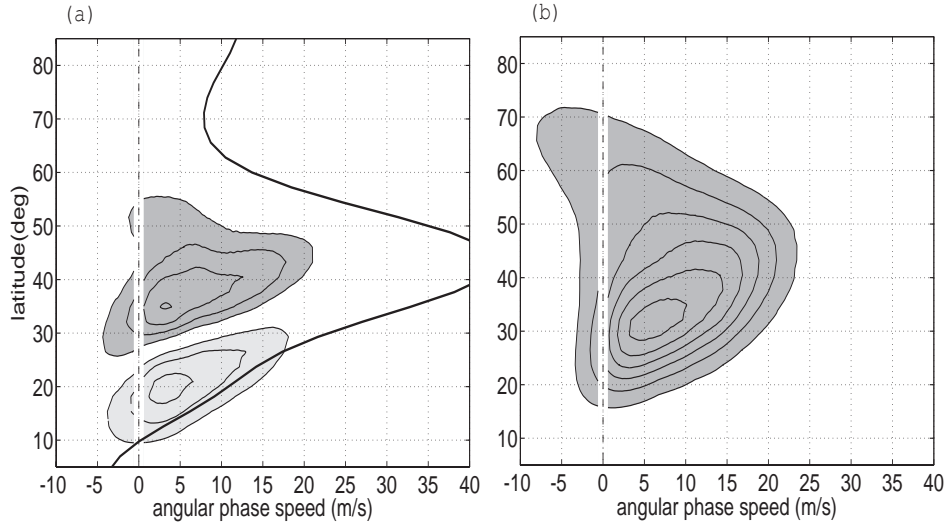


Figure 3.2: The control simulation: (a) the eddy momentum flux convergence in the upper troposphere ($\sigma = 0.230$) and (b) eddy heat flux in the lower troposphere ($\sigma = 0.843$) as a function of latitude and angular phase speed. The thick solid line in (a) is the time and zonally averaged zonal wind at $\sigma = 0.230$, divided by $\cos\phi$ for comparison. The contour intervals are 0.03 m/s/day for (a) and 0.08 Km/s for (b). The dark (light) shading denotes positive (negative) values.

both hemispheres, in contrast to the dipolar structure used in SR and RP. This introduces an angular momentum source to the model, which is eventually removed by the surface friction in the same hemisphere, and therefore it is not necessary to impose an angular momentum source in one hemisphere and a sink in the other. The zonal torque T has the following form.

$$\begin{aligned}
 T &= A_0 G(\phi) \cos(\eta(\sigma)\pi), \quad -0.5 \leq \eta(\sigma) \leq 0.5 \\
 &= 0, \quad \text{elsewhere}
 \end{aligned}
 \tag{3.2}$$

Where A_0 is the forcing amplitude. When the amplitude of A_0 is increased or the sign is changed, the tropospheric response is fairly linear, as is also seen in SR and RP. Therefore, we focus on the jet response to the location of a westerly (eastward) torque with fixed amplitude $A_0 = 2$ m/s/day, which generates a zonal wind response of comparable magnitude to the internal wind variability in the model. $G(\phi)$ controls

the meridional structure of the torque, with a gaussian function in latitude, in which the maximum forcing latitude is ϕ_0 and the meridional half-width is $\phi_w = 9^\circ$. The factor $\cos(\eta(\sigma)\pi)$ controls the vertical structure, in which $\eta(\sigma)$ is centered at the forcing level σ_0 , with a linear vertical profile when σ_0 is below the sigma level 0.3, and with a logarithmic profile when σ_0 is above this level.

$$\begin{aligned}\eta(\sigma) &= (\sigma_0 - \sigma)/\sigma_w, & (\sigma_0 \geq 0.3, \sigma_w = 0.3) \\ &= (\log_{10} \sigma_0 - \log_{10} \sigma)/e_w, & (\sigma_0 \leq 0.3, e_w = 1.0)\end{aligned}\tag{3.3}$$

We perform a comprehensive sensitivity study with respect to the location of the torque (ϕ_0, σ_0) . Most experiments display a tropospheric jet shift similar in structure to the tropospheric annular mode (e.g. Figs. 3.5 and 3.10). Therefore, we describe the jet shift briefly by regressing the zonal wind change $\delta U(\phi, \sigma)$, in a least square manner, to the internal annular mode pattern $U_{AM}(\phi, \sigma)$ in Fig. 3.1b.

$$\delta U(\phi, \sigma) = \beta U_{AM}(\phi, \sigma) + \epsilon\tag{3.4}$$

Here δU and U_{AM} are mass-weighted at each latitude and sigma level before the regression. The regression coefficient β represents the forced jet movement relative to the internal jet variability, with the positive (negative) sign indicating a poleward (an equatorward) shift. Therefore, the zonal wind response for $\beta = 1$ is similar in magnitude to the wind variability associated with one standard deviation of the annular mode index in the control simulation.

Figure 3.3 shows the jet shift as a function of the forcing location. First, we study the dependence on the forcing level, for the torque on the equatorward flank ($\phi_0 = 30$) and poleward flank ($\phi_0 = 50$) of the jet center. The torque in Fig. 3.3a is placed on the vertical levels $\sigma_0 = 0.85, 0.65, 0.45, 0.1, 0.056, 0.032, 0.01, 0.003$. As the torque is moved upwards in the troposphere, the annular mode-like response is

almost unchanged. This result seems to be counterintuitive, as one may think that the torque at the surface would have an opposite effect on the vertical wind shears and the associated baroclinic instability to the torque in the upper troposphere. Moreover, the jet shifts poleward for the westerly torque at all levels on the poleward flank of the jet. But for the torque on the jet's equatorward flank, the jet movement reverses in direction near the forcing level $\sigma = 0.1$. As the torque is moved aloft in the stratosphere, the tropospheric response eventually becomes negligible.

The vertical integral of angular momentum added at the forcing latitude, $\int T d\sigma = \int A_0 \cos(\eta(\sigma)\pi) d\sigma$, remains roughly constant for the torque in the troposphere, and decays exponentially with increasing height for the torque in the stratosphere (Fig. 3.3b). The tropospheric jet response to a stratospheric torque, although the mass-weighted average is small, can be at least comparable in magnitude to the response to a tropospheric torque, which suggests that the direct contribution of the zonal torque to the angular momentum balance is not the key for the jet shift, especially for a stratospheric torque.

Next, we look at the response to the torque location in a latitude-sigma level domain below the lower stratosphere. The torque is placed in the latitudes from 20° to 70° with increments of 10° , and on the sigma levels $\sigma_0 = 0.85, 0.65, 0.45, 0.1, 0.056$. (Note that the wind response is very large for the stratospheric torque in the subtropics, and the time step for the model integration is reduced by half to avoid numerical instability.) As the torque near the surface ($\sigma_0 = 0.85$) is moved from low latitudes to high latitudes, the jet response makes the transition from an equatorward shift to a poleward shift near the forcing latitude 35° . The jet shifts poleward for a westerly torque at the latitude of the surface westerly maximum, consistent with the response to a decrease in surface friction in chapter 2. As the torque is moved from near the surface to the middle troposphere, the jet response does not change very much. However, in the upper troposphere and lower stratosphere, the transitional

latitude tilts equatorward. In particular, the tropospheric jet shifts poleward for the torque placed poleward of 30° in the lower stratosphere ($\sigma_0 = 0.056$).

Figure 3.4 shows the time and zonally averaged zonal wind response for three cases in which the zonal wind change explained by the internal annular mode is less than 60%. For the case of ($\phi_0 = 20^\circ, \sigma_0 = 0.056$), the imposed torque is mainly balanced by Coriolis deceleration, and the small Coriolis parameter in the subtropics results in an extremely large response in meridional winds and zonal winds. In the other two experiments, the torques are moved across the tropopause and the jet center, and simultaneously, the responses make a transition from an equatorward jet shift to a poleward shift. In the following sections, we study the dynamical processes for the experiments in which the response is well projected onto the internal annular mode.

3.4 Response to the tropospheric forcing

We study the response to a tropospheric torque mainly by comparing two experiments, in which the zonal torques near the surface ($\sigma_0 = 0.85$) are placed on the equatorward flank ($\phi = 30^\circ$) and poleward flank ($\phi = 50^\circ$) of the jet center. Figure 3.5 shows the time and zonally averaged responses in the zonal wind and EP flux divergence. The response displays a large-scale pattern in the zonal wind and wave activity, which is highly correlated with the internal annular mode in both the stratosphere and troposphere, but of the opposite sign for the two cases. The wind change shows little resemblance to the external forcing, suggesting that it is useful to think of the response as a projection onto the internal annular mode. For the torque placed on the jet's poleward flank, a westerly wind anomaly is seen in the subtropical upper troposphere as the result of the poleward jet shift, implicative of the separation of the eddy-driven jet from the subtropical jet.

We first show the model response without eddy feedbacks in a zonally symmet-

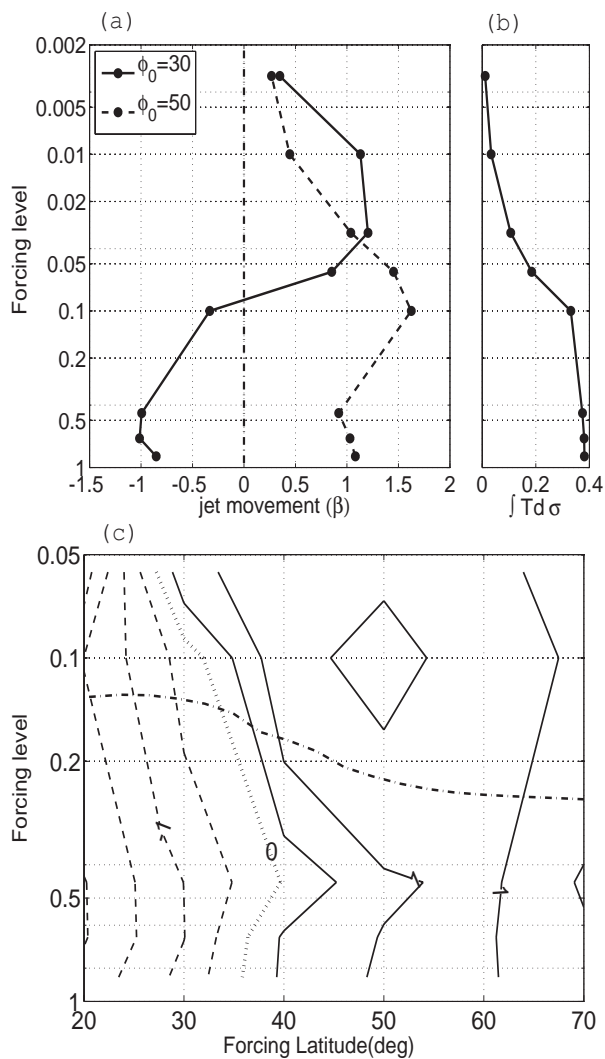


Figure 3.3: Sensitivity of the tropospheric jet latitude to the forcing location. The jet movement β is defined in Eq. (3.4) as the forced jet movement relative to the internal jet variability. β is shown as a function of (a) the forcing level on the jet's equatorward flank ($\phi_0 = 30$) and poleward flank ($\phi_0 = 50$) and (c) the forcing latitude and the forcing level. The dashdotted line in (c) is the tropopause level in the control simulation. The vertical integral of angular momentum added at the forcing latitude, $\int T d\sigma$, is shown in (b) for reference as a function of the forcing level.

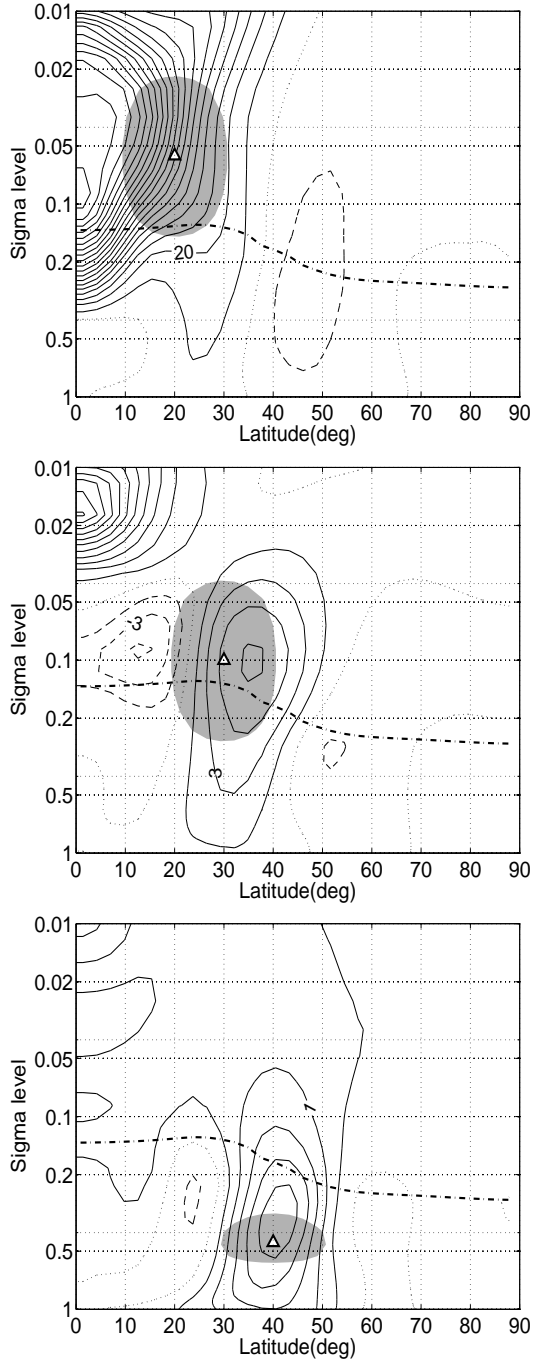


Figure 3.4: The time and zonally averaged zonal wind response for the three cases, in which the zonal wind response explained by the internal annular mode is less than 60%. The triangular symbol denotes the forcing center, and the shading denotes the region where the torque is greater than 0.5 m/s/day. The forcing locations are (top) ($\phi_0 = 20^\circ, \sigma_0 = 0.056$), (middle) ($\phi_0 = 30^\circ, \sigma_0 = 0.1$), (bottom) ($\phi_0 = 40^\circ, \sigma_0 = 0.45$), and the contour intervals are (top) 5 m/s, (middle) 1.5 m/s and (bottom) 0.5 m/s.

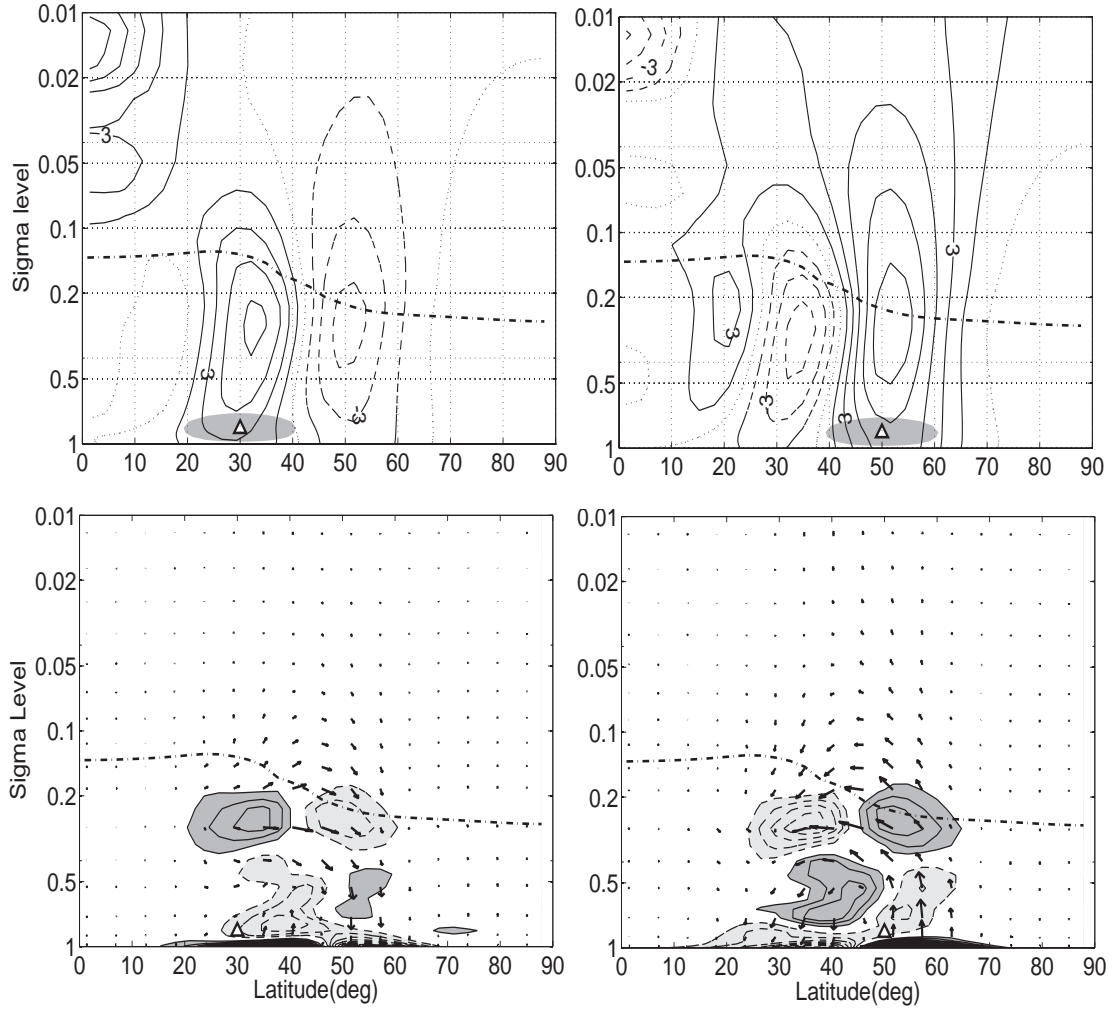


Figure 3.5: The time and zonally averaged responses in the (top) zonal wind and (bottom) EP flux divergence, for the zonal torques near the surface ($\sigma_0 = 0.85$) that are placed on the jet's (left) equatorward flank ($\phi_0 = 30$) and (right) poleward flank ($\phi_0 = 50$). The triangular symbol denotes the forcing center, and the dark shading in the top panels denotes the region where the torque is greater than 0.5 m/s/day, and the dark (light) shading in the lower panels denotes the EP flux divergence (convergence). The dashdotted lines in the plots are the tropopause level in the control simulation. The contour intervals are 1.5 m/s for the zonal wind, 0.5 m/s/day for the EP flux divergence, and 4 m/s/day $\cdot(\Delta\sigma, \Delta\phi)$ for the EP vectors.

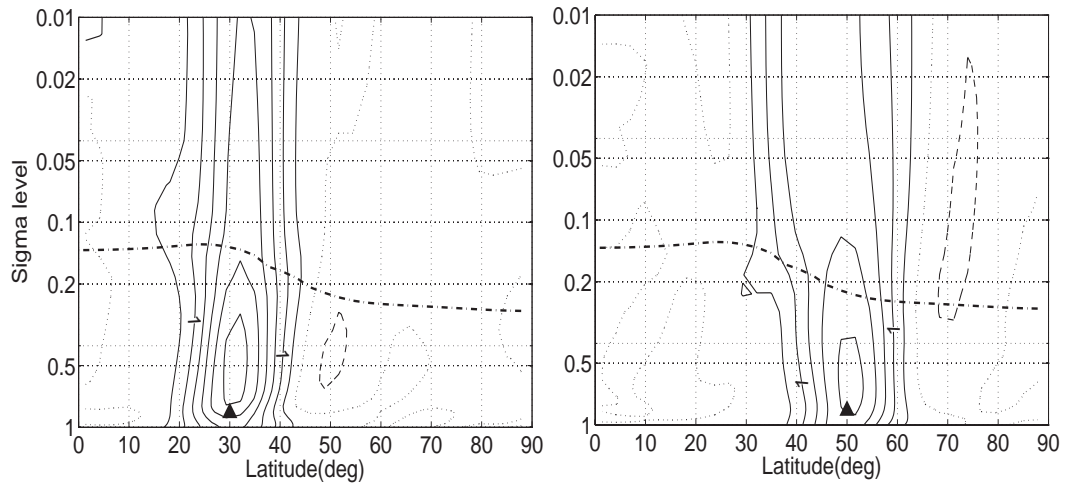


Figure 3.6: The zonal wind responses in a zonally symmetric model for the same surface zonal torques on the jet’s (left) equatorward flank and (right) poleward flank as in Fig. 3.5. The triangular symbol denotes the forcing center. The dashdotted lines in the plots are the tropopause level in the control simulation. The contour interval is 0.5 m/s.

ric model. The model is constructed by making the full model axisymmetric and including the eddy forcings in the control simulation, with the method described in Kushner and Polvani (2004). We integrate the model for 2000 days, and obtain a steady state solution that matches the control climatology except in the deep tropics. Figure 3.6 shows the zonal wind responses for the same surface torques in this model. The zonal wind change displays a fairly barotropic structure from near the surface into the stratosphere, with a slight decrease across the tropopause. This response is expected from the downward control theory, as the forced residual meridional circulation is confined in the planetary boundary layer (Robinson, 2000). The wind changes appear only in the forced latitudes, showing clearly that the jet shift is primarily driven by eddy feedbacks.

The eddy feedbacks are examined with the latitude-phase speed spectra of the upper level eddy momentum flux convergence and lower level eddy heat flux (Fig. 3.7). The response for the torque on the jet’s poleward flank occurs in the midlati-

tudes, with a poleward shift in the upper tropospheric critical latitudes of dominant eddies, associated with an increase in phase speed seen in the spectra of both the eddy momentum flux and heat flux. In contrast, the response for the subtropical torque appears in both the midlatitudes and subtropics, with an equatorward shift in the critical latitudes of nearly all the eddy phase speeds in the climatology, accompanied by an increase in phase speed in the subtropics and a slight decrease in the midlatitudes.

We argue that the full model response can be thought of as a zonally symmetric balance between the prescribed zonal torque and surface friction at first, followed by the subsequent modifications on the eddies and the eddy-driven zonal flow. In the absence of eddy feedbacks, a westerly torque near the surface generates a barotropic increase in the zonal wind. The increased zonal wind on the poleward flank of the jet accelerates the eastward propagation of midlatitude eddies, and thus brings the subtropical critical latitudes poleward. This is observed in the transient adjustment in a model when the surface friction is reduced suddenly in Chen et al. (2007). In contrast, the increased zonal wind in the subtropics allows the midlatitude eddies to penetrate further into the tropics and push the subtropical critical latitudes equatorward. This is consistent with Seager et al. (2003), which argues that the increased subtropical winds in the warm phase of the ENSO cycle permit the equatorward shift in the meridional propagation and refraction of Rossby waves. As the eddy-driven circulation moves equatorward, the midlatitude eddy phase speeds are also seen to decrease somewhat in the lower level heat flux spectra, which can be thought of as a positive feedback.

Despite the difference in the phase speed spectra, the eddy momentum fluxes in both cases display a similar change in eddies with angular phase speeds between 10 m/s and 20 m/s, faster than the dominant eddies in the control climatology. These eddies are responsible for the annular mode-like responses for the zonal mean wind

and EP flux divergence in Fig. 3.5, as the contributions to the subtropical divergence from slower eddies are either too small or cancelled out in the zonal average. The climatological eddy momentum fluxes for these fast eddies transition from divergence to convergence between the latitudes 30° and 40° . A zonal torque placed at these latitudes is likely to modify both the zonal mean wind and eddy phase speed, and thus results in smaller changes in the critical latitudes, which is consistent with the jet movement in latitude for a tropospheric torque shown in Fig. 3.3c (Note that there is no jet shift for a surface torque at about 35° , whereas the jet latitude is at about 40°).

The eddy responses are further examined in zonal wavenumber-phase speed spectra. Figure 3.8 shows the eddy momentum flux averaged between 35° and 45° and eddy heat flux averaged between 45° and 55° , with a cosine weighting in latitude. The latitude bands are chosen to capture the characters of anomalous eddy momentum flux and heat flux maxima associated with the jet movement. The response to a torque on the jet's poleward flank displays an increase in phase speed in both the momentum flux and heat flux, roughly following the slope of the dispersion relationship. The cancellations of dominant eddies ($m=5-6$), when summed over wavenumbers, result in the largest contribution from shorter ($m=6-8$) and faster eddies seen in the latitude-phase speed spectra. These faster eddies also appear in the response to a subtropical torque, but the change in dominant eddies is relatively small.

While it seems plausible that the eddy-driven circulation follows the poleward shift in the critical latitudes, the nonlinear modification of barotropic flow on the eddy-driven jet is rather complex, even in a single baroclinic eddy life cycle. Simmons and Hoskins (1980) and Thorncroft et al. (1993) have varied the barotropic shear on the equatorward flank of the jet in the initial condition, and obtain two distinct types of life cycle (LC). In LC1, the wave breaking is primarily on the anticyclonic side of the jet, and the final jet position moves to the poleward flank of the initial jet. In LC2,

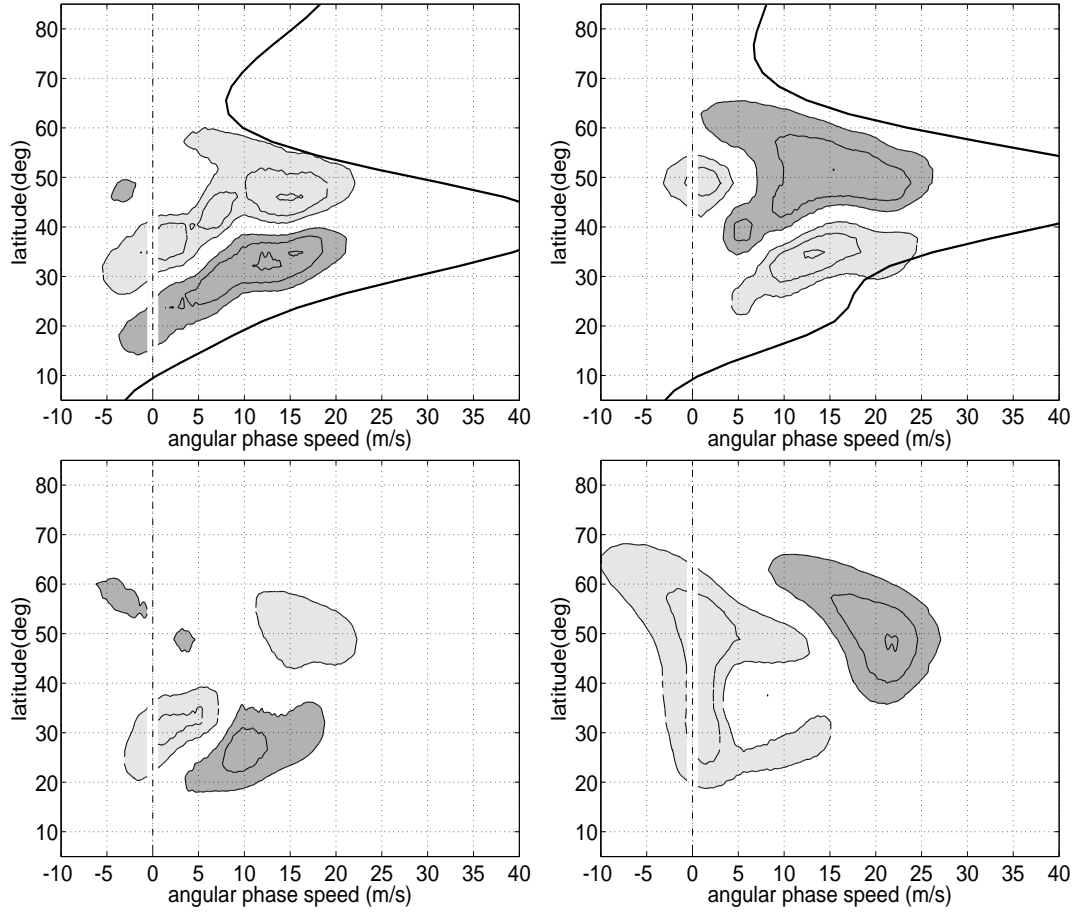


Figure 3.7: The responses in the latitude-phase speed spectra of the (top) upper level ($\sigma = 0.230$) eddy momentum flux convergence and (bottom) lower level ($\sigma = 0.843$) eddy heat flux, for the same surface torques on the jet's (left) equatorward flank and (right) poleward flank as in Fig. 3.5. The thick solid lines in the top panels are the time and zonally averaged upper level ($\sigma = 0.230$) zonal winds, divided by $\cos\phi$ for comparison. The contour intervals are 0.015 m/s/day for the momentum flux convergence and 0.04 Km/s for the heat flux. The dark (light) shading denotes the positive (negative) value.

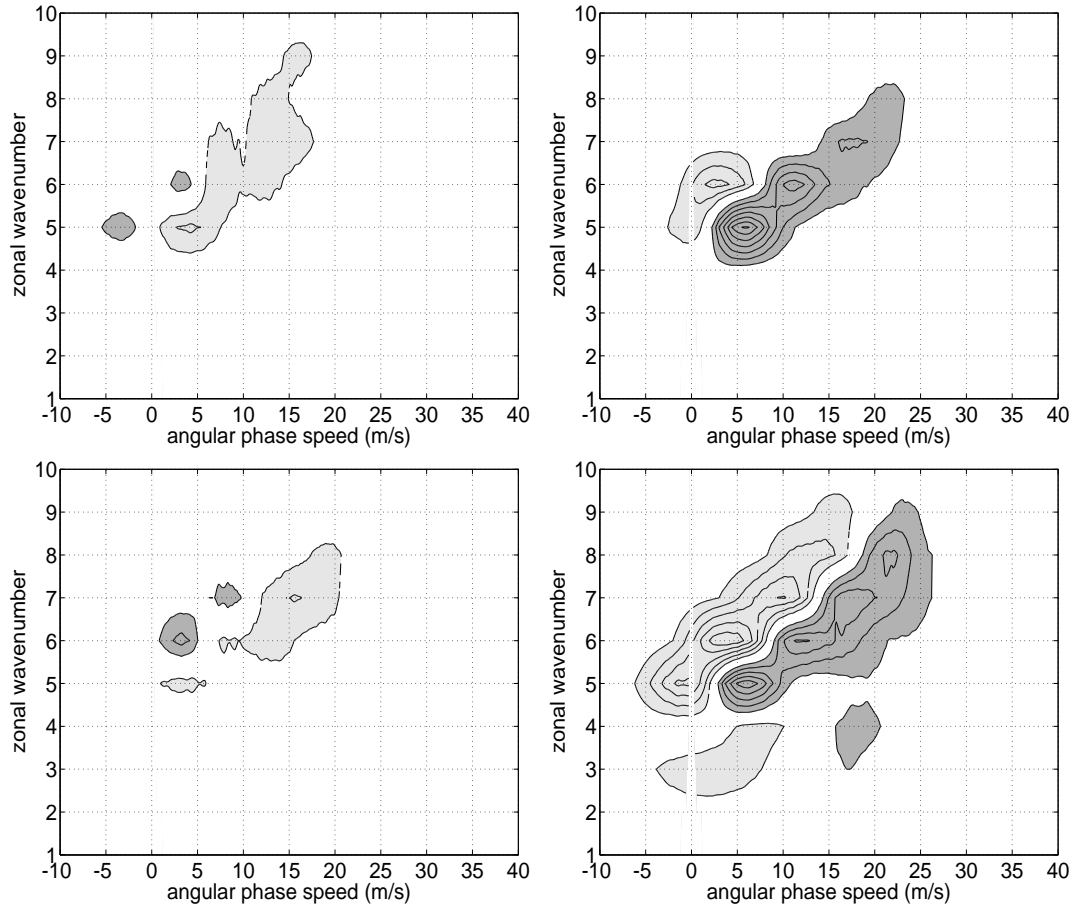


Figure 3.8: The responses in the zonal wavenumber-phase speed spectra of the (top) upper level ($\sigma = 0.230$) eddy momentum flux and (bottom) lower level ($\sigma = 0.843$) eddy heat flux, for the same surface torques on the jet's (left) equatorward flank and (right) poleward flank as in Fig. 3.5. The momentum flux is averaged between 35° and 45° , and the heat flux is averaged between 45° and 55° , with a cosine weighting in latitude. The contour intervals are $0.007 \text{ m}^2/\text{s}^2$ for the momentum flux and 0.01 Km/s for the heat flux. The dark (light) shading denotes the positive (negative) value.

with enhanced cyclonic shear in the initial condition, waves break on the cyclonic side of the jet, and the jet is displaced slightly equatorward. The relationship between the type of life cycles and the jet latitude is also found in the longtime integrations of an idealized dry GCM by Akahori and Yoden (1997). Therefore, the decreased anticyclonic shear equatorward of the jet by a subtropical torque can shift the jet equatorward.

Hartmann and Zuercher (1998) gradually increase the barotropic shear and find that the transition from LC1 to LC2 is abrupt at a critical value of the strength of the added shear. However, in the full model, the jet movement is very linear to the amplitude of the torque. Orlanski (2003), in contrast, finds that a transition from LC1 to LC2 can be obtained in a shallow water model by increasing the amplitude of the forcing. But this cannot explain the poleward jet shift as the surface friction is reduced in a model, in which the eddies are suppressed by barotropic governor (see chapter 2). One can attribute these deficiencies to the shortcomings of a single eddy life cycle. It has also been pointed out by Akahori and Yoden (1997) that there are some differences in the life cycles between the initial value approach and the longtime integrations, such as the relative location between the zonal mean jet and the latitude of maximum eddy kinetic energy.

In chapter 2, we describe a nonlinear shallow model forced by stochastic stirrings, in which the time mean jet is maintained by a balance between the stochastic forcings and radiative relaxation. It is shown quantitatively that changes in the eastward propagation of eddies alone can lead to a shift in the subtropical wave breaking accompanied by the movement in the eddy-driven flow. This can be related to that the meridional scale of eddies does not change very much in the shallow water model, and this may also be the case for the full model, in which the zonal wavenumber changes are small.

As the torque is moved from near the surface into the tropospheric interior, it

requires additional zonal momentum exchange in the vertical. Figure 3.9 shows the EP flux divergence difference for the zonal torques in the tropospheric interior ($\sigma_0 = 0.45$) and near the surface ($\sigma_0 = 0.85$). The anomalous westerly torque in the interior is roughly balanced by anomalous EP flux convergence, which corresponds to the increased divergence near the surface due to anomalous easterly torque. As the result of this cancellation, the imposed angular momentum is brought downwards to the surface by eddies without altering the zonal mean circulation, and therefore the zonal wind response depends relatively little on the forcing level in the troposphere (Fig. 3.3).

The small dependence on the forcing level contradicts the intuition that anomalous zonal torques would alter the vertical zonal wind shears and Eady growth rate in the troposphere. It is the vertical momentum redistribution by the eddies that balances the external forcing and retains an equivalent barotropic structure in the tropospheric response. This vertical momentum redistribution is also achievable by the residual meridional circulations. The induced residual circulations would increase the meridional temperature gradients below the forcing level through diabatic heating/cooling, resulting in more baroclinic zonal wind changes.

3.5 Response to the stratospheric forcing

We further study the stratospheric influence on the troposphere mainly by comparing two experiments, in which the zonal torques in the lower stratosphere ($\sigma_0 = 0.056$) are placed in the subtropics ($\phi_0 = 30$) and high latitudes ($\phi_0 = 70$). Figure 3.10 shows the time and zonally averaged responses in the zonal wind and EP flux divergence. The westerly torque leads to a zonal wind increase that penetrates downwards into the troposphere. This downward penetration displays a poleward slope for the subtropical torque, an equatorward slope for the high latitude torque, and less tilting for the

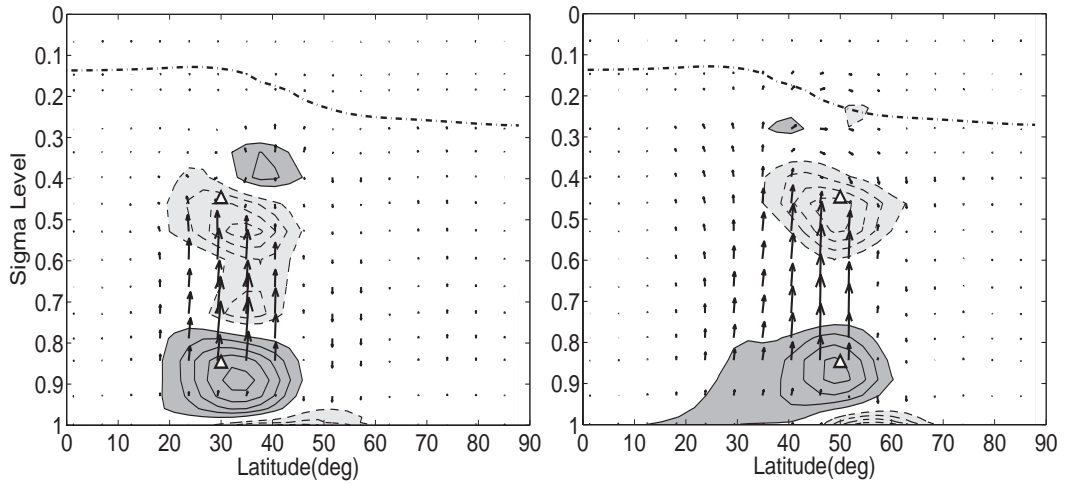


Figure 3.9: The EP flux divergence difference for the zonal torques in the tropospheric interior ($\sigma_0 = 0.45$) and near the surface ($\sigma_0 = 0.85$), that are placed on the jet's (left) equatorward flank and (right) poleward flank. The triangular symbols denote an anomalous westerly torque in the interior and an anomalous easterly torque near the surface. The contour intervals are 0.5 m/s/day for the EP flux divergence, and 4 m/s/day $\cdot(\Delta\sigma, \Delta\phi)$ for the EP vectors. Note that the vertical scale is linear in the plots.

midlatitude torques. The different slopes suggest that the annular mode pattern in the stratosphere is not very meaningful as an internal mode. The torque also increases the eddy activity in the stratosphere. The appearance of anomalous EP flux convergence in the stratosphere corresponds to the increased EP flux divergence near the tropopause between the latitudes 45° and 55° , and the direction of anomalous wave propagation coincides with the slope of the zonal wind change. Despite the difference in the stratospheric changes, the tropospheric jet shifts poleward in both cases, and projects strongly onto the tropospheric internal annular mode. The westerly wind anomalies are again seen in the subtropical upper troposphere due to the poleward jet shift.

However, the response to a stratospheric forcing can not simply be thought of as a zonally symmetric balance with surface friction plus tropospheric eddy feedbacks. This can be easily seen in the zonal wind responses for the lower stratospheric torques

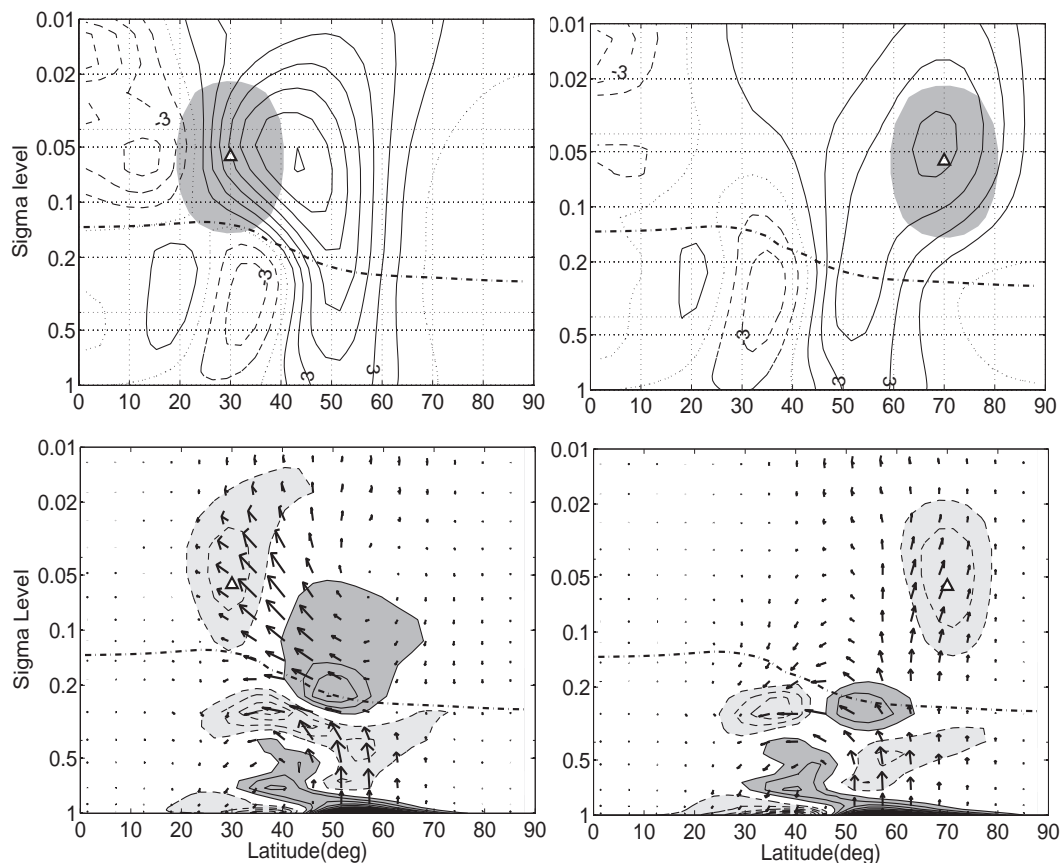


Figure 3.10: The time and zonally averaged responses in the (top) zonal wind and (bottom) EP flux divergence, for the zonal torques in the lower stratosphere ($\sigma_0 = 0.056$) that are placed in the (left) subtropics ($\phi_0 = 30$) and (right) high latitudes ($\phi_0 = 70$). The triangular symbol denotes the forcing center, and the shading in the top panels denotes the region where the torque is greater than 0.5 m/s/day. The contour intervals are 1.5 m/s for the zonal wind, 0.5 m/s/day for the EP flux divergence, and 4 m/s/day $\cdot(\Delta\sigma, \Delta\phi)$ for the EP vectors.

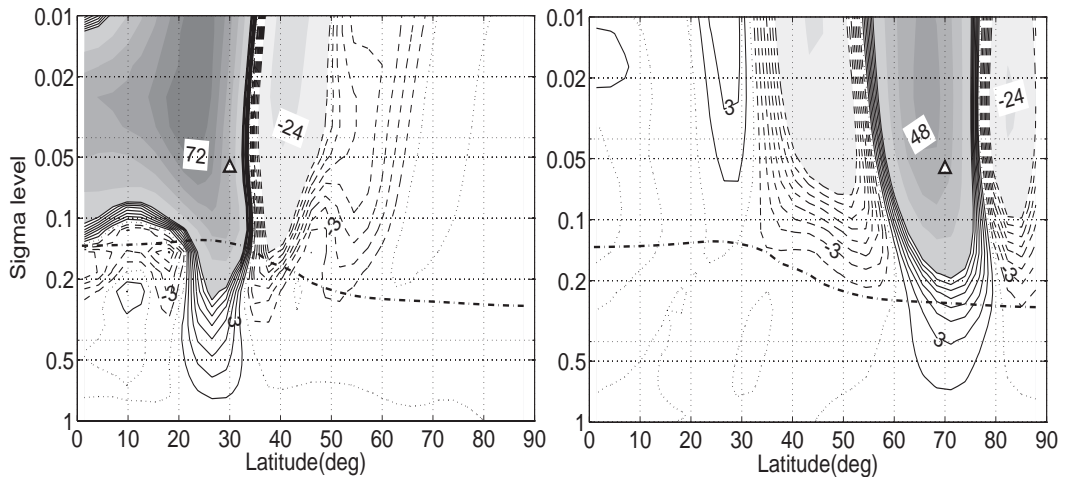


Figure 3.11: The zonal wind responses in the zonally symmetric model for the same lower stratospheric torques in the (left) subtropics and (right) high latitudes as in Fig. 3.10. The triangular symbol denotes the forcing center. The dashdotted lines in the plots are the tropopause level in the control simulation. The zonal wind changes are denoted by the shading with an interval 12 m/s, and by the contours with an interval 1.5 m/s for the values less than 12 m/s.

in the zonally symmetric model in Fig. 3.11. The zonal wind changes are a factor of 8 stronger than those in the full model, and the downward penetrations of zonal winds are vertical. Moreover, the subtropical torque results in a downward penetration, which, in the presence of tropospheric eddy feedbacks, would lead to a jet shift in the opposite direction to that in the full model. These results suggest that the stratospheric eddies are important not only for the magnitude of the stratospheric response, but also for the direction of the tropospheric jet shift.

We extract the effects of stratospheric eddies, by removing the projections of the model responses on the internal annular mode with the least square regression in Eq. (3.4). Figure 3.12 shows the residual patterns in the zonal wind and EP flux divergence, in comparison with the responses in the EP flux divergence due to the planetary waves ($m \leq 3$). The residual wave activity displays a pattern in which anomalous waves originate from the surface, propagate vertically across the tropopause, and converge into the regions of the stratospheric westerly torque. (Note

that such a clear separation can be obtained only if the imposed torque is separate from the tropospheric annular mode.) A comparison with the planetary wave response shows that the residual wave activity is primarily due to planetary waves for the subpolar forcing, but is dominated by medium-scale waves for the subtropical forcing.

The net effect of the prescribed forcing and residual wave activity is to increase the zonal winds mostly in the stratosphere. As the tropospheric eddies enter the stratosphere through the midlatitude tropopause, the subsequent meridional propagation transfers positive zonal wind anomalies from the forcing latitude to midlatitudes in the stratosphere. While the residual wave activities include some tropospheric eddies, more experiments with the zonally symmetric model confirm that the stratospheric eddies alone can generate similar zonal wind changes in the stratosphere (not shown), as is also seen in Kushner and Polvani (2004).

Despite the increased upward EP flux across the tropopause, we argue that the increased lower stratospheric wind is the key for the tropospheric jet shift. The lower stratospheric wind shears can alter the baroclinic eddy life cycle in the troposphere (Wittman et al., 2007). As stratospheric signals are transmitted downwards by planetary waves mainly through the midlatitude tropopause on the poleward flank of the tropospheric jet (Fig. 3.10), it seems plausible to argue that the stratospheric westerly torque can accelerate the phase speed of tropospheric eddies. The only exception is the torque in low latitudes far away from stratospheric eddies (e.g. $\phi_0 = 20^\circ$, $\sigma_0 = 0.056$). We have justified the phase speed increase in the latitude-phase speed spectra and wavenumber-phase speed spectra of the upper level eddy momentum flux and lower level eddy heat flux (Figs. 3.13 and 3.14). The eddy phase speed spectra are remarkably similar to the response to a tropospheric torque on the poleward flank of the jet. The phase speeds of tropospheric midlatitude eddies show consistent increases in momentum and heat fluxes, resulting in the poleward displacement in the subtropical critical latitudes. As such, the lower stratospheric wind anomalies are projected onto

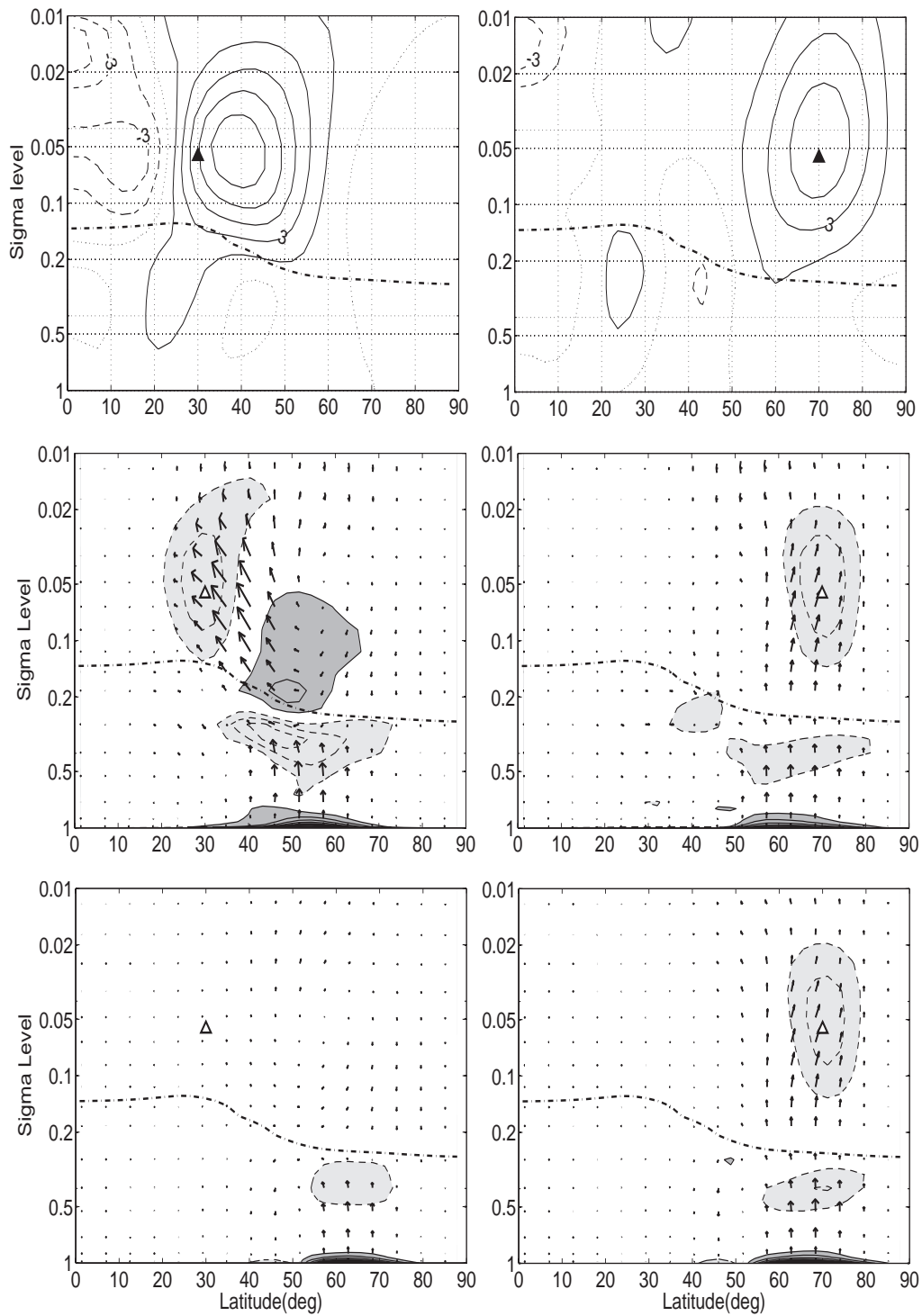


Figure 3.12: The residual patterns, by removing the annular mode projection, in the (top) zonal wind and (middle) EP flux divergence, in comparison with (bottom) the responses in the EP flux divergence due to the planetary waves ($m \leq 3$), for the same lower stratospheric torques in the (left) subtropics and (right) high latitudes as in Fig. 3.10. The contour intervals are 1.5 m/s for the zonal wind, and 0.5 m/s/day for the EP flux divergence, $4 \text{ m/s/day} \cdot (\Delta\sigma, \Delta\phi)$ for the EP vectors.

the tropospheric annular mode.

As the torque is moved aloft in the stratosphere, the residual meridional circulations become more important. Figure 3.15 shows the time and zonally averaged responses in the zonal wind, EP flux divergence and the Coriolis deceleration of the meridional residual circulation, for the zonal torque in the subtropical middle stratosphere ($\phi_0 = 30, \sigma_0 = 0.01$). In contrast to the lower stratospheric torque in Fig. 3.10, the middle stratospheric torque is mainly balanced at the center by the Coriolis deceleration due to anomalous equatorward residual circulation, and results in very intense zonal winds at the forcing center. Moreover, there exists anomalous equatorward wave propagation at the forcing level that attempts to reduce the meridional shears of zonal winds, which might be related to barotropic instability in the stratosphere. Despite these differences, the downward penetration of zonal wind displays a similar poleward slope that coincides with anomalous upward wave propagation from the midlatitude tropopause into the torque region, suggesting that the stratospheric eddies still control the direction of the tropospheric jet shift, rather than the strong residual circulations. These stratospheric eddies transfer positive zonal wind anomalies down to the tropopause level on the poleward flank of the jet, and project onto the positive phase of the tropospheric annular mode.

3.6 The jet response to the orographic GWD parameterization

In this section, we discuss the implications of our results for the orographic GWD parameterization, using GFDL climate model AM2.1. AM2.1 is a global atmosphere and land model forced by the observed values of radiative forcing agents, sea surface temperatures and sea ice (Anderson and coauthors, 2004), and is integrated from January 1983 to December 1998 for this study. The model uses the GWD parameter-

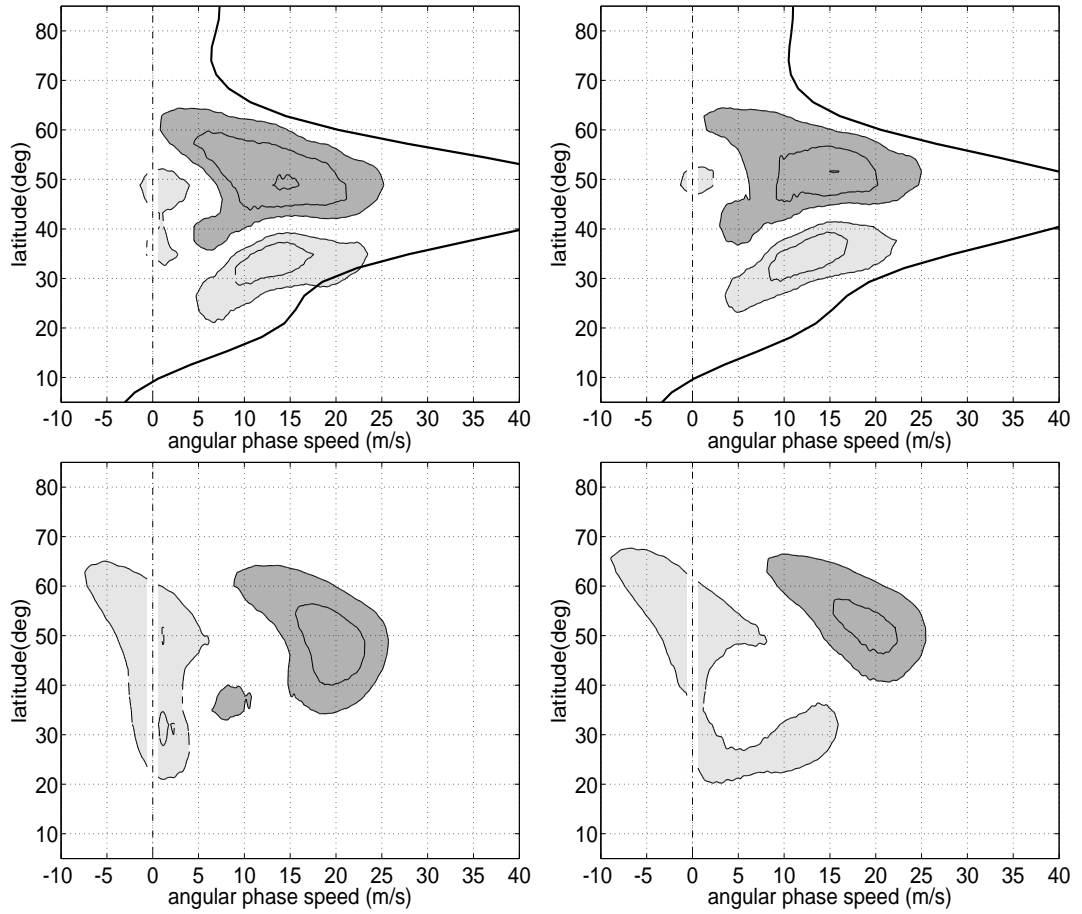


Figure 3.13: The responses in the latitude-phase speed spectra of the (top) upper level ($\sigma = 0.230$) eddy momentum flux convergence and (bottom) lower level ($\sigma = 0.843$) eddy heat flux, for the same lower stratospheric torques in the (left) subtropics and (right) high latitudes as in Fig. 3.10. The thick solid lines in the top panels are the time and zonally averaged upper level ($\sigma = 0.230$) zonal winds, divided by $\cos\phi$ for comparison. The contour intervals are 0.015 m/s/day for the momentum flux convergence and 0.04 Km/s for the heat flux. The dark (light) shading denotes the positive (negative) value.

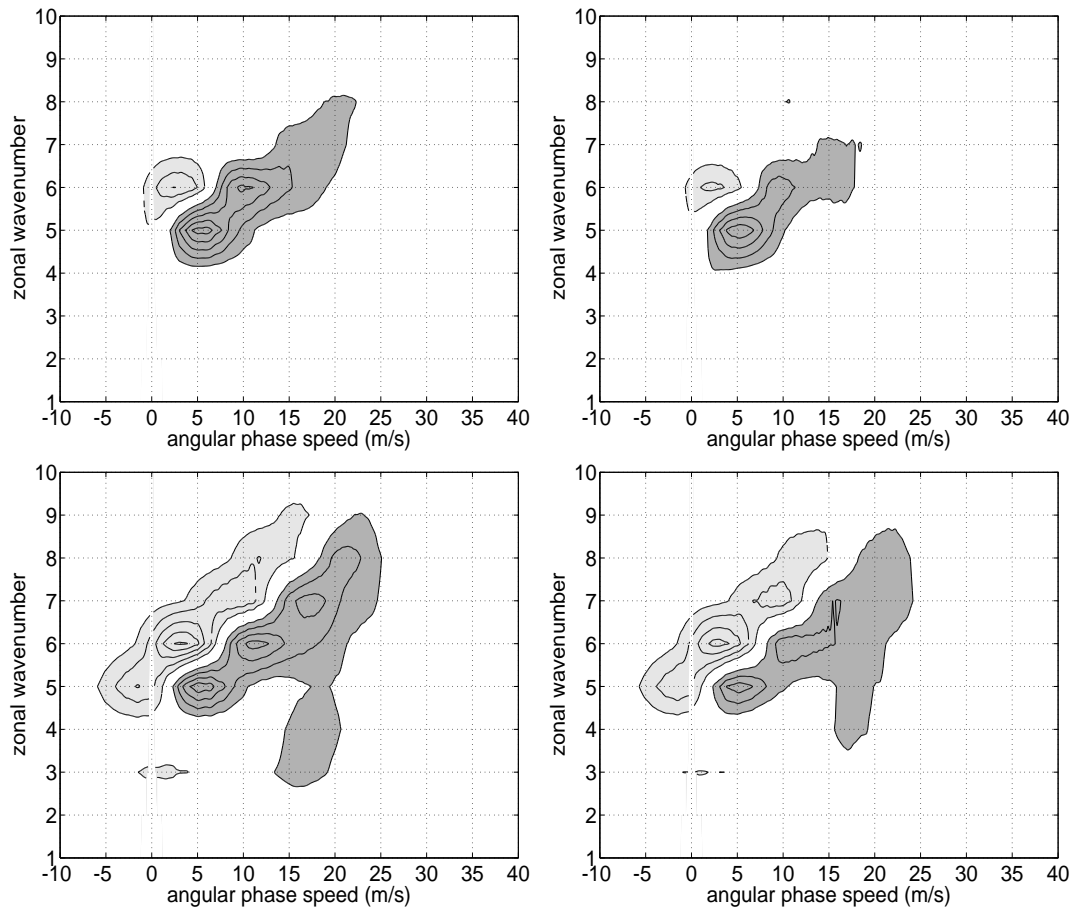


Figure 3.14: The responses in the zonal wavenumber-phase speed spectra of the (top) upper level ($\sigma = 0.230$) eddy momentum flux and (bottom) lower level ($\sigma = 0.843$) eddy heat flux, for the same lower stratospheric torques in the (left) subtropics and (right) high latitudes as in Fig. 3.10. The momentum flux is averaged between 35° and 45° , and the heat flux is averaged between 45° and 55° , with a cosine weighting in latitude. The contour intervals are $0.007 \text{ m}^2/\text{s}^2$ for the momentum flux and 0.01 Km/s for the heat flux. The dark (light) shading denotes the positive (negative) value.

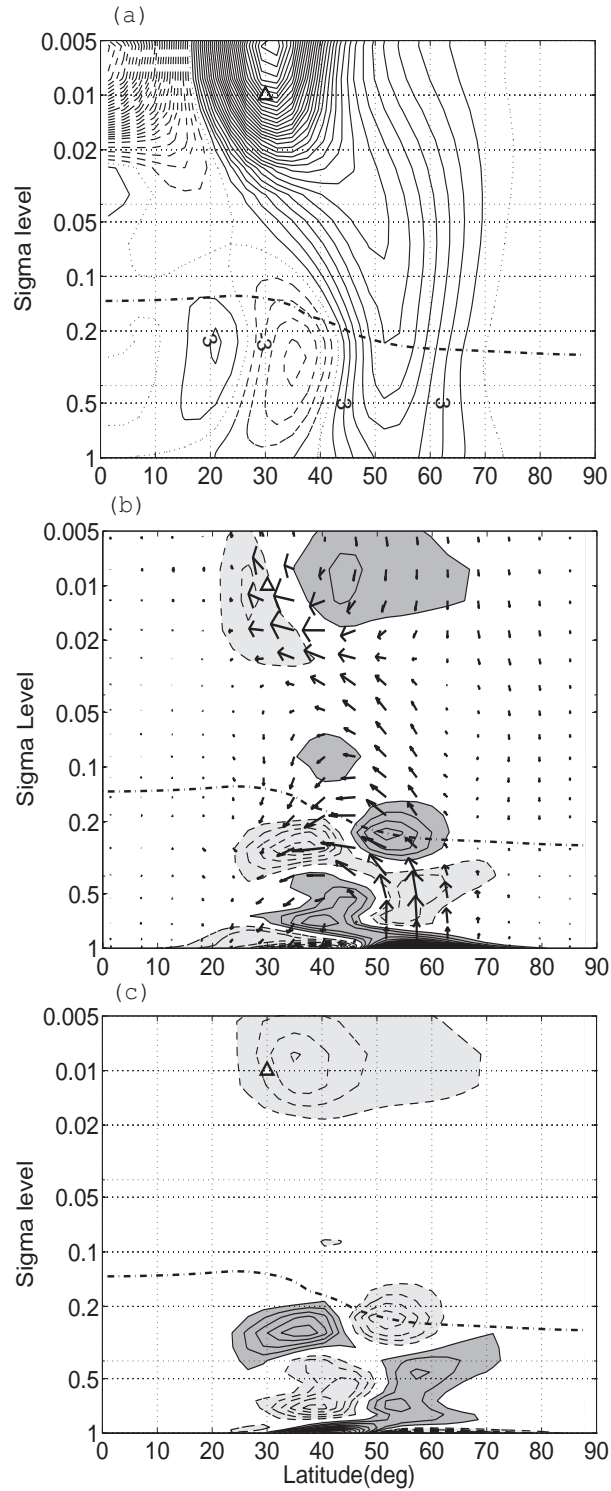


Figure 3.15: The time and zonally averaged responses in (a) the zonal wind, (b) EP flux divergence and (c) the Coriolis deceleration of the meridional residual circulation, for the zonal torque in the subtropical middle stratosphere ($\phi_0 = 30^\circ$, $\sigma_0 = 0.01$). The triangular symbol denotes the forcing center. The contour intervals are 1.5 m/s for the zonal wind, 0.5 m/s/day for the EP flux divergence and the Coriolis deceleration, and 4 m/s/day $\cdot(\Delta\sigma, \Delta\phi)$ for the EP vectors.

ization described in Stern and Pierrehumbert (1988), in which the GWD is deposited at the level where the momentum flux transferred from below exceeds the saturation flux. The surface momentum flux τ_s is parameterized as,

$$\tau_s \propto U^3 G^* \frac{F^2}{F^2 + a^2} \quad (3.5)$$

Where U is the surface wind, F is the Froude number which is a function of surface orography, G^* and a are two non-dimensional constants. G^* is the parameter varied in our sensitivity study.

Figure 3.16 shows the 16-year wintertime (DJF) and zonal mean zonal wind in the control experiment in which $G^* = 1.0$, and the zonal wind response as G^* is reduced from 1.5 to 0.5. We also show the regression of the zonal wind anomaly onto the standardized Northern Hemisphere Annular Mode index, defined as the first principal component of the monthly DJF sea level pressure field poleward of 20°N , in the control experiment. Despite the amplitude difference, the regression pattern simulated in the model resembles the annular mode structure in observations (Thompson and Wallace, 2000). The GWD in the model is mainly deposited above the subtropical jet core in the lower stratosphere. The decreased GWD leads to an increase in the zonal wind, which penetrates downwards and polewards, and projects onto the internal annular mode only in the troposphere. Although the stratospheric polar jet may play a role in this downward influence, the zonal wind change is similar to the response to the subtropical stratospheric torque in the idealized model (Fig. 3.10). Moreover, the downward and equatorward penetration in the zonal wind to a high-latitude stratospheric torque in this idealized model, is also seen in SR and in the observed zonal wind change associated with anomalous stratospheric wave drag (e.g. Black, 2002; Thompson et al., 2006). These results suggest that our understandings from this idealized model are also relevant to the tropospheric jet shift in response to

the stratospheric forcing, even if a stratospheric polar jet exists.

The tropospheric jet sensitivity in Fig. 3.3 implies that the level of gravity wave breaking may have a considerable impact on the tropospheric jet latitude. First, if some of the GWD were deposited below the tropopause level, the tropospheric jet would shift poleward, with little dependence on the drag profile in the troposphere, consistent with Stephenson (1994). On the other hand, if the gravity wave breaking were to occur at a higher level in the stratosphere, the decreased air density would result in a greater zonal wind deceleration so as to satisfy angular momentum conservation, and therefore we should anticipate a more dramatic jet shift (associated with the increased forcing amplitude) than seen in Fig. 3.3.

We have also looked at the spatial distribution in the tropospheric response. Figure 3.17 shows the 10 meter surface wind response to the reduced GWD, and the regression of the surface wind anomaly onto the annular mode index in the control experiment. Although the GWD in the lower stratosphere is localized over steep topography, the surface wind response displays a zonally symmetric component, in that the surface westerlies are displaced poleward in both the Atlantic and Pacific oceans. This surface wind response is very similar to the internal annular mode pattern, justifying that our understandings from a model with zonally symmetric lower boundary conditions are relevant to GCMs with more complex boundary conditions.

3.7 Conclusions and discussions

We study the tropospheric response to prescribed zonal forcing in an idealized dry model. The tropospheric jet shifts equatorward for a westerly (eastward) zonal torque on the equatorward flank of the jet in the troposphere. In contrast, the tropospheric jet moves poleward for a torque on the poleward flank of the jet in the troposphere, and for a torque in the extratropical stratosphere. These jet movements project

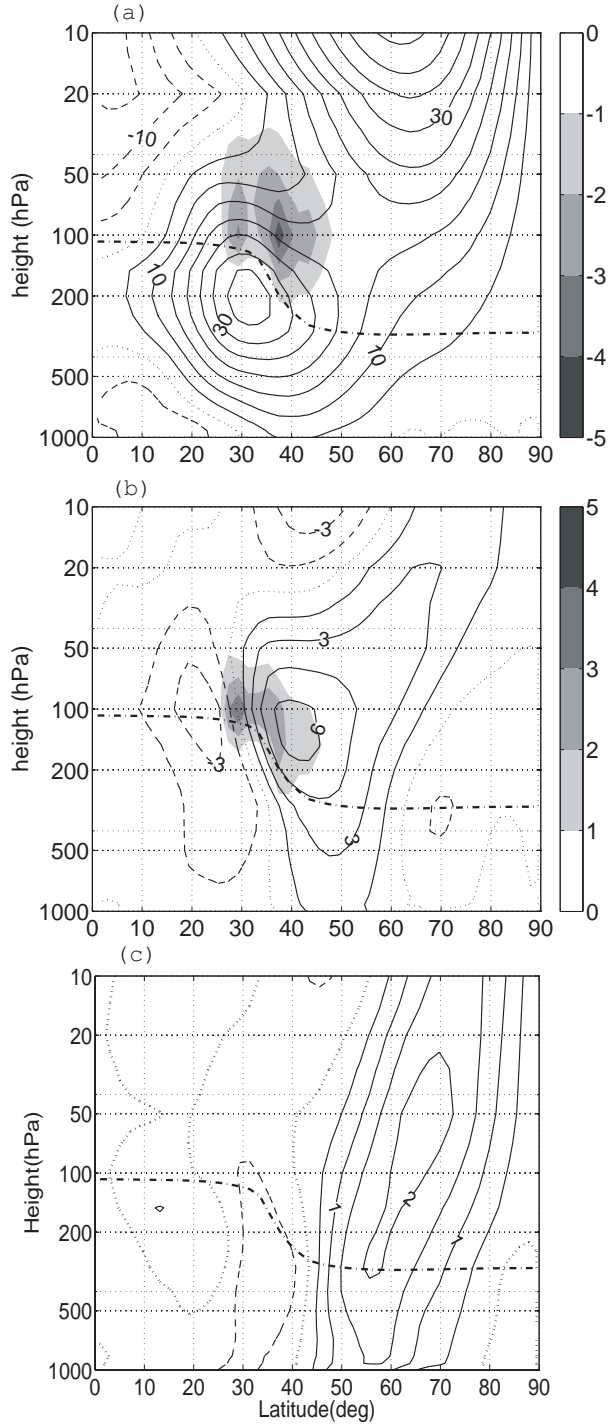


Figure 3.16: The 16-year wintertime (DJF) and zonally averaged (a) zonal wind in the control experiment in which $G^* = 1.0$, (b) the zonal wind response as G^* is reduced from 1.5 to 0.5, and (c) the regression of the zonal wind anomaly onto the standardized Northern Hemisphere Annular Mode index in the control experiment, in the GFDL AM2.1. G^* is the GWD parameter, and a larger value denotes more zonal wind deceleration. The shading in (a) and (b) denotes the zonal wind acceleration by GWD, with an interval of 1 m/s/day. The contour intervals are 5 m/s for (a), 1.5 m/s for (b), and 0.5 m/s for (c).

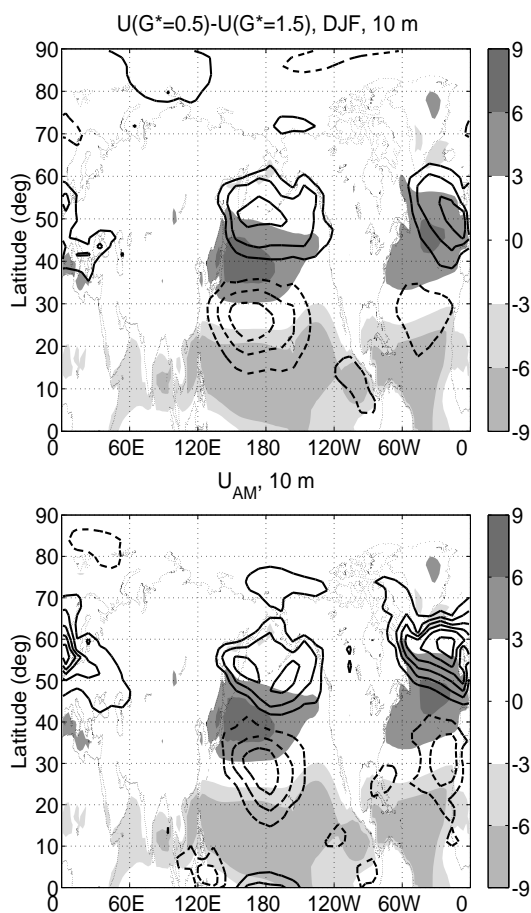


Figure 3.17: The 16-year wintertime (DJF) mean (top) 10 meter surface wind response as G^* is reduced from 1.5 to 0.5, and (bottom) the regression of the surface wind anomaly onto the standardized Northern Hemisphere Annular Mode index in the control experiment. The shading represents the surface winds in the control experiment in which $G^* = 1.0$. The shading interval is 3 m/s, and the contour intervals are 0.8 m/s for the wind response, 0.4 m/s for the regression pattern.

strongly onto the internal annular mode in the troposphere.

These jet movements can be explained by changes in the critical latitudes of tropospheric eddies. For a westerly torque near the surface, the response can be thought of a zonally symmetric balance between the torque and surface friction at first (with surface winds modified until the increased surface friction balances the torque). The zonally symmetric response in the zonal wind is nearly barotropic above the forcing. While the increased zonal winds in the subtropics allow the midlatitude eddies to propagate further into the tropics and result in the equatorward shift in the critical latitudes, the increased winds in the midlatitudes accelerate the eastward eddy phase speeds and lead to the poleward shift in the critical latitudes. Furthermore, as the torque is moved into the tropospheric interior, the eddy activities are redistributed in the vertical, so as to retain an equivalent barotropic structure in the zonal wind.

As for the torque in the stratosphere, the stratospheric eddies play a more important role in controlling the tropospheric jet latitude than do the residual circulations. Despite the lack of the stratospheric polar jet in this idealized model, the tropospheric response to the prescribed stratospheric forcing is similar to that in models with a more realistic stratosphere. The downward penetration of zonal winds to the troposphere displays a poleward slope for the subtropical torque, an equatorward slope for the high latitude torque, and less tilting for the midlatitude torques. These slopes are the signatures of anomalous wave propagation in the stratosphere, in contrast to the vertical downward penetration accompanying the residual circulation changes in the "downward control" theory (Haynes et al., 1991). As the tropospheric eddies enter the stratosphere through the midlatitude tropopause, they transfer positive zonal wind anomalies from the torque region to the midlatitude lower stratosphere. These wind anomalies are thought to be able to modify the eddy phase speeds in the upper troposphere, and displace the tropospheric jet as seen for a tropospheric forcing. However, further research is necessary to examine how the stratospheric planetary-scale

eddies interact at the tropopause level with the tropospheric medium-scale eddies. Such interactions are also observed, although not fully understood, in the life cycle of sudden stratospheric warming (e.g. Limpasuvan et al., 2004).

3.8 Appendix A: The Eliassen-Palm (EP) fluxes

Here we briefly summarize the Transformed Eulerian Mean (TEM) forms of zonally averaged equations in the spherical and pressure coordinates (Andrews et al., 1987; Edmon et al., 1980; Vallis, 2006). In the absence of diabatic heating or frictional damping, the zonal mean zonal momentum, thermodynamics and mass continuity equations can be written as

$$\frac{\partial \bar{u}}{\partial t} - \bar{v}_*(f + \bar{\zeta}) + \bar{\omega}_* \frac{\partial \bar{u}}{\partial p} = dF \quad (3.6)$$

$$\frac{\partial \bar{\theta}}{\partial t} + \frac{\bar{v}_*}{a} \frac{\partial \bar{\theta}}{\partial \phi} + \bar{\omega}_* \frac{\partial \bar{\theta}}{\partial p} = 0 \quad (3.7)$$

$$\frac{1}{a \cos \phi} \frac{\partial(\bar{v}_* \cos \phi)}{\partial \phi} + \frac{\partial \bar{\omega}_*}{\partial p} = 0 \quad (3.8)$$

Where the overbars denote zonal means, and primes denote the deviations from zonal means (eddies). a is the Earth radius, ϕ is latitude, p is pressure, θ is the potential temperature, $f = 2\Omega \sin \phi$ and ζ are the planetary vorticity and relative vorticity, (u, v, ω) are the zonal, meridional and vertical velocities. In particular, $\partial \bar{\theta} / \partial p$ is the static stability parameter, dF is the Eliassen-Palm (EP) flux divergence and represents the zonal wind acceleration due to eddy activities, and (v_*, ω_*) are residual circulations induced by diabatic heating or dissipation.

The residual circulations, (v_*, ω_*) , are defined as,

$$\bar{v}_* = \bar{v} - \frac{\partial}{\partial p} \left(\frac{\overline{v'\theta'}}{\partial \bar{\theta} / \partial p} \right) \quad (3.9)$$

$$\bar{\omega}_* = \bar{\omega} + \frac{1}{a \cos \phi} \frac{\partial}{\partial \phi} \left(\frac{\overline{v'\theta'}}{\partial \bar{\theta} / \partial p} \cos \phi \right) \quad (3.10)$$

The EP flux divergence, $dF = dF_\phi + dF_p$, consists of the meridional and vertical components.

$$dF_\phi = \frac{1}{a \cos^2 \phi} \frac{\partial}{\partial \phi} (\cos^2 \phi (-\overline{v'u'} + \frac{\partial \bar{u}}{\partial p} (\frac{\overline{v'\theta'}}{\partial \bar{\theta}/\partial p}))) \quad (3.11)$$

$$dF_p = \frac{\partial}{\partial p} (-\overline{\omega'u'} + (f + \bar{\zeta}) \frac{\overline{v'\theta'}}{\partial \bar{\theta}/\partial p}) \quad (3.12)$$

In the quasi-geostrophic approximation, the EP flux divergence becomes

$$dF_\phi = \frac{1}{a \cos^2 \phi} \frac{\partial}{\partial \phi} (-\overline{v'u'} \cos^2 \phi) \quad (3.13)$$

$$dF_p = \frac{\partial}{\partial p} (f \frac{\overline{v'\theta'}}{\partial \bar{\theta}/\partial p}) \quad (3.14)$$

The EP flux divergence is equal to quasi-geostrophic potential vorticity (q) flux.

$$dF = \overline{v'q'} \quad (3.15)$$

Under the WKB approximation, the EP flux is equal to the wave activity multiplied by the group velocity, and therefore, the EP flux vectors plotted in the figures represent the direction of wave propagation.

3.9 Appendix B: The Empirical Orthogonal Function (EOF) analysis

Suppose we have measurements of some variable at locations x_1, x_2, \dots, x_m , taken at times t_1, t_2, \dots, t_n . For each time t_j , ($j = 1, \dots, n$), we can think of the measurements x_i , ($i = 1, \dots, m$) as a map. We store the data in a two-dimensional data set $\mathbf{X}(n \times m)$, whose n rows represent the n observation times (sampling dimension) and m columns represent the m components (structure dimension) of the state vector X_m .

We perform a singular vector decomposition (SVD).

$$\mathbf{X} = \mathbf{U}\Sigma\mathbf{V}^T, \quad \Sigma_{i,j} = \delta_{i,j}\gamma_{i,i} \quad (3.16)$$

where \mathbf{U} and \mathbf{V} are orthogonal and Σ is diagonal. The covariance matrix \mathbf{R} is

$$\mathbf{R} = \mathbf{X}^T\mathbf{X} = \mathbf{V}\Sigma^T\Sigma\mathbf{V}^T \quad (3.17)$$

$\mathbf{V}(m \times m)$ are the Empirical Orthogonal Functions (EOFs) for the covariance matrix \mathbf{R} , and $\mathbf{U}(n \times n)$ are the corresponding Principle Components (PCs). $\gamma_{i,i}$, ($i = 1, \dots, r \leq \min(n, m)$) are the square roots of the nonzero eigenvalues of \mathbf{R} . The percentage of variance explained by the i th EOF is

$$\gamma_i^2 / \sum_{i=1}^r \gamma_i^2 \quad (3.18)$$

In practice, we weight the covariance matrix by the cosine latitude, prior to the SVD, to take into account the decreasing area towards poles. Also, instead of the normalized EOFs, we often present the regressions onto the standardized PCs, and then the regression patterns have the magnitude of the variability.

Chapter 4

Observations and Climate Models

4.1 Introduction

The intraseasonal variability of the extratropical circulations in both hemispheres is characterized by remarkably zonally symmetric or annular patterns. The Southern Hemisphere and Northern Hemisphere annular modes (SAM and NAM), defined by the variability of sea level pressure, are associated with changes of equivalent barotropic structures in tropospheric zonal winds, temperatures and geopotential heights (Thompson and Wallace, 2000). The dipolar structure of annular modes in latitude represents the meridional vacillation of surface westerlies and upper tropospheric eddy-driven jets about their climatological mean positions. This zonal wind variability is generally attributed to the internal variability of the atmosphere that arises from the eddy-mean flow interaction (e.g. Limpasuvan and Hartmann, 2000; Lorenz and Hartmann, 2001, 2003). The zonal flow vacillation is also found in idealized models without topography, seasonal cycle or sea surface temperature variations (e.g. Robinson, 1991; James and James, 1992; Yu and Hartmann, 1993).

On the interannual time scale, the extratropical zonal flow can be affected by the El Niño-Southern Oscillation (ENSO). In addition to the zonally asymmetric

Rossby wave teleconnection pattern (e.g. Hoskins and Karoly, 1981), the extratropical circulation response bears a zonally symmetric component, and projects strongly onto the SAM during austral summer (Robinson, 2002; Seager et al., 2003; L’Heureux and Thompson, 2006). These extratropical changes can be roughly explained by the impact of subtropical zonal wind anomalies on the equatorward propagation and absorption of midlatitude eddies near their critical latitudes, and subsequently on the eddy-driven extratropical circulation (Chang, 1995, 1998; Robinson, 2002; Seager et al., 2003).

Additionally, the observations reveal an annular mode trend toward the positive phase in both hemispheres in recent decades (e.g. Thompson et al., 2000; Thompson and Solomon, 2002). These trends are seen in climate model simulations of the late 20th century and projections of future climate change, and have been attributed to greenhouse gas increases and stratospheric ozone depletion. Models predict a consistent positive trend in the annular modes in both hemispheres due to increases in greenhouse gas concentrations (Fyfe et al., 1999; Kushner et al., 2001; Stone et al., 2001; Cai et al., 2003; Rauthe et al., 2004), as well as a trend in the SAM to decreases in stratospheric ozone concentrations (Kindem and Christiansen, 2001; Sexton, 2001; Gillett and Thompson, 2003). Recent studies suggest that stratospheric ozone depletion is a greater contributor to the observed SAM trend in the late 20th century, and that greenhouse gas increases will sustain and continue the positive annular mode trends in two hemispheres throughout the 21st century despite the predicted recovery of stratospheric ozone concentrations (Shindell and Schmidt, 2004; Arblaster and Meehl, 2006; Miller et al., 2006).

In this chapter, we identify and compare the changes in eddy characteristics associated with these annular patterns of climate variability to interpret the mechanisms that generate such modal variations on various time scales. We look at these annular variations from the perspective of angular momentum balance, and examine the

latitudinal variation of surface westerlies rather than the phase of a fixed annular mode. In the monthly and zonal average, the surface stress, generally quadratic to surface winds, is equal to the vertical integral of momentum flux convergence minus the mountain drag and gravity wave drag. Our main concern is to show consistent variations in the eddy momentum flux convergence and surface winds, and interpret their variations by the unforced or forced variability in the large-scale wave propagation that generates these momentum fluxes.

We examine the space-time spectra of eddy momentum fluxes in the reanalysis and the outputs of climate models. On the interannual time scale, we find that the ENSO-induced eddy variability is consistent with the impact of subtropical wind anomalies onto the refractive index for the large-scale wave propagation suggested in Seager et al. (2003). As to the long-term trends, the extratropical transient eddies are marked by an trend to increased eddy phase speeds in the Southern Hemisphere in the late 20th century, and in the projections for future climate change in both hemispheres. This trend is very similar to the internal interannual variability in the eddy spectra, suggesting that the annular mode trends due to greenhouse gas increases or stratospheric ozone depletion are more related to the processes for the extratropical internal variability, rather than those for the tropical-extratropical interactions.

In this chapter, we first describe the reanalysis data and climate models used for this study in section 4.2. Then, we describe the variability in the latitude of surface westerlies and eddy spectra on various time scales. In section 4.3, we show the linear trends in the Southern Hemisphere in the late 20th century, in the reanalysis data and in coupled and atmosphere-only climate models. The content of this section appears in Chen and Held (2007). In section 4.4, we first compare the ENSO-induced interannual variability between the ERA-40 reanalysis and the AM2.1 ensemble mean, and then present the internal interannual variability in AM2.1 by removing the ensemble mean SST-forced variability. In section 4.5, we describe the response to global warming in

the GFDL coupled climate model. Finally, we offer a brief summary in section 4.6.

4.2 Reanalysis and models

We use the ERA-40 reanalysis data and comprehensive climate models for this study. ERA-40 is the latest reanalysis from the European Centre for Medium-Range Weather Forecasts (Uppala and coauthors, 2005), covers the period from September 1957 to August 2002 with four observations per day. The data set is on a $2.5^\circ \times 2.5^\circ$ horizontal grid, and has 23 pressure levels in the vertical, with 10 levels above 100 hPa.

We use the GFDL global atmosphere and land model, "AM2.1" (Anderson and coauthors, 2004), and coupled atmosphere-ocean model, "CM2.1" (Delworth and coauthors, 2006). The model outputs consist of an ensemble of experiments for present climate from 1860-2000. The CM2.1 integrations are composed of 5 ensemble members, forced by estimates of the observed changes in well-mixed greenhouse gases, tropospheric and stratospheric ozone, volcanic and anthropogenic aerosols, solar irradiance, and land use. Three of these integrations were submitted to the archive of coupled model results provided for the IPCC (Intergovernmental Panel on Climate Change) organized at PCMDI (Program in Climate Model Diagnosis and Intercomparison). The AM2.1 simulations consist of 10 ensemble members using the same changes in forcing functions, but with sea surface temperatures (SSTs) and sea ice prescribed at observed values. In addition, we have examined one coupled-model projection for the 21st century following the greenhouse gas forcing in IPCC A2 scenario. All the experiments are conducted at the same atmospheric model resolution, with a horizontal grid of 2.5° longitude by 2.0° latitude, and 17 pressure levels in the vertical, with 5 levels above 100 hPa.

4.3 The linear trends in the late 20th century

4.3.1 Reanalysis data

We first look at the linear trends of the eddy spectra in the late 20th century in the ERA-40 reanalysis. Despite less reliability in the early data, Marshall (2003) suggests that ERA-40 provides a reliable representation of the Southern Hemisphere high latitude atmospheric circulation variability. We choose to study a 40-year period from 1961-2000, and focus on the Southern Hemisphere summer (DJFM) when the SAM trend is greatest (Thompson and Solomon (2002); Marshall (2003), and Fig. 4.2 in this section). We first compute the space-time co-spectra of (u, v) for the 120-day DJFM time series in each year, using daily data tapered by a Hanning window. Following Randel and Held (1991), we transform the (frequency, wavenumber) spectra into (angular phase speed, wavenumber) spectra and then sum over wavenumbers, resulting in plots of these spectra as a function of latitude and phase speed. Finally, the least-square best fit linear trends are computed for these phase-speed spectra.

The 40-year climatological mean and trend of the eddy momentum flux convergence at 250 hPa in DJFM are shown as a function of latitude and angular phase speed (Fig. 4.1). The climatological mean of the eddy spectrum displays the familiar eddy momentum flux convergence in midlatitudes and divergence near the critical latitudes, where the phase speed equals the background zonal mean wind. The midlatitude convergence and subtropical divergence are both dominated by eastward propagating disturbances with $U/\cos(\theta)$ between 5 and 20 m/s, with maximum values at 10~15 m/s.

The trend in the phase speed spectrum shows that the phase speed of the eddies transporting momentum increases with time. Most of the convergence trend at 60°S is due to eddies with phase speeds between 15 and 30 m/s, with the largest contribution from phase speeds close to 25 m/s, far above the maximum in the climatological con-

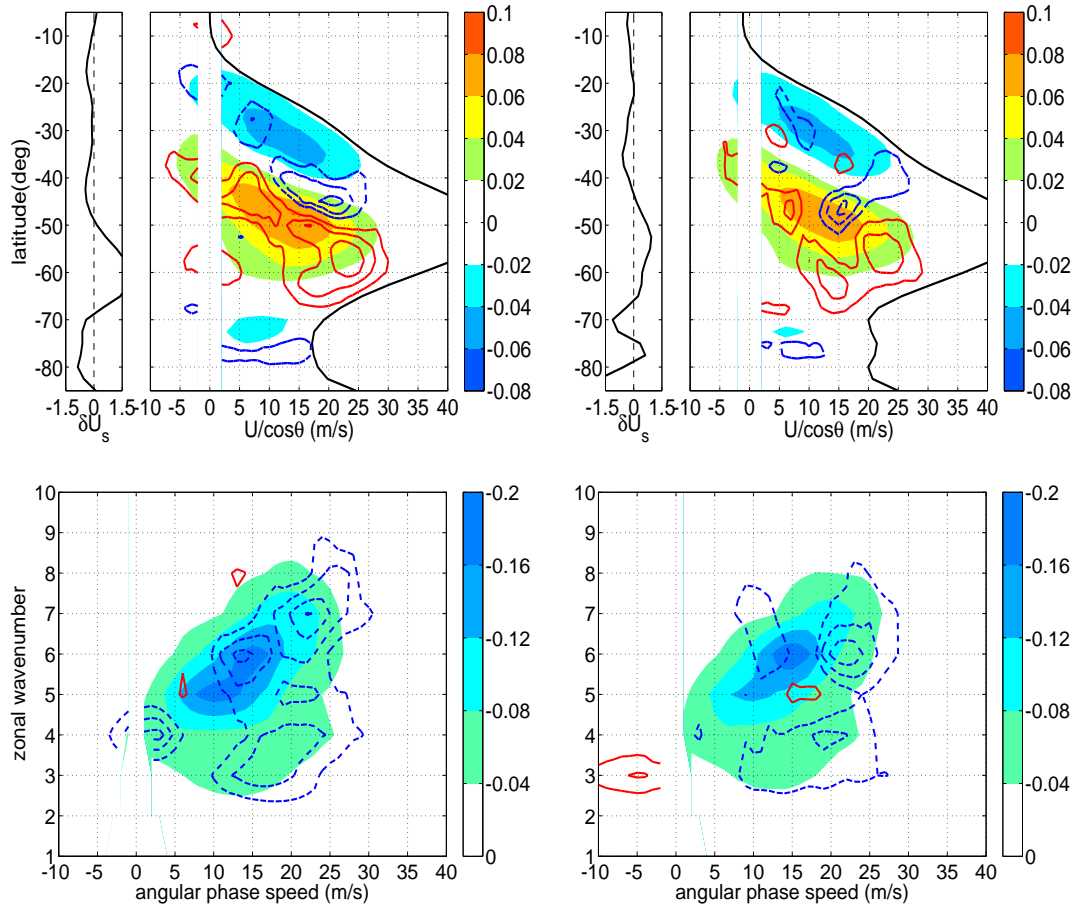


Figure 4.1: The (shading) climatological means and (contours) linear trends of the eddy spectra at 250 hPa in DJFM, for (left) 40 years (1961-2000) in ERA-40 and (right) 28 years (1979-2006) in NCEP/NCAR. The figure denotes the (top) *eddy momentum flux convergence* as a function of latitude and angular phase speed, and (bottom) *eddy momentum flux* as a function of zonal wavenumber and angular phase speed with a cosine weighted average between 55°S and 45°S . In the top panels, the black solid lines denote the time and zonally averaged zonal winds at 250hPa divided by $\cos\theta$, in comparison with the spectra, and the trends of zonally averaged 10 meter surface winds, on the left of the spectra. The contour intervals are (top) $0.01 \text{ m/s/day}/(40 \text{ year})$ and (bottom) $0.025 \text{ m}^2/\text{s}^2/(40 \text{ year})$ for the trends in ERA-40, and the contour intervals are (top) $0.01 \text{ m/s/day}/(28 \text{ year})$ and (bottom) $0.025 \text{ m}^2/\text{s}^2/(28 \text{ year})$ for the trends in NCEP/NCAR. The red (blue) color denotes the positive (negative) value.

vergence pattern. The trend in subtropical divergence is also due to eddies with larger phase speeds than the typical eddies contributing to the subtropical divergence in the mean climate. One can describe the change in the latitude/phase speed spectrum as a shift towards faster eddies accompanied by a poleward shift, roughly following the slope of the subtropical critical latitude.

As the trend is characterized by an increase in the poleward momentum flux across 50°S , we plot the climatological mean and trend of eddy momentum flux as a function of zonal wavenumber and angular phase speed, with a cosine-weighted average between 55°S and 45°S . The climatological mean spectrum shows that the eddies with smaller zonal wavenumbers propagate more rapidly eastwards, as expected from the Rossby wave dispersion relationship, and that the dominant eddies with phase speeds of $10\sim 15$ m/s have the zonal wavenumbers of 5-6. More importantly, the trend shows that the eddy momentum flux increase due to faster eddies with phase speeds of $15\sim 30$ m/s is not associated with a clear change in the eddy scale.

Concerned of the data quality before satellite was incorporated in the global data assimilation system, we have additionally examined the reanalysis product from National Centers for Environmental Prediction - National Center for Atmospheric Research (NCEP/NCAR) (Kalnay and Coauthors, 1996; Kistler and Coauthors, 2001). We compare the 28-year (1979-2006) trend of eddy momentum fluxes in NCEP/NCAR with the 40-year (1961-2000) trend in ERA-40, and the overlapped period covers most of the poleward displacement of surface westerlies in the observation (Fig. 4.3). In comparison with the 40-year trend in ERA-40, the 28-year trend in NCEP/NCAR displays an additional convergence maximum at 60°S and between 10 and 15 m/s, and also a greater projection on the poleward shift than on the strengthening of surface westerlies. But the overall trends in two reanalysis products display a similar pattern that the midlatitude eddies increase in phase speed and displace poleward over time, and the resemblance in zonal wavenumber-phase speed spectra suggests

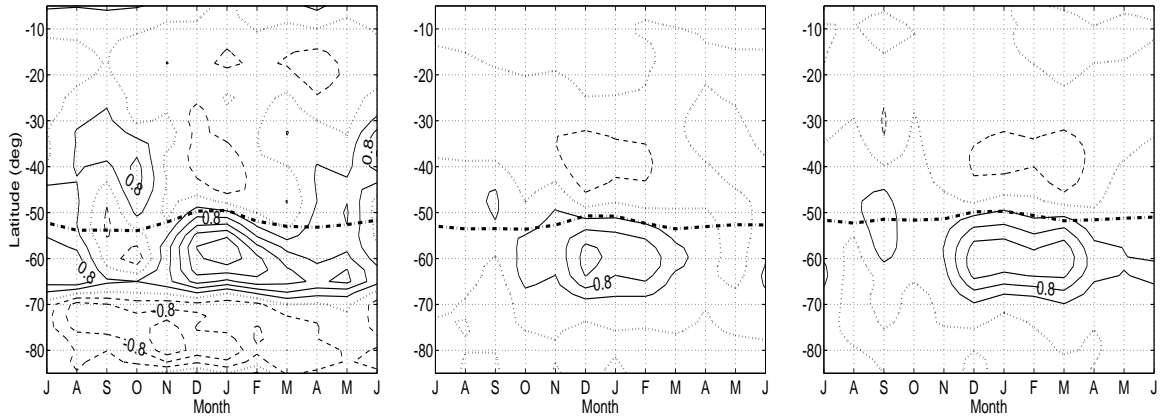


Figure 4.2: The linear trends in the monthly and zonally averaged 10 meter surface winds for (left) ERA-40 and the ensemble means in (middle) AM2.1 and (right) CM2.1. The dotted-dashed lines denote the position of the climatological mean westerly maxima. The contour intervals are $0.4 \text{ m/s}/(40 \text{ year})$.

that the increased eddy phase speed has a small dependence on the eddy scale.

4.3.2 GFDL climate models

We further compare the observations with climate model simulations, to help increase our confidence in the significance of the observed trends. Figure 4.2 shows the linear trends in the monthly and zonally averaged 10 meter surface winds for ERA-40 and for the ensemble means in AM2.1 and CM2.1. While the surface zonal wind change in the models is about a factor of 2 weaker than the observed change, the ensemble means in both AM2.1 and CM2.1 capture the observed wind increase between the latitudes of 50°S - 70°S and decrease between 30°S - 50°S in the months of December-March. As the climatological mean surface westerlies peak at about 50°S , these zonal wind trends are implicative of the poleward shift of surface westerlies.

Figure 4.3 shows the ensemble means and spreads of the latitude of the DJFM and zonal mean 10 meter surface westerly maximum from 1961-2000 in AM2.1 and CM2.1. This latitude is obtained by computing the meridional derivative of the DJFM and zonally averaged zonal wind, and using a cubic interpolation to estimate

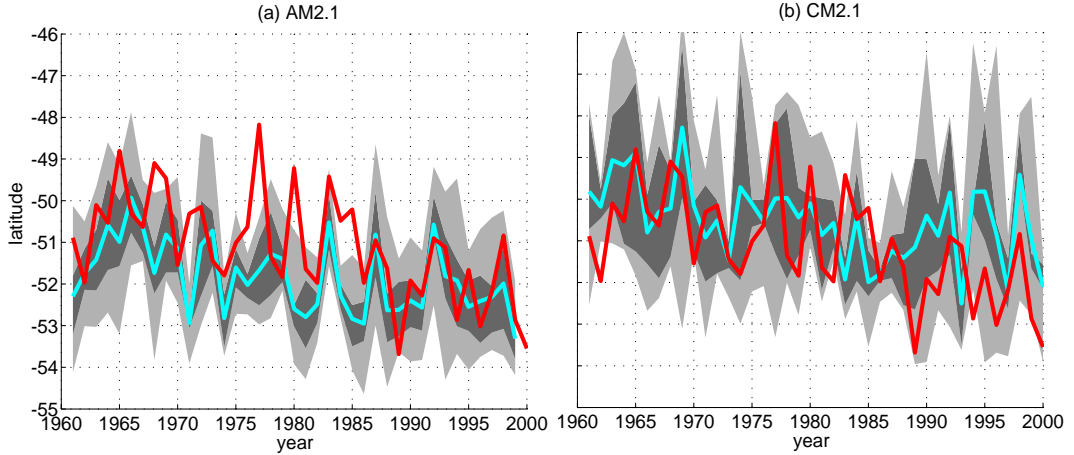


Figure 4.3: The ensemble means and spreads of the latitude of the DJFM and zonal mean 10 meter surface westerly maximum from 1961-2000 in (a) AM2.1 and (b) CM2.1. The red and cyan lines denote the westerly latitudes for ERA-40 and the model ensemble mean, respectively. The westerly latitudes in each year for the ensemble experiments are ranked in an ascending order as y_i ($i = 1, \dots, 10$ for AM2.1 and $i = 1, \dots, 5$ for CM2.1). The shading in AM2.1 is between $(y_1 + y_2)/2$ and $(y_9 + y_{10})/2$, in which the dark shading is between $(y_3 + y_4)/2$ and $(y_7 + y_8)/2$. The shading in CM2.1 is between y_1 and y_5 , in which the dark shading is between y_2 and y_4 .

the location of the zero in the derivative near the grid point of the surface westerly maximum. The ensemble means of the simulated poleward shifts in AM2.1 and CM2.1 are comparable to the observed shift in ERA-40, and their ensemble spreads about the trends encompass the observed fluctuations in most years. While AM2.1 and CM2.1 both show a gradual poleward movement in 40 years, the surface westerly shift in ERA-40 is especially abrupt in the 1980s. This rapid shift in the reanalysis can be attributed to the roughly concurrent development of Antarctic ozone hole, but it may be also related to changes in the available data sources around this period. The ensemble spread in CM2.1 is somewhat larger than that in AM2.1, due to the SST variability in the coupled model.

Figure 4.4 shows the linear trends of DJFM-averaged zonal mean zonal wind, transient eddy momentum flux convergence and zonal mean surface stress for ERA-40, and for the ensemble means of AM2.1 and CM2.1. The transient eddy flux is

obtained by first calculating the total eddy flux from daily data, and then subtracting the stationary component defined by the DJFM mean for each year.

From the upper row of panels, the vertical structure of simulated wind trends resembles the observed pattern in the troposphere and the lower stratosphere. The zonal wind trend in the troposphere displays an equivalent barotropic increase on the poleward side of the midlatitude jet. The increase of zonal wind in the subpolar lower stratosphere is similar in the models and observations. Such an increase is expected from the increased meridional temperature gradients due to stratospheric cooling, but we do not attempt a decomposition into the effects of ozone and greenhouse gases here.

The amplitude of the simulated trends in the winds is smaller than that in the reanalysis, however, in both the troposphere and stratosphere. The ensemble mean trend simulated in AM2.1 is roughly 50% of the ERA-40 trend, while the CM2.1 trend is somewhat larger but still below the reanalysis trend. This difference is also apparent in the eddy momentum flux convergence in the center row of panels, and the surface stress in the bottom row. The ensemble mean stress trend in CM2.1 is roughly a factor of 2 smaller than that in ERA-40, while the mean stress trend in AM2.1 is closer to a factor of 3 too weak. Because the stress is quadratic in the surface winds, one expects the stress to be more sensitive than the winds, consistent with Fig. 4.4. (Note that one of the CM2.1 runs has a very small trend, as seen in the lower right panel.) Roughly speaking, the trend in the reanalysis is a poleward shift plus a strengthening of the westerlies, whereas the model trends are closer to being simply a poleward shift, so the models and observations agree more quantitatively when examining the latitude of the westerlies, as in Fig. 4.3, than when one compares the amplitude of the wind or stress trends.

To the extent that the tropospheric winds are, in fact, driven by the lower stratospheric winds, these differences between models and reanalysis may result from model

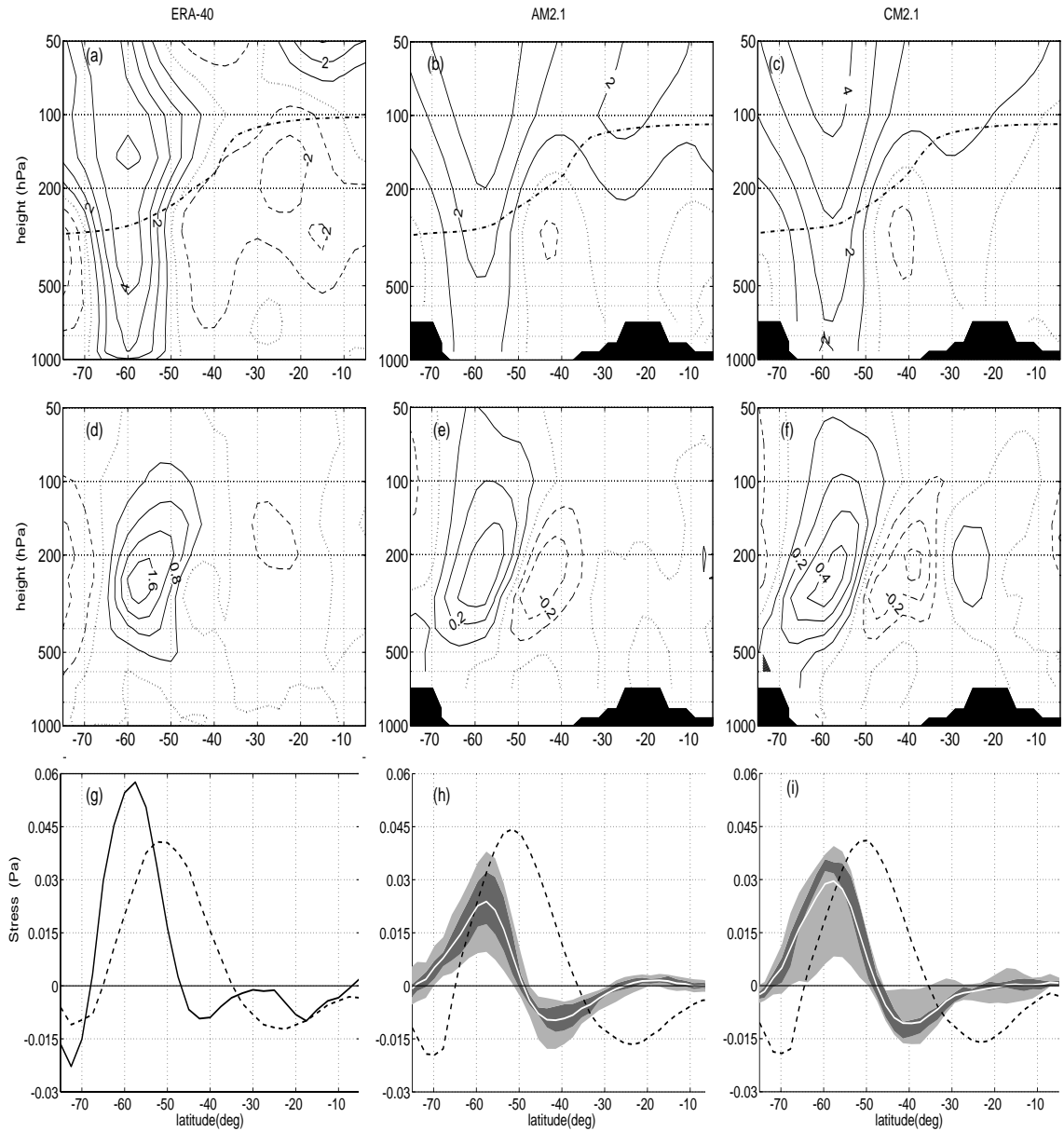


Figure 4.4: The linear trends of (top) DJFM-averaged zonal mean zonal wind, (middle) transient eddy momentum flux convergence and (bottom) zonal mean surface stress for (left) ERA-40, and for the ensemble means of (middle) AM2.1 and (right) CM2.1. The heavy dashed line in (a)-(c) is the tropopause level, estimated by the standard WMO lapse-rate criterion. The contour intervals are 1 m/s/(40 year) for (a)-(c), 0.4 m/s/day/(40 year) for (d), 0.1 m/s/day/(40 year) for (e) and (f). The black/white solid lines in (g)-(i) are the ensemble mean surface stress trends, and the dashed lines are 1/4 of the mean surface stress climatologies. The surface stress trends for the ensemble experiments are ranked and plotted in the gray shading for (h) and (i) as in Fig. 4.3.

deficiencies in producing too weak a stratospheric wind signal. Since the models provide rather accurate simulations of the climatological stress distribution, as also shown in Fig. 4.4, it is more difficult to argue that horizontal resolution or some other deficiency in the tropospheric simulations is the primary cause of this discrepancy. Reference to Miller et al. (2006) suggests that the trend in winds in CM2.1 is at least as large as that in other coupled models compared in that study. As discussed by Marshall (2003), the annular mode trend in the reanalysis may be overestimated due to the data quality in early decades or the transition of data sources.

The model deficiency in the amplitude of the trends is more dramatic in the eddy momentum fluxes themselves, where, despite the agreement in the pattern of the trends, the magnitude is a factor of 4 smaller than ERA-40 in CM2.1 and even smaller in AM2.1. This difference in scaling is surprising given the zonal momentum balance between the eddy momentum flux convergence and surface stress. This discrepancy may be related to the absence of an exact balance in the angular momentum budget in the reanalysis (Huang et al., 1999), whereas the models have a more consistent balance.

Since the poleward shifts of surface westerlies and tropospheric zonal winds are simulated by the models fairly well, although the magnitude of the wind response is weak, we proceed to test our hypothesis on eddy phase speeds by computing the ensemble means of eddy momentum flux convergence spectra in the upper troposphere for AM2.1 and CM2.1 (Fig. 4.5). The eddy spectra in AM2.1 are smoother than for CM2.1, due to the larger ensemble size. The models do indeed display trends similar in structure to the observed trend in Fig. 4.1, although the amplitudes are weak as expected from Fig. 4.4. As is especially clear in the AM2.1 composite, the model results confirm that the poleward shift of the momentum flux convergence is associated with an increase in the contribution from waves with angular phase speeds close to the fastest waves present in the climatology, rather than the slower phase

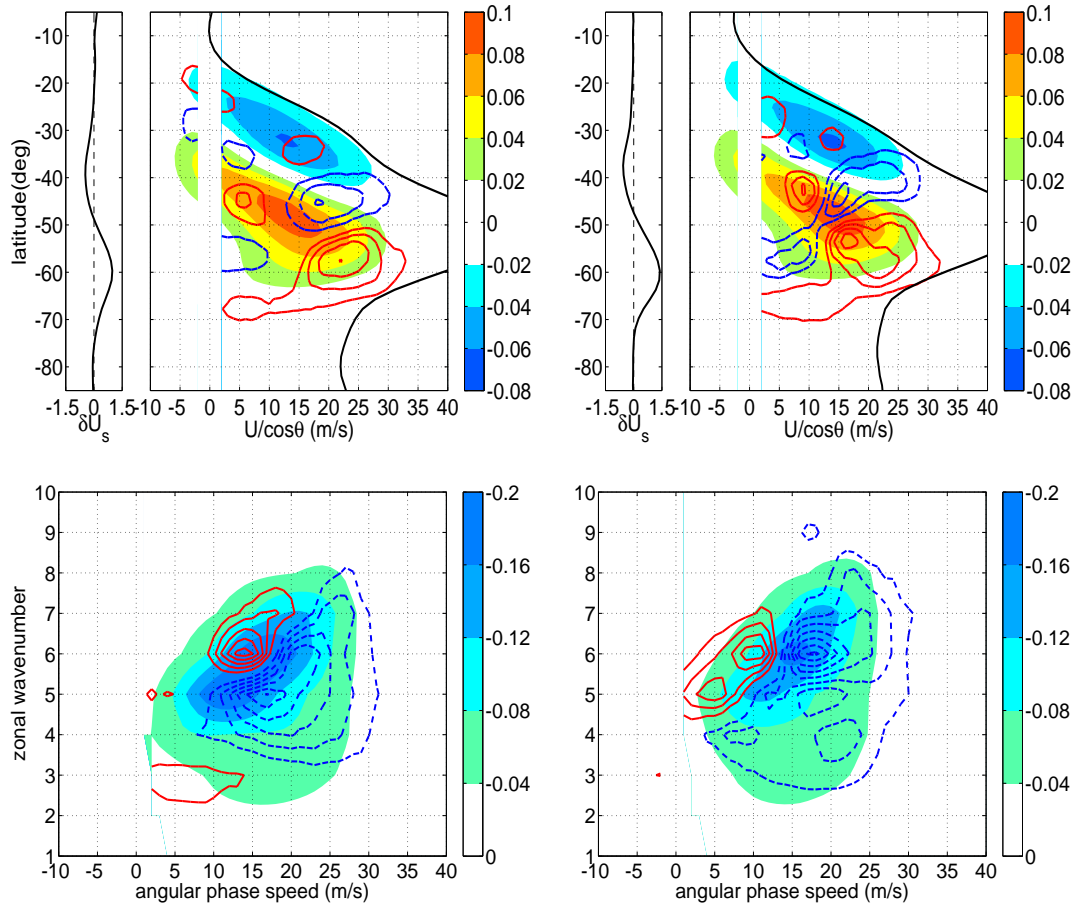


Figure 4.5: The (shading) climatological means and (contours) linear trends of the eddy spectra at 250 hPa in DJFM, for (left) AM2.1 and (right) CM2.1. The figure denotes the (top) *eddy momentum flux convergence* as a function of latitude and angular phase speed, and (bottom) *eddy momentum flux* as a function of zonal wavenumber and angular phase speed with a cosine weighted average between 55°S and 45°S. In the top panels, the black solid lines denote the time and zonally averaged zonal winds at 250hPa divided by $\cos \theta$, in comparison with the spectra, and the trends of zonally averaged 10 meter surface winds, on the left of the spectra. The contour intervals are (top) 0.004 m/s/day/(40 year) and (bottom) 0.01 m^2/s^2 /(40 year). The red (blue) color denotes the positive (negative) value.

speeds that dominate the climatological flux.

In the wavenumber-phase speed spectra averaged about the momentum flux trend maximum, the model ensemble means display a much smoother structure than the observations in Fig. 4.1. The Rossby wave dispersion relationship is especially coherent in AM2.1 for both the climatological mean and long-term trend, which shows clearly that the trend of the eddy activity in the regions of surface westerlies is characterized by a large increase in phase speed and a slight change in zonal wavenumber. As the trend in eddy momentum flux is summed over wavenumbers, the cancellations in the dominant eddies, due to the shift in phase speed, result in the largest contribution from the fastest eddies.

While the vertical resolution of AM2.1 and CM2.1 is not optimal for studies of troposphere-stratosphere interactions, the zonal wind trends in the lower stratosphere should not be strongly influenced by resolution, as the wind trends are in a simple thermal wind balance with the temperature changes associated with the strong forcing by the ozone hole. Furthermore, the comparison with the observations suggests that the effect of these wind changes on the phase speed of midlatitude eddies can be qualitatively captured in a model of this type, but it is possible that there are quantitative deficiencies due to inadequate vertical resolution. It will be of interest to examine the changes in eddy dynamics in models of much higher vertical resolution in the future.

4.4 The interannual variability

In this section, we study the interannual variability in the latitude of surface westerlies and the spectra of upper tropospheric eddies in ERA-40 and the same AM2.1 ensemble of experiments used for the linear trends in section 4.3. Although the AM2.1 integrations display a trend driven by time-varying radiative forcings, the statistics

of interannual variability are almost the same as those in another AM2.1 ensemble of experiments with fixed radiative forcings, that is, the interannual variability is primarily due to the internal dynamics and the SST variations. Our focus is the similarity and difference in the spatial patterns between two hemispheres and between the SST-forced and intrinsic variability. The spatial patterns are obtained from linear regressions onto the detrended and standardized indices of ENSO and internal variability. We compute the regression patterns of most fields, using 24 years (1979-2002) in ERA-40 and 10 realizations of 21 years (1979-1999) in AM2.1. Despite improved data quality in the reanalysis after 1979, our results are similar when the data prior to the satellite era are included. Therefore, in calculating the eddy momentum flux spectrum, we use 44 years (1959-2002) in ERA-40 so as to increase the statistical significance in the spectral space. Also, we use 10 realizations of 40 years (1960-1999) in AM2.1 to compute the eddy spectrum, although the result is nearly unchanged with only half of the record.

4.4.1 The ENSO-induced variability

Figure 4.6 shows the regressions onto the ENSO cycle of the monthly and zonally averaged 10 meter surface zonal wind anomalies for ERA-40 and for the ensemble mean in AM2.1. The ENSO cycle is described by the detrended and standardized Cold Tongue Index (CTI), defined as the SST anomalies averaged between 6°N - 6°S and 180° - 90°W (Deser and Wallace, 1990), and the regression onto the inverted CTI represents the cold phase of the ENSO cycle. The seasonal variation of surface winds in ERA-40 is consistent with that of the extratropical upper tropospheric winds documented in Seager et al. (2003) and L'Heureux and Thompson (2006). In particular, the Southern Hemisphere (SH) surface westerlies in ERA-40 are displaced poleward relative to the westerly maximum in the months of November-February, and the Northern Hemisphere (NH) surface westerlies display a considerable weakening on the equa-

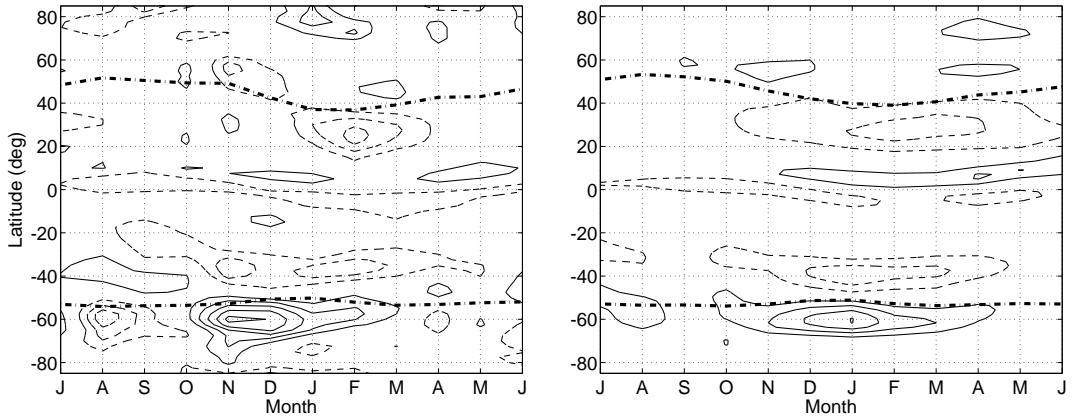


Figure 4.6: The regressions onto the inverted CTI of the monthly and zonally averaged 10 meter surface zonal wind anomalies for (left) ERA-40 and (right) the ensemble mean in AM2.1. The dotted-dashed lines denote the position of the climatological mean westerly maxima. The contour intervals are 0.15 m/s.

forward side of the westerly maximum in the months of January-March. The model can simulate the observed wind pattern rather well except for the SH wind peak in November, which might be related to the strong stratosphere-troposphere coupling in the SH in November, that is not well resolved at the model vertical resolution. Therefore, we focus on the seasonal average from December-March, in which the surface wind responses in both hemispheres are notable and well simulated in the model. Our results are qualitatively similar even if November is included.

Figure 4.7 shows the spatial pattern of DJFM mean zonal wind anomalies at the surface and 250 hPa regressed onto the inverted CTI for ERA-40 and the AM2.1 ensemble mean. The zonal winds are characterized by anomalous surface easterlies and upper tropospheric westerlies over the tropical Pacific ocean. There is a hemispherically symmetric weakening in the upper tropospheric winds over the subtropical Pacific, as expected from cooler-than-normal SST anomalies in the tropical Pacific and the thermal wind relationship. In the extratropics, the SH surface westerlies displace poleward over the Pacific and Atlantic oceans, but the NH westerlies are weakened on the equatorward side in the Pacific, and exhibit almost no change in

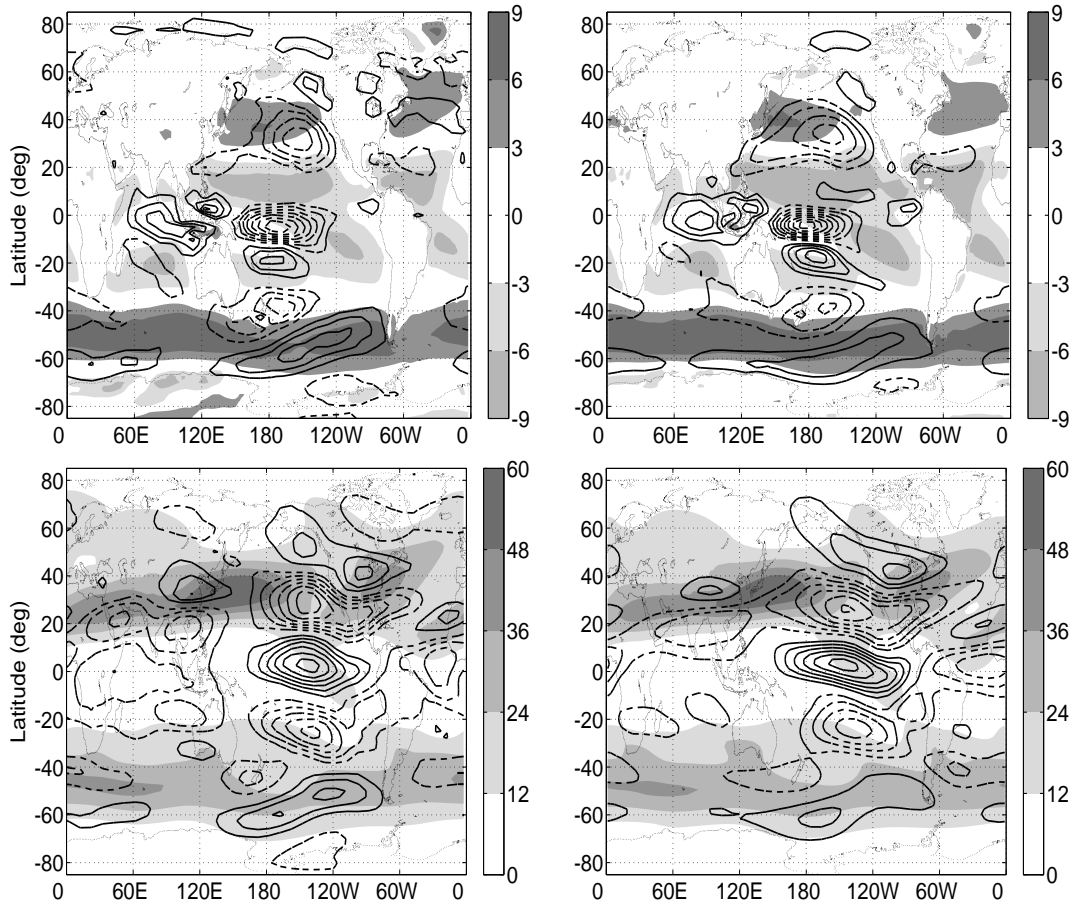


Figure 4.7: The spatial pattern of DJFM mean zonal wind anomalies at (top) the surface and (bottom) 250 hPa regressed onto the inverted CTI for (left) ERA-40 and (right) the AM2.1 ensemble mean. The shading represents the climatological mean winds. The contour intervals are (top) 0.3 m/s, and (bottom) 1 m/s.

the Atlantic. The extratropical wind change has an equivalent barotropic structure in the vertical, and extends eastwards in the upper levels. All these tropical and extratropical circulation responses associated with the cold phase of ENSO cycle are well simulated in the model. As is noted in Seager et al. (2003) and L’Heureux and Thompson (2006), the zonal wind change associated with the ENSO cycle bears a great degree of hemispheric symmetry over the Pacific ocean, and a notable zonally symmetric component especially in the SH and in the NH upper troposphere.

We quantify the variability of surface westerlies by defining the surface westerly latitude (SWL) as the mean latitude of zonally averaged surface westerlies in midlat-

itudes weighted by the wind strength.

$$\text{SWL} = \int_{20^\circ}^{70^\circ} \phi(\bar{u} \cos \phi) d\phi / \int_{20^\circ}^{70^\circ} (\bar{u} \cos \phi) d\phi \quad (\text{for } \bar{u} > 0) \quad (4.1)$$

Where \bar{u} denotes the zonal mean surface zonal wind. The time series of SWL represents the meridional movement of surface westerlies, and is highly correlated with indices of annular modes, but we do not need to define an EOF mode here. The relationship between the detrended CTI and SWLs of two hemispheres in DJFM is illustrated in Fig. 4.8 for ERA-40 and for the AM2.1 ensemble mean with the spread among 10 realizations. Both the reanalysis and the model show a statistically significant correlation between CTI and the SH SWL, as is easily seen in the figure that the El Niño years are associated with the equatorward shift of SH surface westerlies. The correlation coefficient is 0.55 for ERA-40, and the average of correlations in AM2.1, $\sum r_i \sigma_i / (\sum \sigma_i^2)^{1/2}$ (where r_i, σ_i are the correlation coefficient and standard deviation for the i th realization), is 0.52, suggesting that ENSO explains about 1/4 of the latitudinal variability of SH surface westerlies, consistent with the observed correlation between CTI and the SAM (L’Heureux and Thompson, 2006). However, the NH SWL is not significantly correlated with CTI, which is especially obvious in the SWL time series in the reanalysis. Our definition of SWL permits to separate the contributions to the variability of surface westerlies between the North Atlantic and North Pacific, suggesting that this is due to the North Atlantic surface westerlies, which are not linearly correlated with CTI in the reanalysis and model (Fig. 4.7). Keeping this zonal asymmetry in mind, we proceed to examine the zonally averaged response in the extratropical circulations.

We compare the ENSO-induced anomalies in the surface winds and upper tropospheric eddies, for ERA-40 and for the AM2.1 ensemble means with the spread among 10 realizations. Figure 4.9 shows the climatological means and ENSO regres-

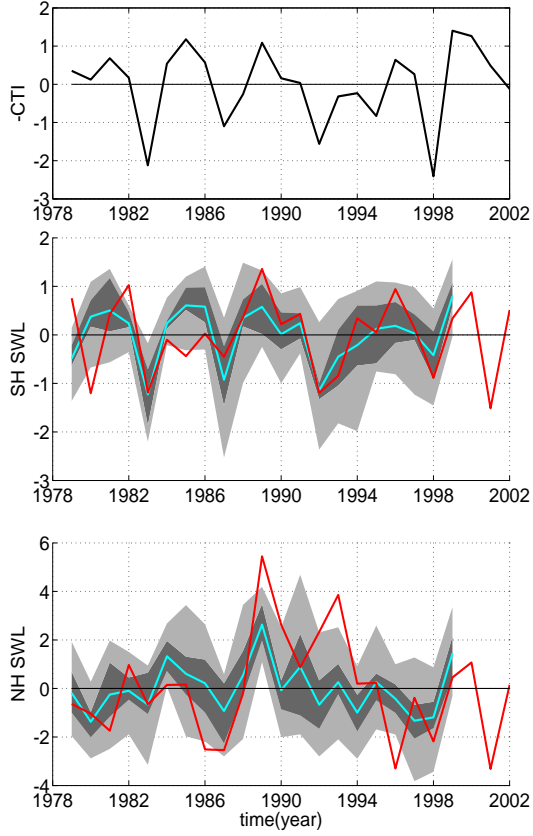


Figure 4.8: The DJFM averaged (top) detrended and standardized inverted Cold Tongue Index (CTI), the ensemble means and spreads of the detrended SWLs in the (middle) SH and (bottom) NH from 1979-2002. SWL is the surface westerly latitude defined in Eq. (4.1), and the positive value represents a poleward shift. The red and cyan lines denote the SWLs for ERA-40 and the model ensemble mean, respectively. The SWLs in each year for the ensemble experiments are ranked in an ascending order as $y_i (i = 1, \dots, 10)$. The shading is between $(y_1 + y_2)/2$ and $(y_9 + y_{10})/2$, in which the dark shading is between $(y_3 + y_4)/2$ and $(y_7 + y_8)/2$.

sion patterns of the DJFM and zonally averaged surface stress, and the corresponding transient and stationary eddy momentum flux convergence with a pressure-weighted average between 100-500 hPa. The stationary eddies are defined by the DJFM seasonal means, and transient eddies are the deviations from the season means.

The model can simulate a consistent response in circulation remarkably similar to the reanalysis. In the extratropics, the SH surface westerlies shift poleward, consistent with the movement of transient eddy momentum flux convergence in the upper troposphere. In contrast, the NH surface westerlies are mainly reduced on the equatorward side of the westerly maximum, and the ensemble mean increase on the poleward side in the model is smaller than the spread among different realizations. In the upper troposphere, the transient momentum flux convergence displaces poleward, but this displacement is undermined by anomalous stationary eddy flux, which displays a seemingly opposite effect to transients in ERA-40 and a small ensemble mean response with a large fluctuation among the AM2.1 realizations. In the subtropics, the transient eddy momentum flux divergence moves polewards in both hemispheres, while anomalous stationary eddies strengthen the climatological stationary divergence at about 20°N. From the perspective of angular momentum balance, the surface westerly movement linearly related to ENSO is mainly driven by transient eddies rather than stationary eddies in the upper troposphere, although the momentum flux convergence is somewhat offset by the mountain torque in the NH (not shown). In particular, the anomalous transient eddy flux in the upper troposphere displays a latitudinal fluctuation between divergence and convergence, with a great degree of hemispheric symmetry.

We decompose the transient eddy momentum flux convergence at 250 hPa as a function of latitude and angular phase speed for ERA-40 and the AM2.1 ensemble mean (Fig. 4.10). We use angular phase speed (phase speed divided by $\cos \phi$) in the plot, and the spectrum emphasizes more on the subtropics than that in Randel and

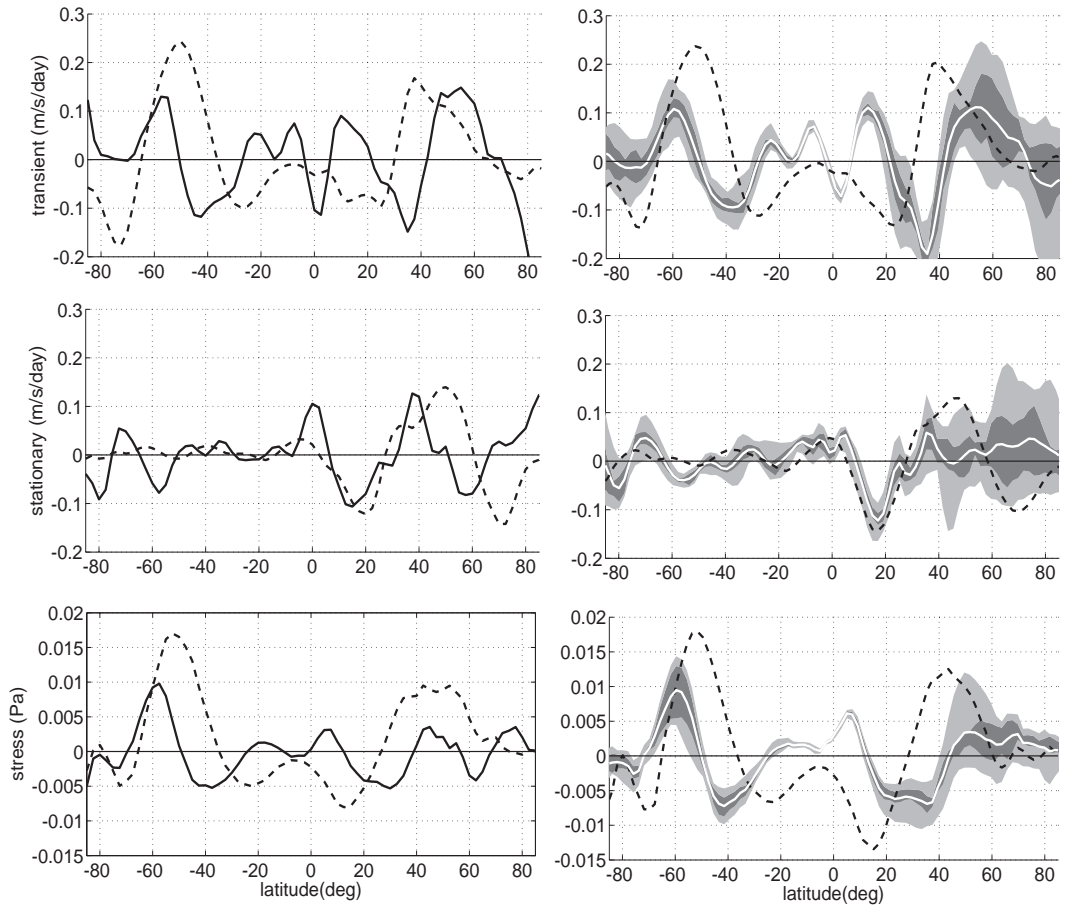


Figure 4.9: The ENSO-induced anomalies in the surface stress and upper tropospheric eddy momentum flux convergence, for (left) ERA-40 and for (right) the AM2.1 ensemble means with the spread among 10 realizations. The black/white solid lines are the ENSO regression patterns of the DJFM and zonally averaged (bottom) surface stress, and the corresponding (top) transient and (middle) stationary eddy momentum flux convergence with a pressure-weighted average between 100-500 hPa, and the dashed lines are 1/10 of the climatological means. The model ensemble spread is ranked and plotted in gray shading as in Fig. 4.8.

Held (1991). The anomalous pattern is obtained by regressing the eddy spectrum of 120-day DJFM time series in each year onto the inverted CTI. The spectra show a striking hemispheric symmetry in the divergence and convergence anomalies for both the reanalysis and model. In the subtropics, the anomalous eddy momentum flux displays a meridional dipolar structure parallel to the subtropical critical line, implying the poleward shift of the subtropical momentum flux divergence. As is evident in the figure, the midlatitude eddies in the climatology cannot penetrate beyond their critical latitudes, and thus the poleward shift of the subtropical divergence can be attributed to the weakening of subtropical winds during the cold ENSO phase, which prevents the equatorward penetration of midlatitude eddies. In the extratropics, the momentum flux convergence displaces poleward, with strong anomalous convergence about 50°N in the reanalysis. This displacement can be thought of as the result of either the poleward refraction of transient eddies or the feedback accompanying the poleward movement of the upper level jets and surface temperature gradients.

Since the model spectrum is similar to the observation and smoother due to a large ensemble of experiments, we further examine the transient eddy momentum flux at a given latitude as a function of zonal wavenumber and phase speed for the AM2.1 ensemble mean (Fig. 4.11). The eddy spectra are averaged in 10 degrees of latitudes with a cosine weighting about the climatological mean midlatitude convergence and subtropical divergence maxima in two hemispheres, and these averaged spectra represent the mean phase speed and zonal wavenumber of transient eddies being generated in the midlatitudes or being absorbed in the subtropics. As these latitudes also roughly coincide with anomalous eddy momentum flux maxima or minima, the averaged spectra capture the characters of eddies responsible for anomalous movement of surface westerlies.

In the SH, the climatological mean eddy spectra averaged in midlatitudes (55°S - 45°S) are dominated by eddies with zonal wavenumbers of 5-6 and angular phase

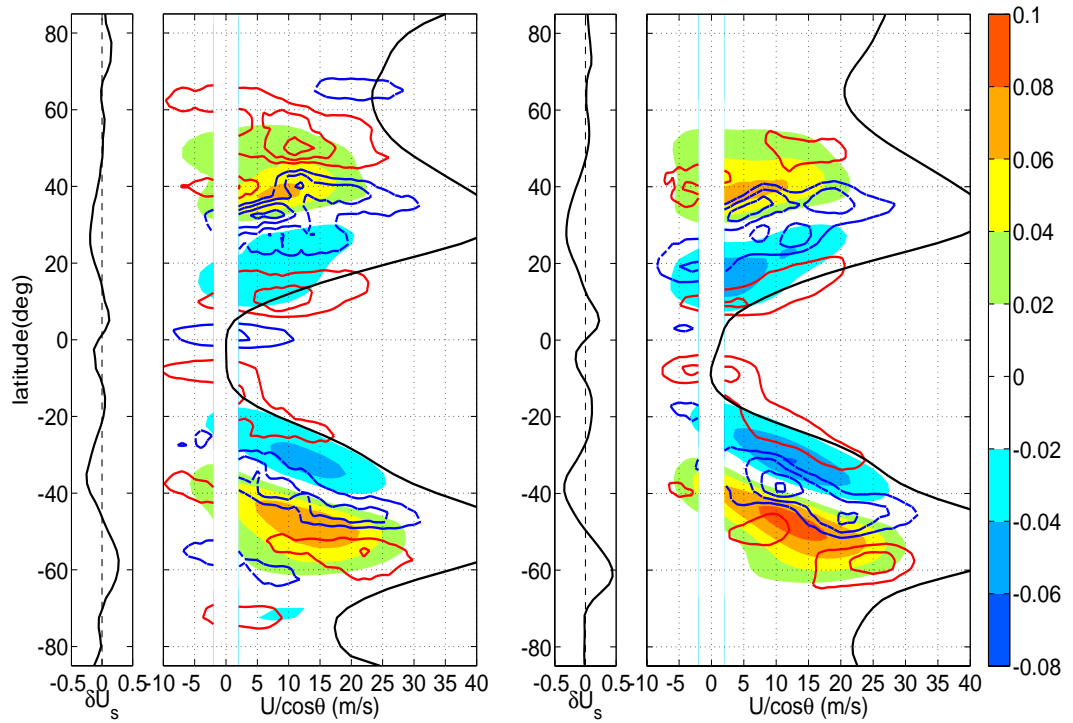


Figure 4.10: The (shading) climatological means and (contours) ENSO-induced anomalies in the *eddy momentum flux convergence* as a function of latitude and angular phase speed at 250 hPa in DJFM, for (left) ERA-40 and (right) the AM2.1 ensemble mean. The black solid lines denote the time and zonally averaged zonal winds at 250hPa divided by $\cos \theta$, in comparison with the spectra, and the anomalies of zonally averaged 10 meter surface winds, on the left of the spectra. The contour intervals are 0.002 m/s/day. The red (blue) color denotes the positive (negative) value.

speeds of 10~20 m/s, while the eddies averaged in subtropics (35°S-25°S) are dominated by wavenumbers of 4-5 and phase speeds of 0~10 m/s, as expected since slower eddies can propagate further equatorward than faster eddies. The ENSO-induced eddy anomalies averaged in midlatitudes have nearly the same dispersion relationship as the dominant eddies generated in the climatology, although the fastest and shortest waves are increased. Meanwhile, the anomalous spectra averaged in subtropics show a considerable reduction of eddies faster than the eddies typically reaching and being absorbed in the subtropics in the climatology. This is consistent with the mechanism described in Seager et al. (2003) that transient eddies are refracted poleward due to the weakening of subtropical winds and the poleward shift of critical lines. One should note that the increase in fastest eddies with phase speeds of 20~30 m/s in midlatitudes is related to the anomalous convergence at 60°S in the latitude-phase speed spectra (Fig. 4.10), and that the overall increase in the momentum flux averaged in 55°S-45°S may just reflect the poleward shift of the momentum flux with a peak at about 30°N in the mean climate (Fig. 4.9).

The NH eddy response is analogous to the SH but with more complexity. The climatological mean eddy spectra are dominated by medium-scale eddies of wavenumbers 5-6 and planetary-scale eddies of wavenumber 3 in both midlatitudes (15°N-25°N) and subtropics (35°N-45°N). In the midlatitudes, the medium-scale eddies extend in the wavenumber-phase speed space in a manner similar to the dispersion relationship in the SH, and therefore they are likely to be generated through baroclinic instability. The planetary-scale eddies are quasi-stationary, likely to be forced by zonal asymmetries in the lower boundary conditions such as topography or diabatic heating (Held et al., 2002). Notice that they both have a characteristic period larger than 15 days, indicated by the black dashed line in the figure. In the cold phase of ENSO cycle, the medium-scale eddy response is similar to the SH counterpart, characterized by the weakening of faster eddies among all the disturbance arriving at the subtropics, and

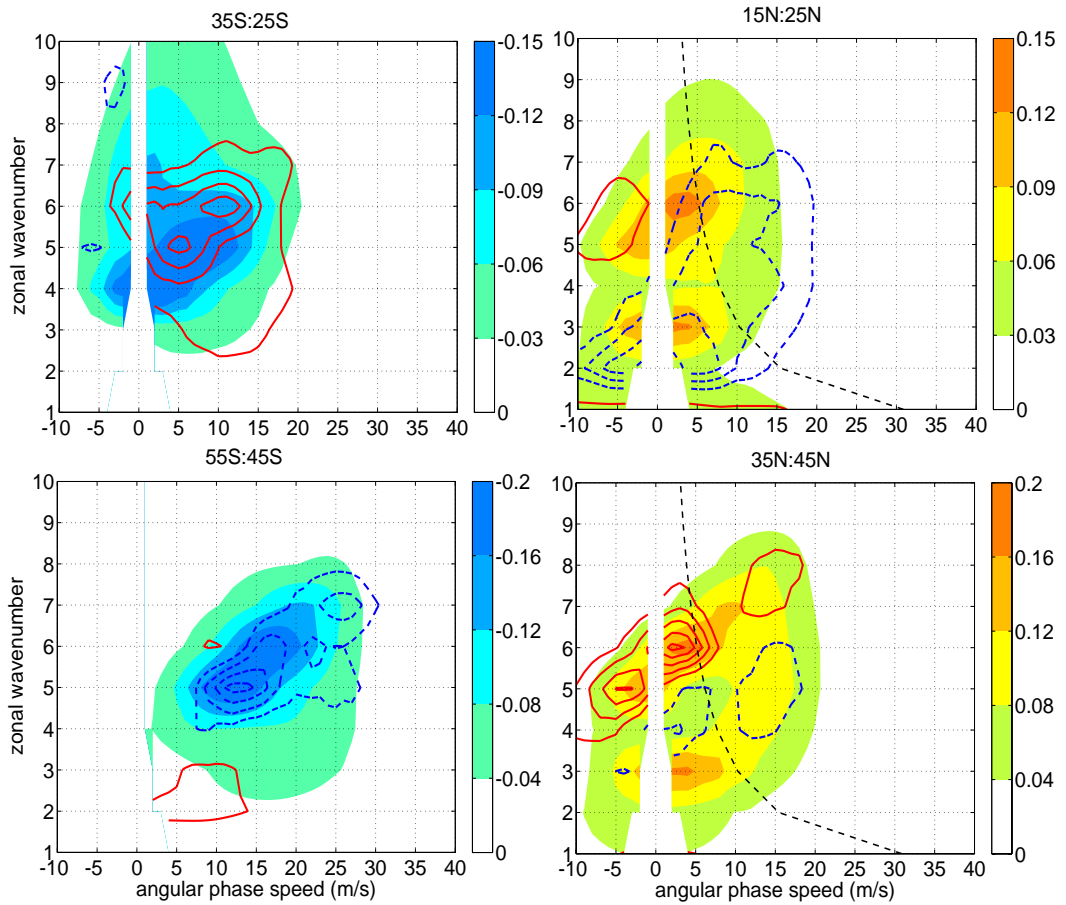


Figure 4.11: The (shading) climatological means and (contours) ENSO-induced anomalies in the *eddy momentum flux* as a function of zonal wavenumber and angular phase speed at 250 hPa in DJFM for the AM2.1 ensemble mean. The spectra are averaged in latitude bands of (left) 35°S-25°S, 55°S-45°S, (right) 15°N-25°N, 35°N-45°N. The contour intervals are $0.004 \text{ m}^2/\text{s}^2$. The black dashed line in the right panels denotes the period of 15 days. The red (blue) color denotes the positive (negative) value.

the poleward refraction of midlatitude eddies implied by the wavenumber-phase speed distribution coincident with the climatological distribution. However, the planetary-scale eddy response in the model appears mainly in the subtropics, dominated by the weakening of eddy momentum flux transport by zonal wavenumber 2. The difference in medium-scale and planetary-scale eddies may be attributed to the nature by which they are generated. It may also be related to their longitudinal distributions, since ENSO is more related to surface westerlies in the North Pacific (Fig. 4.7), but it is impossible to study this difference in the space-time spectrum.

4.4.2 The internal variability

We further explore the internal interannual variability in the surface westerlies and eddy spectra independent of the SST forcing. The index of internal variability for each hemisphere is defined by removing the ensemble mean variability from the SWL time series in each realization, and the corresponding spatial pattern is attained by regressing the field of interest onto the detrended and standardized index and then averaging over 10 realizations. These regression patterns correspond to anomalous poleward shift of surface westerlies, and are referred to as the positive phase of internal variability by convention.

Figure 4.12 shows the regression patterns of DJFM mean zonal wind anomalies at the surface and at 250 hPa for the internal variability in two hemispheres. The zonal wind variability in two hemispheres displays a similar dipolar structure in latitude extending from the surface to the upper troposphere with the character of annular modes (cf. Limpasuvan and Hartmann, 2000): the SH wind anomalies are nearly zonally symmetric at all levels and the NH wind anomalies become more zonally symmetric at the higher level. In contrast to the ENSO-induced zonal wind variability, the intrinsic wind variability is more zonally symmetric and restricted only in one hemisphere. This is especially clear in the NH, where ENSO is mainly linearly related

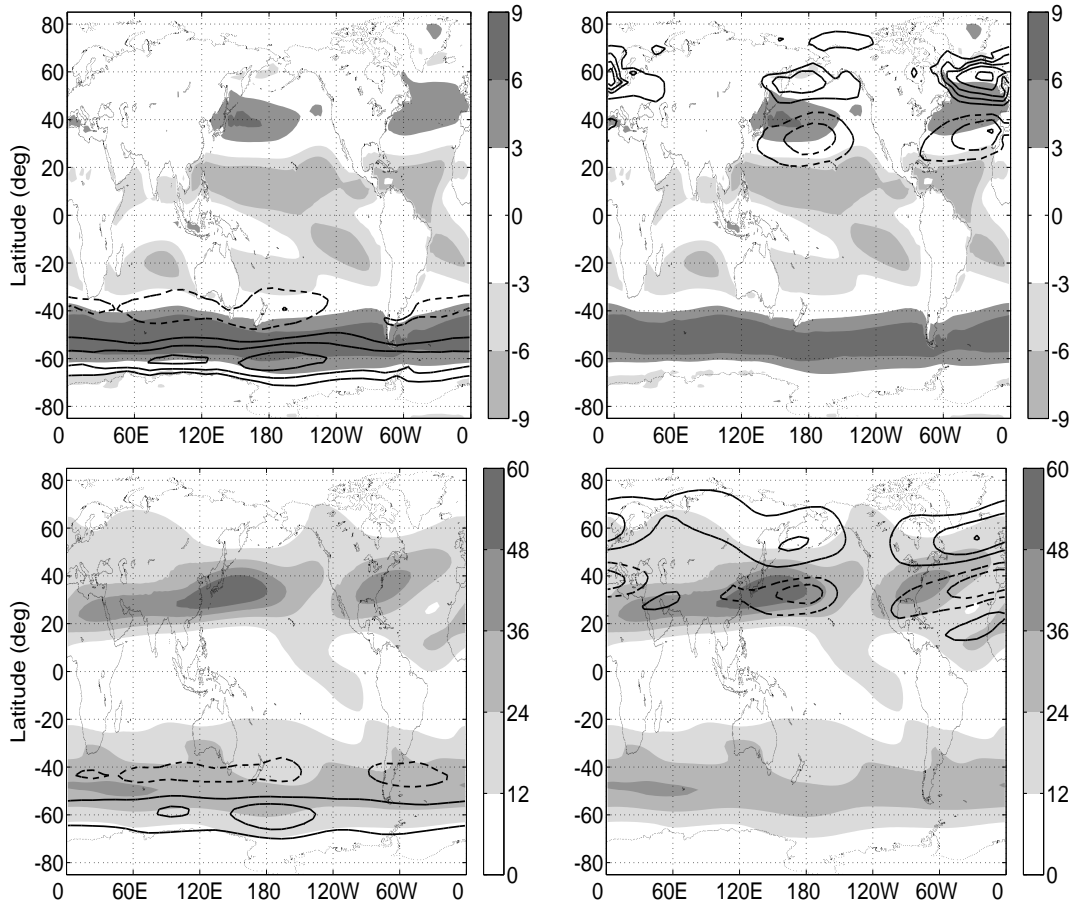


Figure 4.12: The spatial pattern of DJFM mean zonal wind anomalies at (top) the surface and (bottom) 250 hPa regressed onto the internal variability indices in the (left) SH and (right) NH. The shading represents the climatological mean winds. The contour intervals are (top) 0.3 m/s, and (bottom) 1 m/s.

to surface westerlies in the North Pacific, but the intrinsic wind variability shows a connection between the North Pacific and North Atlantic.

The intrinsic surface wind anomalies are compared with anomalous eddy momentum fluxes in the upper troposphere. Figure 4.13 shows the ensemble mean patterns regressed onto the internal variability indices in two hemispheres with the spread among 10 realizations, for the DJFM and zonally averaged surface stress, and the corresponding transient and stationary eddy momentum flux convergence with a pressure-weighted average between 100-500 hPa. The internal variability of surface westerlies in the hemisphere of interest is characterized by the meridional vacillation

about the westerly maximum, and the westerly anomalies in the other hemisphere are nearly zero in the ensemble mean, which is a key distinction from the hemispherically symmetric variability associated with ENSO. While the intrinsic surface westerly anomalies in the SH are mainly driven by transient eddies in the upper troposphere, the intrinsic surface westerly anomalies in the NH are driven by both stationary and transient eddies. The latter is not inconsistent with Limpasuvan and Hartmann (2000), which concludes that the stationary eddies, defined by monthly means, contribute most to the eddy momentum flux associated with the NH annular mode. In comparison with the SST-forced response, while the intrinsic transient momentum flux anomalies in the SH display a similar dipolar structure in midlatitudes, the intrinsic convergence anomalies in the NH occur at higher latitudes, with a peak at about 60°N . Moreover, the stationary eddies display intrinsic momentum flux anomalies in NH midlatitudes that appear, at least in the model, not to be directly related with ENSO.

The transient eddy momentum flux convergence at 250hPa is plotted as a function of latitude and angular phase speed (Fig. 4.14). In the SH, the intrinsic eddy momentum flux anomalies mark the divergence at 40°S and convergence at 60°S that are both associated with eddies with phase speeds between $15\sim 25$ m/s. In the NH, while there is a noticeable anomalous divergence maximum at about 35°N with phase speeds between $10\sim 20$ m/s, the anomalous convergence maximum is less well-defined and spans over the latitudes of $50^\circ\text{N}\sim 70^\circ\text{N}$. The zonally averaged convergence anomalies (Fig. 4.13) exhibit a peak value at 60°N , which can be attributed to the eddies with phase speeds between $0\sim 10$ m/s. Therefore, the phase speed spectra illustrate a distinction between the eddies associated with the internal dynamics in two hemispheres: while the SH intrinsic variability is mainly associated with faster eddies in the climatological spectra, the NH intrinsic variability involves all the eddies maintaining the mean climate.

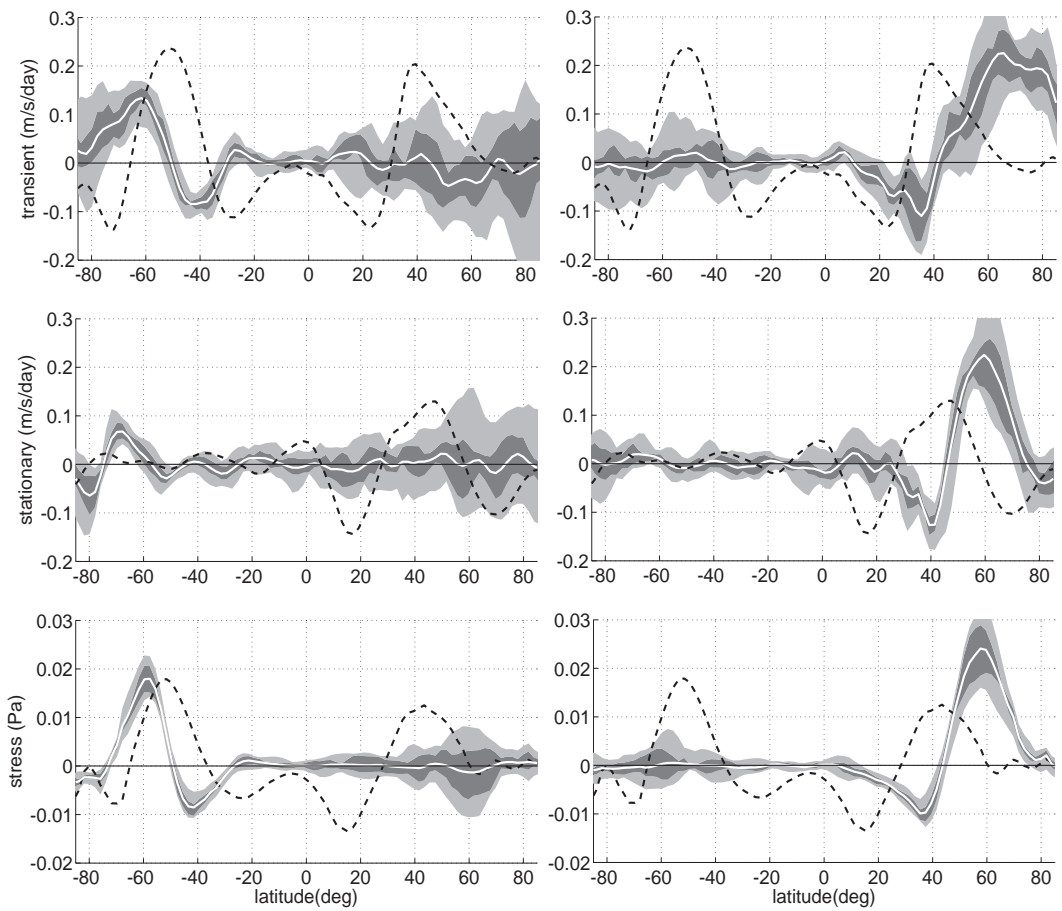


Figure 4.13: The internal variability in the surface stress and upper tropospheric eddy momentum flux convergence, with the spread among 10 realizations, for the (left) SH and (right) NH. The black/white solid lines are the regression patterns of the DJFM and zonally averaged (bottom) surface stress, and the corresponding (top) transient and (middle) stationary eddy momentum flux convergence with a pressure-weighted average between 100-500 hPa, and the dashed lines are 1/10 of the climatological means. The model ensemble spread is ranked and plotted in gray shading as in Fig. 4.8.

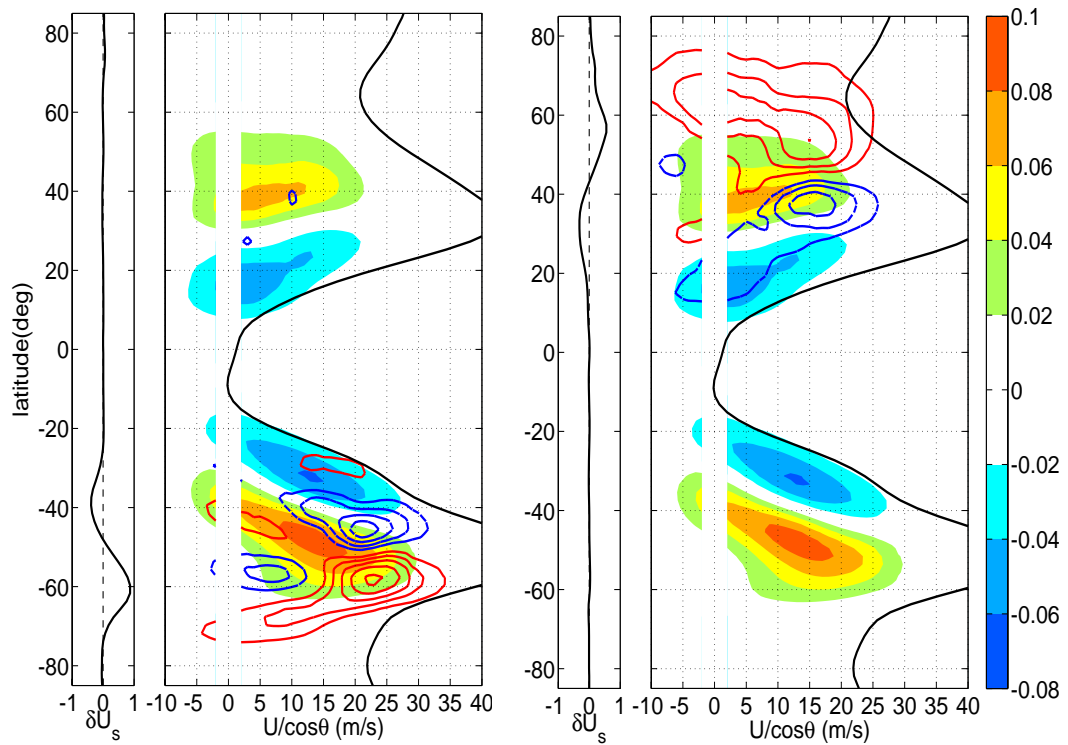


Figure 4.14: The (shading) climatological means and (contours) internal variability patterns in the *eddy momentum flux convergence* as a function of latitude and angular phase speed at 250 hPa in DJFM, in (left) the SH and (right) NH. The black solid lines denote the time and zonally averaged zonal winds at 250hPa divided by $\cos \theta$, in comparison with the spectra, and the anomalies of zonally averaged 10 meter surface winds, on the left of the spectra. The contour intervals are 0.002 m/s/day. The red (blue) color denotes the positive (negative) value.

The transient eddy momentum flux at 250hPa is further examined in the zonal wavenumber-phase speed space (Fig. 4.15). In the SH, the eddy momentum flux anomalies averaged in midlatitudes (55°S-45°S), in the positive phase of internal variability, are characterized by a coherent spectral structure with a large increase in phase speed and a small change in zonal wavenumber. In the NH, the momentum flux is averaged in two midlatitude bands of 35°N-45°N and 45°N-55°N, and the latter emphasizes more on the quasi-stationary eddies (Fig. 4.14). The medium-scale and planetary-scale eddies display two distinct regression patterns. The anomalous medium-scale eddies have characteristic phase speeds between 10~20 m/s, and the comparison with Fig. 4.14 indicates that the associated eddy forcing is well projected onto the surface wind vacillation, as the SH counterpart. The anomalous planetary-scale eddies are dominated by quasi-stationary eddies of phase speeds between -5~10 m/s, and the comparison with Figs. 4.13 and 4.14 suggests that they are largely responsible for the anomalous convergence at 60°N. The anomalous quasi-stationary planetary-scale eddies have similar phase speeds and wavenumbers to the climatological means, consistent with the interpretation that these eddies are refracted poleward in the positive phase of the NAM (Limpasuvan and Hartmann, 2000; Lorenz and Hartmann, 2003).

The space-time spectra provide detailed information on the eddy characters related to the internal variability. For example, the anomalous medium-scale and planetary-scale eddies in the NH reveal two distinct time scales roughly separated by a 15-day period, which is employed as a cut-off period in Lorenz and Hartmann (2003) for the high-frequency eddies associated with the NAM variability. Moreover, the spectra provide new insights on the annular mode variability, that the positive phase of annular modes is associated with the increased phase speeds of medium-scale eddies, along with the poleward shift in the propagation and absorption of Rossby waves in the upper troposphere. But the eddy spectrum alone cannot settle the

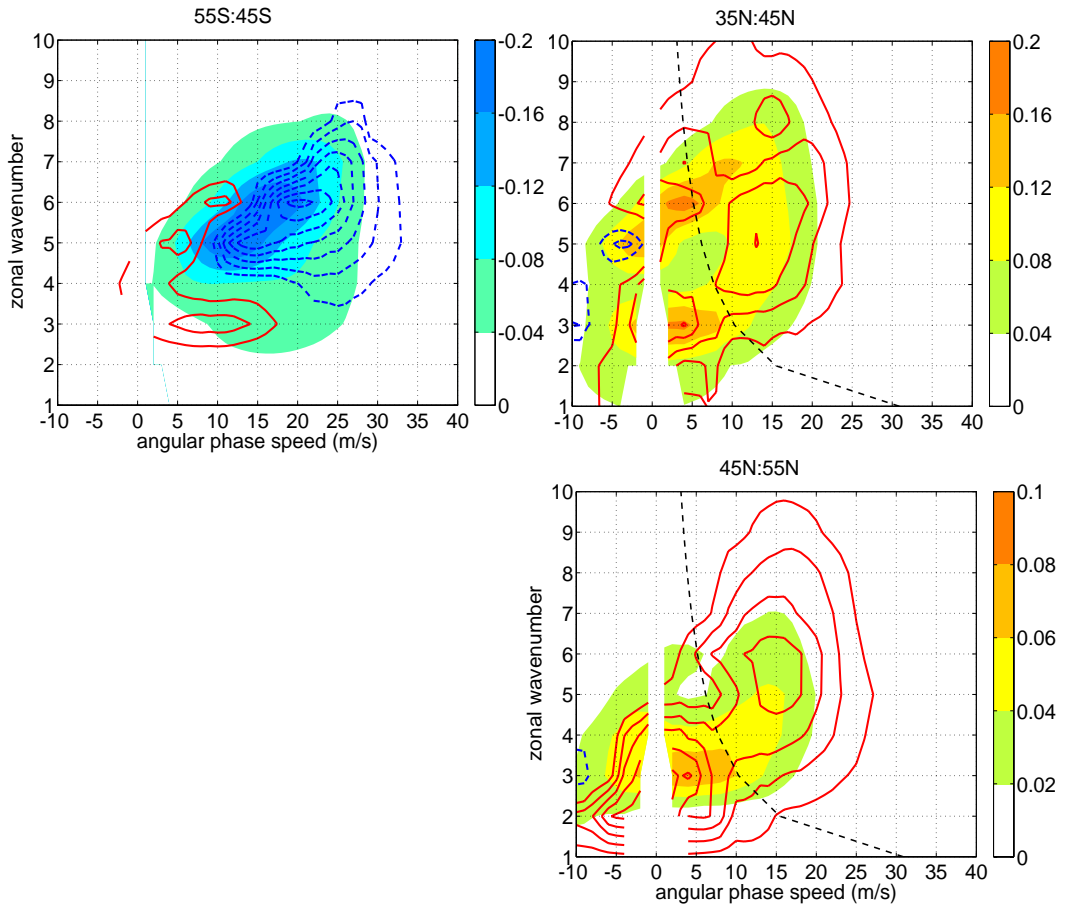


Figure 4.15: The (shading) climatological means and (contours) internal variability patterns in the *eddy momentum flux* as a function of zonal wavenumber and angular phase speed at 250 hPa in DJFM for the (left) SH and (right) NH. The spectra are averaged in latitude bands of (left) 55°S-45°S, (right) 35°N-45°N, 45°N-55°N. The contour intervals are $0.004 \text{ m}^2/\text{s}^2$. The black dashed line in the right panels denotes the period of 15 days. The red (blue) color denotes the positive (negative) value.

causality relationship.

The eddy phase spectrum also reveals the difference between the intrinsic and ENSO-forced variability. While the intrinsic eddy variability occurs mostly in the midlatitude convergence and the eddies faster than typical eddies in the mean climate, the ENSO-induced change is largely in the subtropical divergence and nearly all the phase speeds, especially in the AM2.1 ensemble mean. For the medium-scale eddies in the midlatitudes, the positive phase of internal variability is best described as a poleward shift associated with increased eddy phase speeds, but the ENSO response displays relatively little change in eddy characters, consistent with a poleward refraction by the subtropical wind anomalies.

4.5 The projected trends in the 21th century

In this section, we study the responses to global warming (IPCC A2 scenario) in the latitude of surface westerlies and the eddy spectra in CM2.1, and compare them with the ENSO-induced and intrinsic interannual variability. We use the 20-year means of 2001-2020 as the climatology for this section, and the global warming response is the 20-year means of 2081-2100 subtracted by the climatological means.

Figure 4.16 shows the response of the monthly and zonally averaged 10 meter surface winds in CM2.1. The surface westerlies displace poleward in both hemispheres in the annual mean. The displacement in SH westerlies is notable nearly all year around, but the shift in NH westerlies exhibits a seasonal dependence with a peak in the boreal winter. As we are particularly interested in the comparison between the interannual variability and global warming trend, we again look at the DJFM seasonal mean.

Figure 4.17 shows the spatial pattern of the DJFM mean zonal wind response at the surface and at 250 hPa. The surface westerlies displace poleward in both hemi-

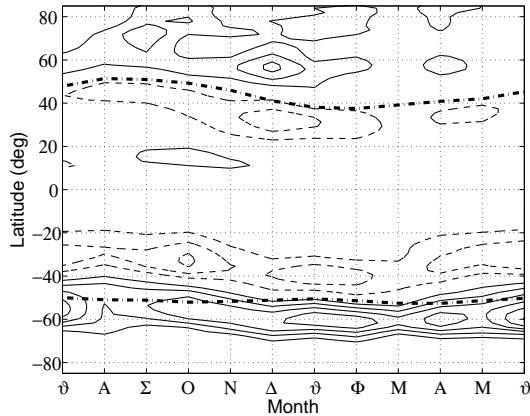


Figure 4.16: The response to global warming of the monthly and zonally averaged 10 meter surface zonal winds in CM2.1. The dotted-dashed lines denote the position of the climatological mean westerly maxima. The contour intervals are 0.4 m/s.

spheres, and the wind anomalies have a zonally symmetric component that resembles those in the internal variability than in the ENSO-induced variability. The resemblance becomes less in the upper troposphere. In the SH, the midlatitude jet moves poleward with anomalous westerlies in the subtropics, analogous to the separation of the eddy-driven jet from the subtropical jet in idealized models, as the equator-to-pole temperature gradients or water vapor contents are altered (e.g. Son and Lee, 2005; Frierson et al., 2006). In the NH, while the zonal wind response is less clear on the equatorward flank of the Pacific and Atlantic jets, the zonal wind on the poleward flank is intensified and more zonally symmetric.

We examine the upper tropospheric momentum flux responses associated with the displacement of surface westerlies. Figure 4.18 shows the responses for the DJFM and zonally averaged surface stress, and the corresponding transient and stationary eddy momentum flux convergence with a pressure-weighted average between 100-500 hPa. From the angular momentum balance, the surface wind shift in the SH is mainly driven by transient eddy momentum fluxes, but for the surface westerly movement in the NH, both transient and stationary eddies are important. While the transient eddy response in two hemispheres displays a poleward shift similar to the positive

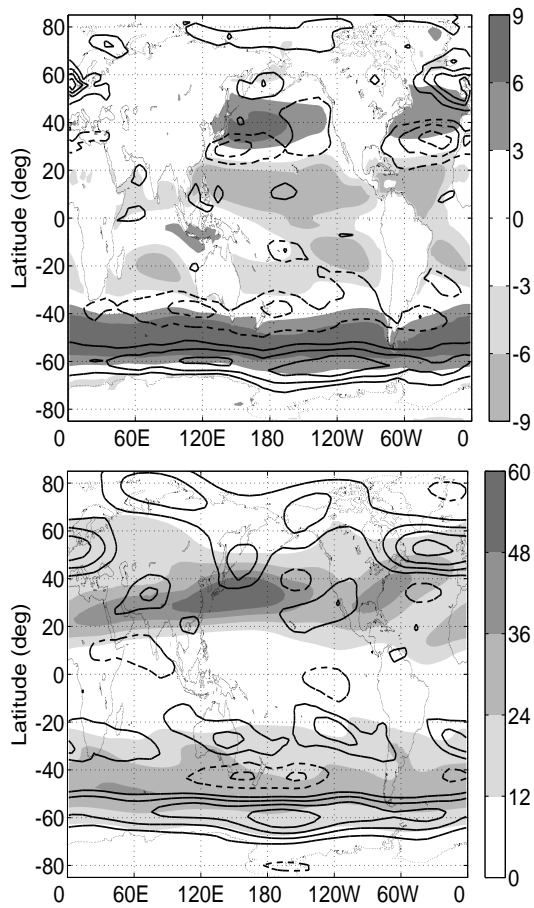


Figure 4.17: The spatial pattern of the DJFM mean zonal wind response to global warming at (top) the surface and (bottom) 250 hPa. The shading represents the climatological mean winds. The contour intervals are (top) 0.6 m/s, and (bottom) 1.5 m/s.

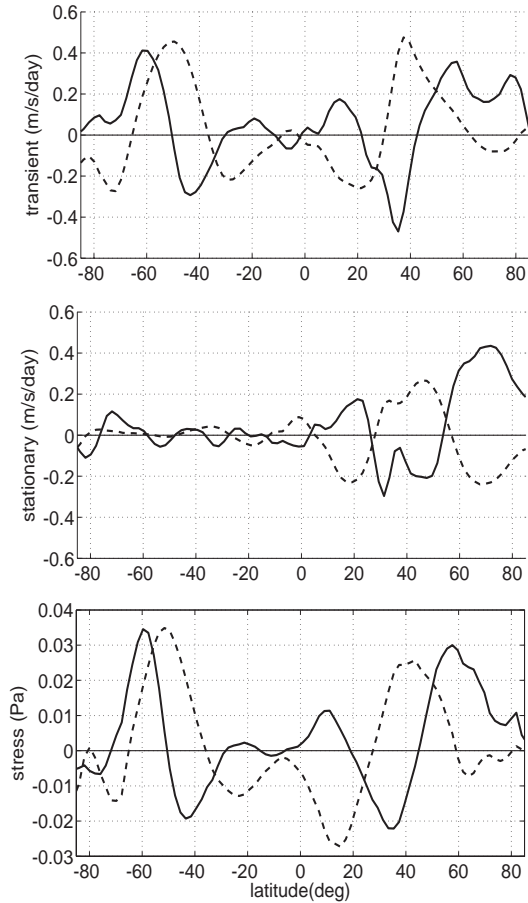


Figure 4.18: The response to global warming in the surface stress and upper tropospheric eddy momentum flux convergence. The black/white solid lines are the responses of the DJFM and zonally averaged (bottom) surface stress, and the corresponding (top) transient and (middle) stationary eddy momentum flux convergence with a pressure-weighted average between 100-500 hPa, and the dashed lines are 1/5 of the climatological means.

phase of internal variability, the stationary eddy response in the NH is more of a weakening than of a shift relative to the climatological mean (Joseph et al., 2004). Moreover, the anomalous stationary momentum flux convergence at about 40°N is not very well-defined.

The response of transient eddy momentum flux convergence at 250hPa is plotted in the latitude-phase speed spectrum (Fig. 4.19). In the SH, both the eddy momentum flux convergence and divergence increase in the phase speeds at 15~30 m/s and decrease somewhat in the phase speeds at 0~15 m/s, and the decrease in the

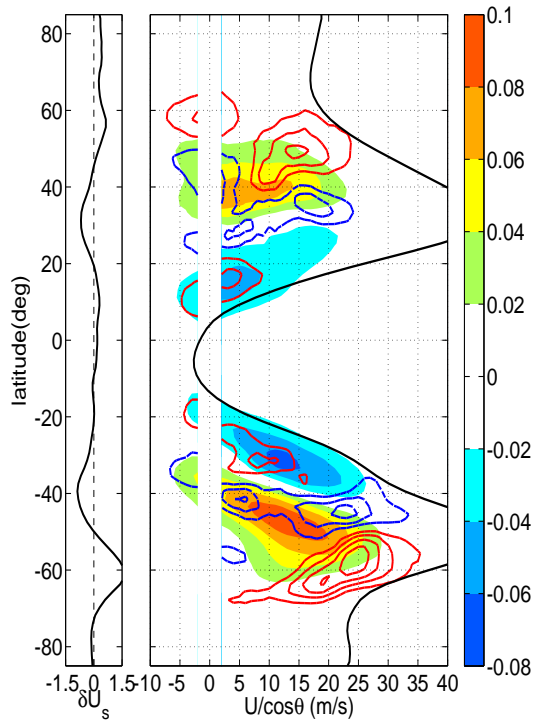


Figure 4.19: The (shading) climatological means and (contours) the global warming response in the *eddy momentum flux convergence* as a function of latitude and angular phase speed at 250 hPa in DJFM. The black solid lines denote the time and zonally averaged zonal winds at 250hPa divided by $\cos\theta$, in comparison with the spectra, and the response of zonally averaged 10 meter surface winds, on the left of the spectra. The contour intervals are 0.006 m/s/day. The red (blue) color denotes the positive (negative) value.

subtropical divergence at 20°S-40°S is related to the subtropical westerly anomalies in Fig. 4.17. In the NH, the subtropical divergence and midlatitude convergence, like their SH counterparts, display an increase in phase speed from -5~5 m/s to 10~20 m/s, except that there is anomalous convergence by quasi-stationary eddies at about 60°N. The response in quasi-stationary eddies corresponds to the weakening of stationary waves in Fig. 4.18. In both hemispheres, the increases in eddies with faster phase speeds are remarkably similar to the anomalous patterns in the positive phase of internal variability, yet in the response to global warming, the decreases in slower phase speeds become noticeable as well. As the subtropical critical latitude of midlatitude eddies tilts poleward for more rapid eastward propagation, the increased eddy phase speeds are accompanied by the poleward shift of the subtropical momentum flux divergence.

The transient eddy momentum flux at 250hPa is again plotted in the wavenumber-phase speed spectra averaged about anomalous eddy flux maxima and minima (Fig. 4.20). In the SH, the eddy momentum flux averaged in midlatitudes (55°S-45°S) displays an increase in phase speed with little change in wavenumber, roughly following the slope of the dispersion relationship. The change in phase speed is also evident in the subtropics (35°S-25°S), where the dominant eddies are slower than those diverging from the midlatitudes, and the response of subtropical eddies can be roughly traced back to their midlatitude origins. In the NH, the medium-scale eddies respond to global warming by a similar increase in phase speed in the subtropics (15°N-25°N) and midlatitudes (35°N-45°N), although the pattern is less well-defined. For the medium-scale eddies in both hemispheres, the increased momentum fluxes in faster phase speeds are similar to those in the positive phase of internal variability, but the decreased momentum fluxes in slow phase speeds become more noticeable in the global warming response. The planetary-scale eddies also show an increased poleward momentum flux transport by zonal wavenumber 2 in the latitudes of 45°N-55°N,

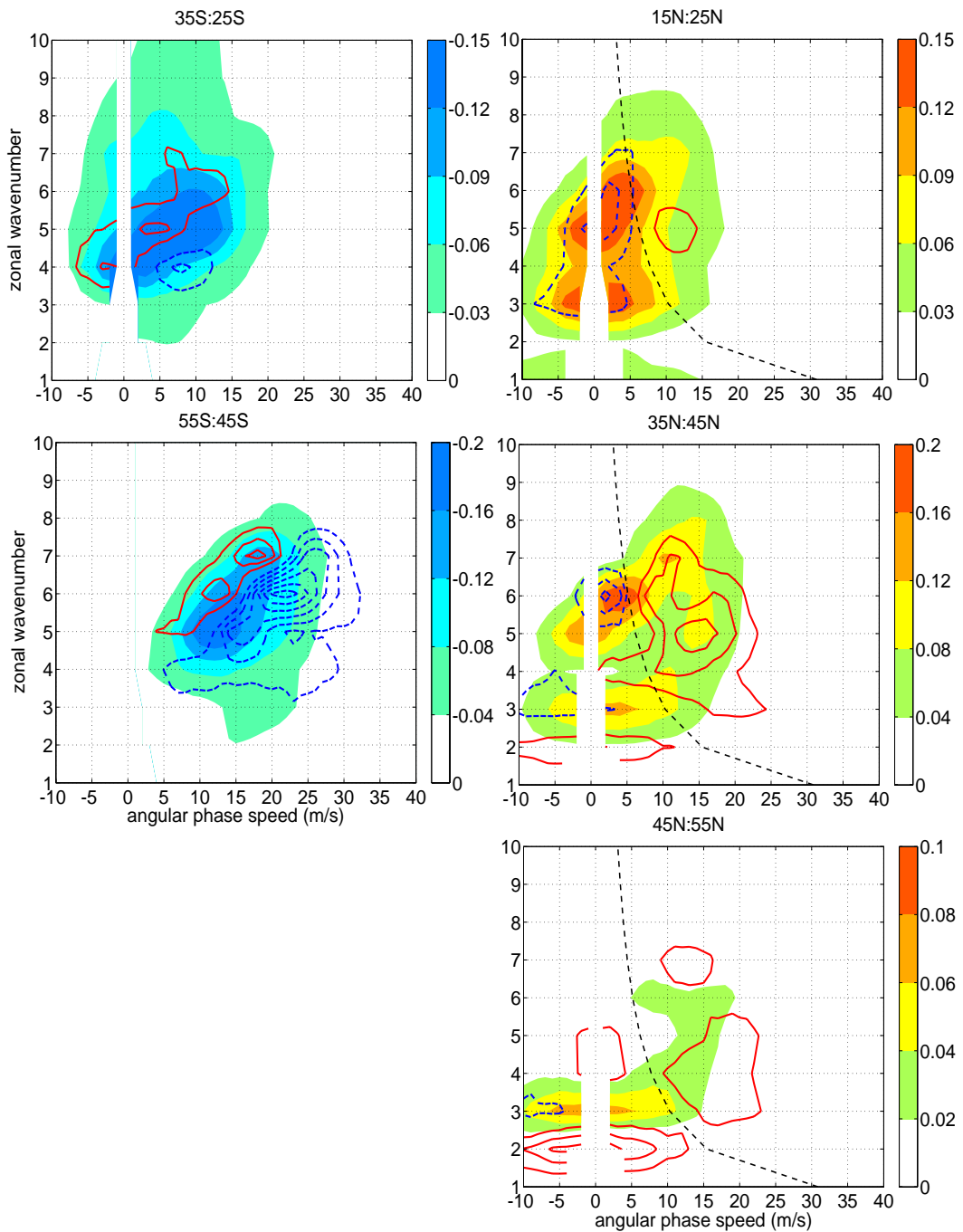


Figure 4.20: The (shading) climatological means and (contours) global warming responses in the *eddy momentum flux* as a function of zonal wavenumber and angular phase speed at 250 hPa in DJFM. The spectra are averaged in latitude bands of (left) 35°S-25°S, 55°S-45°S, (right) 15°N-25°N, 35°N-45°N, 45°N-55°N. The contour intervals are $0.02 \text{ m}^2/\text{s}^2$. The black dashed line in the right panels denotes the period of 15 days. The red (blue) color denotes the positive (negative) value.

similar to the positive phase of internal variability. The spectra also disclose that the response of quasi-stationary eddies consists of the contributions from both medium-scale eddies and planetary-scale eddies, which may be related to the discontinuity in the stationary momentum flux convergence at 40°N in Fig. 4.18.

4.6 Conclusions and Discussions

In this chapter, we have identified and compared the patterns of interannual variability and long-term trends in the latitude of surface westerlies and the space-time eddy momentum flux spectra, in the reanalysis data and in the coupled and atmosphere-only climate models.

The interannual variability of dominant midlatitude eddies displays distinct patterns with respect to the internal variations due to atmospheric eddy-mean flow interactions, and to the SST-forced variations during the ENSO cycle. While the response to ENSO is consistent with the refraction of midlatitude eddies due to the subtropical wind anomalies, the internal variability marks a change in the eastward propagation speed of midlatitude eddies. Furthermore, the dominant eddies exhibit a trend towards faster eddy phase speeds in response to global warming in both hemispheres and to ozone depletion in the Southern Hemisphere, in a manner similar to the positive phase of interannual internal variability. As the result of the shift in phase speed, the quasi-stationary eddies contribute less to the trends of surface westerlies than to the intrinsic variability of surface westerlies.

It has been shown in chapter 3 that the increased extratropical stratospheric winds can lead to the poleward shift in the tropospheric jet. Therefore, we suggest that both the observed shift in the Southern Hemisphere and the projected shift in both hemispheres in the future can be explained, at least in part, as a consequence of increased zonal winds near the tropopause or in the lower stratosphere. In the case of global

warming, tropical upper tropospheric warming and stratospheric cooling combine to create this increase in winds; in the late 20th century, the polar stratospheric cooling due to the Antarctic ozone hole has contributed to, if not dominated, this increase in winds aloft in the Southern Hemisphere. These increased winds accelerate the eastward phase speeds of midlatitude eddies, shifting the subtropical breaking region polewards, resulting in a poleward shift of the eddy momentum flux convergence and the associated surface and tropospheric winds.

Lorenz and DeWeaver (2007) find that the poleward shift of zonal winds in IPCC models is associated with an increase in the tropopause height, and show that similar changes in circulation can be simulated in a simple GCM by directly varying the tropopause height. While nearly identical simple model simulations in Williams (2006) show that the tropopause height change and the jet shift are associated with a change in eddy scale, our space-time spectral analysis shows that the changes in eddy momentum fluxes are dominated by an increase in eddy phase speeds in the GFDL coupled model. Lorenz and DeWeaver (2007) have also shown that the ensemble mean zonal wind response in IPCC models is significantly correlated with the cooling over the polar cap in the lower stratosphere, which is consistent with the importance of the subpolar lower stratospheric winds as we suggest.

Chapter 5

Conclusions

In this thesis, we study the factors that control the latitude of surface westerlies and tropospheric jet streams, to understand the extratropical zonal mean circulation response to climate change. Our discussions are primarily built on a quasi-linear perspective of the atmosphere, in which Rossby waves propagate equatorward in the upper troposphere and transfer angular momentum from the subtropics into the midlatitude jets. The fundamental key to this view is the conservation of pseudomomentum (a measure of wave activity) in the absence of sources and sinks, and the orthogonality of pseudomomentum distribution among the modes of various eddy scales and phase speeds (Held, 1985).

We starts from a simple way to shift the jet latitude in chapter 2, in which, when the surface friction is reduced in an idealized dry atmosphere model, the midlatitude jets and surface westerlies are displaced poleward (Robinson, 1997). We first confirm that the poleward jet shift is mainly controlled by the friction on zonal means, and then examine the transient response to a reduction in surface friction. In the transient response, the eddy kinetic energy decreases substantially in the first 10-20 days, due to the development of barotropic shears ("barotropic governor" in James (1987)), but the poleward jet movement persists up to 100 days, associated with relatively little

change in eddy kinetic energy. We conclude from this that eddy kinetic energy is not the key for this type of jet movements.

In the space-time spectrum of eddy momentum fluxes, we find that the poleward jet shift is associated with the increased eastward propagation of midlatitude eddies. As the rapid transient adjustment is characterized by the zonal wind acceleration in midlatitudes, we argue that the increased eastward eddy phase speed is the consequence of the accelerated midlatitude jet, which in turn leads to the poleward shift in the upper-tropospheric eddy momentum fluxes, and the associated eddy-driven upper level jet and surface westerlies.

In chapter 3, we utilize a prescribed zonal torque to justify the importance of the phase speeds and the subtropical critical latitudes of midlatitude eddies. The tropospheric jet shifts poleward for the westerly (easterly) torque on the poleward (equatorward) flank of the jet center in the troposphere. This is consistent with the picture of Rossby wave propagation: the increased eastward phase speed of midlatitude eddies results in the wave activity absorption at more poleward critical latitudes, and the weakening of subtropical winds prevents midlatitude eddies from propagating into the deep tropics. The fast and slow eddies respond differently in the two cases, which can be seen in the latitude-phase speed spectrum. The mechanism is illustrated schematically in Fig. 5.1.

Also shown in chapter 3, the tropospheric jet shifts poleward for a westerly torque in the extratropical stratosphere. The zonal wind anomalies in the stratosphere are mainly transferred downwards into the troposphere by stratospheric eddies rather than the residual circulations through "downward control" (Haynes et al., 1991). We argue that the stratospheric zonal wind anomalies can affect the tropospheric jet by altering the eastward propagation of tropospheric eddies. However, further research is necessary to examine in detail how the stratospheric planetary-scale eddies interact at the tropopause level with the tropospheric medium-scale eddies. Such interactions are

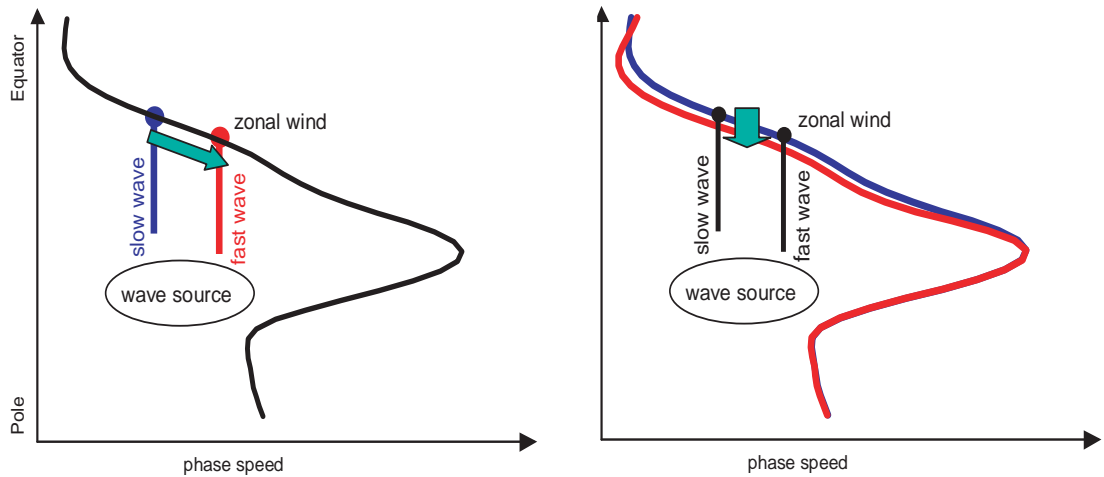


Figure 5.1: A schematic diagram for the changes in the critical latitudes of midlatitude eddies with respect to the changes in (left) the eddy phase speeds and (right) the subtropical winds. The figure shows schematically that as the eddy phase speeds are increased or the subtropical winds are decreased (indicated by the arrow from the blue curve to the red curve), the critical latitudes of midlatitude eddies are displaced poleward.

also observed, although not fully understood, in the life cycle of sudden stratospheric warming (Limpasuvan et al., 2004).

Lastly, in chapter 4, we have examined the interannual variability and long-term trend in the surface westerlies and eddy momentum flux spectra. The interannual variability displays distinct patterns with respect to the internal variability due to atmospheric eddy-mean flow interactions, and to the SST-forced variability during the ENSO cycle. The former involves the variations in the extratropical eddy phase speeds, the latter is related to the subtropical wind anomalies associated with the variations in sea surface temperatures, and their differences can also be explained by Fig. 5.1. Furthermore, the annular mode trends, due to stratospheric ozone depletion or global warming, are associated with the trends towards faster eastward eddy phase speeds similar in pattern to the positive phase of internal interannual variability. This suggests that the observed and simulated shifts of surface westerlies are more

related to the processes for the extratropical internal variability such as the variations in stratospheric polar vortex, rather than those for the tropical-extratropical interactions.

These results suggest a unifying mechanism, helping to explain the response of the circulation to stratospheric ozone reduction and to global warming, and more generally, the influence of the stratosphere on tropospheric annular mode-like anomalies: *An increase in lower stratospheric/upper tropospheric zonal winds increases the eastward phase speed of tropospheric eddies, and this increase in phase speed, by displacing the region of subtropical wave breaking polewards, shifts the eddy momentum fluxes polewards, as well as the surface westerlies that are maintained by these momentum fluxes.* This mechanism can be related to the poleward propagation of zonal wind anomalies in the upper troposphere (Lee et al., 2007). It may also provide a new view for the annular mode variability, in addition to current understandings from a stochastic perspective (see the review in Vallis and Gerber (2007)).

Our mechanism on the latitude of surface westerlies depends on the latitude of eddy momentum divergence in the upper troposphere. Alternatively, one may relate the movement of surface westerlies to the latitude of eddy momentum divergence or eddy heat flux. From the diffusive eddy closure point of view, the lower tropospheric eddy heat flux can be determined by the background potential vorticity gradient (e.g. Held, 1999), or by the energy balance in a moist model (e.g. Frierson et al., 2007). However, the jet latitude is sensitive to zonal wind anomalies in the upper troposphere/lower stratosphere, and the zonal wind response to idealized and realistic climate forcings retains a quasi-barotropic structure. Therefore, a theory for the barotropic decay of midlatitude eddies seems to be more relevant than a theory for the baroclinic production. Since it is the coupling between the upper troposphere and lower troposphere that results in baroclinic eddy production, the picture is completed by the claim that this shift in upper tropospheric eddies is accompanied by a shift in

the eddy production as well.

Bibliography

- Abatzoglou, J. T. and G. Magnusdottir, 2006: Planetary wave breaking and nonlinear reflection: Seasonal cycle and interannual variability. *J. Climate*, **19**, 6139–6152.
- Akahori, K. and S. Yoden, 1997: Zonal flow vacillation and bimodality of baroclinic eddy life cycles in a simple global circulation model. *J. Atmos. Sci.*, **54**, 2349–2361.
- Anderson, J. and coauthors, 2004: The new GFDL global atmosphere and land model AM2/LM2: Evaluation with prescribed SST simulations. *J. Climate*, **17**, 4641–4673.
- Andrews, D. G., J. R. Holton, and C. B. Leovy, 1987: *Middle Atmosphere Dynamics*. Academic Press, 489 pp.
- Arblaster, J. M. and G. A. Meehl, 2006: Contributions of external forcings to southern annular mode trends. *J. Climate*, **19**, 2896–2905, doi:10.1175/JCLI3774.1.
- Baldwin, M. P. and T. J. Dunkerton, 1999: Propagation of the Arctic Oscillation from the stratosphere to the troposphere. *J. Geophys. Res.*, **104**, 30937–30946.
- 2001: Stratospheric harbingers of anomalous weather regimes. *Science*, **104**, 581–584.
- Baldwin, M. P., D. B. Stephenson, D. W. J. Thompson, T. J. Dunkerton, A. J. Charlton, and A. O’Neill, 2003: Stratospheric memory and extended-range weather forecasts. *Science*, **301**, 636–640.

- Black, R. X., 2002: Stratospheric forcing of surface climate in the Arctic Oscillation. *J. Climate*, **15**, 268–277.
- Cai, W., P. H. Whetton, and D. J. Karoly, 2003: The response of the Antarctic Oscillation to increasing and stabilized atmospheric CO₂. *J. Climate*, **16**, 1525–1538.
- Chang, E. K. M., 1995: The influence of Hadley circulation intensity changes on extratropical climate in an idealized model. *J. Atmos. Sci.*, **52**, 2006–2024.
- 1998: Poleward-propagating angular momentum perturbations induced by zonally symmetric heat sources in the tropics. *J. Atmos. Sci.*, **55**, 2229–2248.
- Chang, E. K. M. and D. B. Yu, 1999: Characteristics of wave packets in the upper troposphere. Part I: Northern hemisphere winter. *J. Atmos. Sci.*, **56**, 1708–1728.
- Chen, G. and I. M. Held, 2007: Phase speed spectra and the recent poleward shift of southern hemisphere surface westerlies. *Geophys. Res. Lett.*, submitted.
- Chen, G., I. M. Held, and W. A. Robinson, 2007: Sensitivity of the latitude of the surface westerlies to surface friction. *J. Atmos. Sci.*, in press.
- Chen, P. and W. A. Robinson, 1992: Propagation of planetary waves between the troposphere and stratosphere. *J. Atmos. Sci.*, **49**, 2533–2545.
- Delsole, T., 2001: A simple model for transient eddy momentum fluxes in the upper troposphere. *J. Atmos. Sci.*, **58**, 3019–3035.
- 2004: Stochastic models of quasigeostrophic turbulence. *Surveys in Geophys*, **25**, 107–149.
- Delworth, T. L. and coauthors, 2006: GFDL’s CM2 global coupled climate models. Part I: Formulation and simulation characteristics. *J. Climate*, **19**, 643–674.

- Deser, C. and J. M. Wallace, 1990: Large-scale atmospheric circulation features of warm and cold episodes in the tropical pacific. *J. Climate*, **3**, 1254–1281.
- Edmon, H. J., B. J. Hoskins, and M. E. McIntyre, 1980: Eliassen Palm cross sections for the troposphere. *J. Atmos. Sci.*, **37**, 2600–2616.
- Frierson, D. M. W., I. M. Held, and P. Zurita-Gator, 2006: A gray-radiation aquaplanet moist GCM. Part I: Static stability and eddy scales. *J. Atmos. Sci.*, **63**, 2548–2566.
- 2007: A gray-radiation aquaplanet moist GCM. Part II: Energy transports in altered climates. *J. Atmos. Sci.*, **64**, 1680–1693.
- Fu, Q., C. M. Johanson, J. M. Wallace, and T. Reichler, 2006: Enhanced mid-latitude tropospheric warming in satellite measurements. *Science*, **312**, 1179, doi:10.1126/science.1125566.
- Fyfe, J., G. Boer, and G. Flato, 1999: The Arctic and Antarctic Oscillations and their projected changes under global warming. *Geophys. Res. Lett.*, **26**, 1601–1604.
- Fyfe, J. C. and O. A. Saenko, 2005: Human-induced change in the Antarctic Circumpolar Current. *J. Climate*, **18**, 3068–3073.
- Gerber, E. P., S. Voronin, and L. M. Polvani, 2007: Testing the Annular Mode autocorrelation timescale in simple atmospheric general circulation models. *Monthly Weather Review*, submitted.
- Gillett, N. P. and D. W. J. Thompson, 2003: Simulation of recent southern hemisphere climate change. *Science*, **302**, 273–275.
- Haigh, J. D., M. Blackburn, and R. Day, 2005: The response of tropospheric circulation to perturbations in lower-stratospheric temperature. *J. Climate*, **18**, 3672–3685.

- Hartmann, D. L. and P. Zuercher, 1998: Response of baroclinic life cycles to barotropic shear. *J. Atmos. Sci.*, **55**, 297–313.
- Hayashi, Y., 1971: A generalized method of resolving disturbances into progressive and retrogressive waves by space fourier and time cross-spectral analyses. *J. Meteor. Soc. Japan*, **49**, 125–128.
- Haynes, P. H., C. J. Marks, M. E. McIntyre, T. G. Shepherd, and K. P. Shine, 1991: On the "downward control" of extratropical diabatic circulations by eddy-induced mean zonal forces. *J. Atmos. Sci.*, **48**, 651–678.
- Held, I. M., 1985: Pseudomomentum and the orthogonality of modes in shear flows. *J. Atmos. Sci.*, **21**, 2280–2288.
- 1999: The macroturbulence of the troposphere. *Tellus*, **51A-B**, 59–70.
- 2000: *The General Circulation of the Atmosphere..* Proc. Woods Hole Summer School on GFD, 66 pp.
- Held, I. M. and A. Y. Hou, 1980: Nonlinear axially symmetric circulations in a nearly inviscid atmosphere. *J. Atmos. Sci.*, **37**, 515–533.
- Held, I. M. and P. J. Phillips, 1987: Linear and nonlinear barotropic decay on the sphere. *J. Atmos. Sci.*, **44**, 200–207.
- 1990: A barotropic model of the interaction between the Hadley cell and a Rossby wave. *J. Atmos. Sci.*, **47**, 856–869.
- Held, I. M. and M. J. Suarez, 1994: A proposal for the intercomparison of the dynamical cores of atmospheric general circulation models. *Bull. Amer. Meteor. Soc.*, **75**, 1825–1830.
- Held, I. M., M. Ting, and H. Wang, 2002: Northern winter stationary waves: Theory and modeling. *J. Atmos. Sci.*, **15**, 2125–2144.

- Hoskins, B. J. and D. J. Karoly, 1981: The steady linear response of a spherical atmosphere to thermal and orographic forcing. *J. Atmos. Sci.*, **38**, 1179–1196.
- Huang, H. P., P. D. Sardeshmukh, and K. M. Weickmann, 1999: The balance of global angular momentum in a long-term atmospheric data set. *J. Geophys. Res.*, **104**, 2031–2040.
- James, I. N., 1987: Suppression of baroclinic instability in horizontally sheared flows. *J. Atmos. Sci.*, **44**, 3710–3720.
- James, I. N. and L. J. Gray, 1986: Concerning the effect of surface drag on the circulation of a baroclinic planetary atmosphere. *Quart. J. Roy. Meteor. Soc.*, **112**, 1231–1250.
- James, I. N. and P. M. James, 1992: Spatial structure of ultra-low frequency variability of the flow in a simple atmospheric circulation model. *Quart. J. Roy. Meteor. Soc.*, **118**, 1211–1233.
- Joseph, R., M. Ting, and P. J. Kushner, 2004: The global stationary wave response to climate change in a coupled GCM. *J. Climate*, **17**, 540–556.
- Kalnay, E. and Coauthors, 1996: The NCEP/NCAR 40-year reanalysis project. *Bull. Amer. Meteor. Soc.*, **77**, 437–471.
- Kim, H. and S. Lee, 2004: The wave-zonal mean flow interaction in the southern hemisphere. *J. Atmos. Sci.*, **61**, 1055–1067.
- Kindem, I. T. and B. Christiansen, 2001: Tropospheric response to stratospheric ozone loss. *Geophys. Res. Lett.*, **28**, 1547–1551.
- Kistler, R. and Coauthors, 2001: The NCEP-NCAR 50-year reanalysis: Monthly means CD-ROM and documentation. *Bull. Amer. Meteor. Soc.*, **82**, 247–267.

- Kushner, P. J., I. M. Held, and T. L. Delworth, 2001: Southern hemisphere atmospheric circulation response to global warming. *J. Climate*, **14**, 2238–2249.
- Kushner, P. J. and L. M. Polvani, 2004: Stratosphere-troposphere coupling in a relatively simple AGCM: The role of eddies. *J. Climate*, **17**, 629–639.
- Kwok, R. and D. A. Rothrock, 1999: Variability of Fram Strait ice flux and North Atlantic Oscillation. *J. Geophys. Res.*, **104**, 5177–5190.
- Lee, S., 1997: Maintenance of multiple jets in a baroclinic flow. *J. Atmos. Sci.*, **54**, 1726–1738.
- 2005: Baroclinic multiple zonal jets on the sphere. *J. Atmos. Sci.*, **62**, 2484–2498.
- Lee, S. and I. M. Held, 1993: Baroclinic wave packets in models and observations. *J. Atmos. Sci.*, **50**, 1413–1428.
- Lee, S. and H. Kim, 2003: The dynamical relationship between subtropical and eddy-driven jets. *J. Atmos. Sci.*, **60**, 1490–1503.
- Lee, S., S.-W. Son, K. M. Grise, and S. B. Feldstein, 2007: Mechanism of poleward propagation of zonal mean flow anomalies. *J. Atmos. Sci.*, **64**, 849–868, doi:10.1175/JAS3861.1.
- Leith, C. E., 1975: Climate response and fluctuations. *J. Atmos. Sci.*, **32**, 2022–2026.
- L’Heureux, M. L. and D. W. J. Thompson, 2006: Observed relationships between the El Niño-Southern Oscillation and the extratropical zonal-mean circulation. *J. Climate*, **19**, 276–287, doi:10.1175/JCLI3617.1.
- Limpasuvan, V. and D. L. Hartmann, 2000: Wave-maintained annular modes of climate variability. *J. Climate*, **13**, 4414–4429.

- Limpasuvan, V., D. W. J. Thompson, and D. L. Hartmann, 2004: The life cycle of the Northern Hemisphere sudden stratospheric warmings. *J. Climate*, **13**, 2584–2596.
- Lorenz, D. J. and E. DeWeaver, 2007: The tropopause height and the zonal wind response to global warming in the IPCC scenario integrations. *J. Geophys. Res.*, in press.
- Lorenz, D. J. and D. L. Hartmann, 2001: Eddy-zonal flow feedback in the Southern Hemisphere. *J. Atmos. Sci.*, **21**, 3312–3327.
- 2003: Eddy-zonal flow feedback in the Northern Hemisphere winter. *J. Climate*, **16**, 1212–1227.
- Lorenz, E. N., 1967: *The Nature and Theory of the General Circulation of the Atmosphere*. World Meteorological Organization, 161 pp.
- Lu, J., G. A. Vecchi, and T. Reichler, 2007: Expansion of the Hadley cell under global warming. *Geophys. Res. Lett.*, **34**, L06805, doi:10.1029/2006GL028443.
- Marshall, G. J., 2003: Trends in the southern annular mode from observations and reanalyses. *J. Climate*, **16**, 4134–4143.
- Marshall, J., Y. Kushnir, D. Battisti, P. Chang, A. Czaja, J. Hurrell, M. McCartney, Saravanan, and M. Visbeck, 2002: Atlantic climate variability. *International Journal of Climatology*, **21**, 1863–1898.
- Miller, R. L., G. A. Schmidt, and D. T. Shindell, 2006: Forced annular variations in the 20th century Intergovernmental Panel on Climate Change Fourth Assessment Report models. *J. Geophys. Res.*, **111**, D18101, doi:10.1029/2005JD006323.
- Norton, W. A., 2003: Sensitivity of Northern Hemisphere surface climate to simulation of the stratospheric polar vortex. *Geophys. Res. Lett.*, **30**, 1627, doi:10.1029/2003GL016958.

- Orlanski, I., 2003: Bifurcation in eddy life cycles: Implications for storm track variability. *J. Atmos. Sci.*, **60**, 993–1023.
- Panetta, R. L., 1993: Zonal jets in wide baroclinically unstable regions: Persistence and scale selection. *J. Atmos. Sci.*, **50**, 2073–2106.
- Perlwitz, J. and N. Harnik, 2003: Observational evidence of a stratospheric influence on the troposphere by planetary wave reflection. *J. Climate*, **16**, 3011–3026.
- Polvani, L. M. and P. J. Kushner, 2002: Tropospheric response to stratospheric perturbations in a relatively simple general circulation model. *Geophys. Res. Lett.*, **29**, 1114.
- Randel, W. J. and I. M. Held, 1991: Phase speed spectra of transient eddy fluxes and critical layer absorption. *J. Atmos. Sci.*, **48**, 688–697.
- Rauthe, M., A. Hense, and H. Paethn, 2004: A model intercomparison study of climate change signals in extratropical circulation. *Int. J. Clim.*, **24**, 643–662.
- Rind, D., J. Perlwitz, and P. Lonergan, 2005a: AO/NAO response to climate change: 1. Respective influences of stratospheric and tropospheric climate changes. *J. Geophys. Res.*, **110**, D12107, doi:10.1029/2004JD005103.
- Rind, D., J. Perlwitz, P. Lonergan, and J. Lerner, 2005b: AO/NAO response to climate change. Part II: Relative importance of low and high latitude temperature changes. *J. Geophys. Res.*, **110**, D12108, doi:10.1029/2004JD005686.
- Ring, M. J. and R. A. Plumb, 2007: Forced annular mode patterns in a simple atmospheric general circulation model. *J. Atmos. Sci.*, in press.
- Robinson, W. A., 1991: The dynamics of the zonal index in a simple model of the atmosphere. *Tellus*, **43A**, 295–305.

- 1997: Dissipation dependence of the jet latitude. *J. Climate*, **10**, 176–182.
 - 2000: A baroclinic mechanism for the eddy feedback on the zonal index. *J. Atmos. Sci.*, **57**, 415–422.
 - 2002: On the midlatitude thermal response to tropical warmth. *Geophys. Res. Lett.*, **29**, 1190, doi:10.1029/2001GL014158.
- Russell, J. L., R. J. Stouffer, and K. W. Dixon, 2006: Intercomparison of the southern ocean circulations in IPCC coupled model control simulations. *J. Climate*, **19**, 4560–4575, doi:10.1175/JCLI3869.1.
- Scaife, A. A., J. R. Knight, G. K. Vallis, and C. K. Folland, 2005: A stratospheric influence on the winter NAO and North Atlantic surface climate. *Geophys. Res. Lett.*, **32**, L18715, doi:10.1029/2005GL023226.
- Scott, R. K. and L. Polvani, 2006: Internal variability of the winter stratosphere. Part I: Time independent forcing. *J. Atmos. Sci.*, in press.
- Seager, R., N. Harnik, Y. Kushnir, W. Robinson, and J. Miller, 2003: Mechanisms of hemispherically symmetric climate variability. *J. Climate*, **16**, 2960–2978.
- Sexton, D. M. H., 2001: The effect of stratospheric ozone depletion on the phase of the Antarctic Oscillation. *Geophys. Res. Lett.*, **28**, 3697–3700.
- Shell, K. M. and I. M. Held, 2004: Abrupt transition to strong superrotation in an axisymmetric model of the upper troposphere. *J. Atmos. Sci.*, **61**, 2928–2935.
- Shindell, D. T. and G. A. Schmidt, 2004: Southern hemisphere climate response to ozone changes and greenhouse gas increases. *Geophys. Res. Lett.*, **31**, L18209, doi:10.1029/2004GL020724.

- Simmons, A. J. and D. M. Burridge, 1981: An energy and angular-momentum conserving vertical finite-difference scheme and hybrid vertical coordinates. *Mon. Wea. Rev.*, **109**, 758–766.
- Simmons, A. J. and B. J. Hoskins, 1980: Barotropic influences on the growth and decay of nonlinear baroclinic waves. *J. Atmos. Sci.*, **37**, 1679–1684.
- Son, S. W. and S. Lee, 2005: The response of westerly jets to thermal driving in a primitive equation model. *J. Atmos. Sci.*, **62**, 3741–3757.
- 2006: Preferred modes of variability and their relationship with climate change. *J. Atmos. Sci.*, **19**, 2063C2075, doi:10.1175/JCLI3705.1.
- Song, Y. and W. A. Robinson, 2004: Dynamical mechanisms for stratospheric influences on the troposphere. *J. Atmos. Sci.*, **61**, 1711–1725.
- Stephenson, D. B., 1994: The northern hemisphere tropospheric response to changes in the gravity-wave drag scheme in a perpetual January GCM. *Quart. J. Roy. Meteor. Soc.*, **120**, 699–712.
- Stern, W. F. and R. T. Pierrehumbert, 1988: The impact of an orographic gravity wave drag parameterization on extended range predictions with a GCM. *Preprints, Eighth Conf. on Numerical Weather Prediction*, Amer. Meteor. Soc., Baltimore, MD, 745–750.
- Stone, D. A., A. J. Weaver, and R. J. Stouffer, 2001: Projection of climate change onto modes of atmospheric variability. *J. Climate*, **14**, 3551–3565.
- Taguchi, M., 2003: Tropospheric response to stratospheric degradation in a simple global circulation model. *J. Atmos. Sci.*, **15**, 1835–1846.

- Thompson, D. W. J., M. P. Baldwin, and S. Solomon, 2005: Stratosphere-troposphere coupling in the Southern Hemisphere. *J. Atmos. Sci.*, **62**, 708–715, doi:10.1175/JAS-3321.1.
- Thompson, D. W. J., J. C. Furtado, and T. G. Shepherd, 2006: On the tropospheric response to anomalous stratospheric wave drag and radiative heating. *J. Atmos. Sci.*, **63**, 2616–2629, doi:10.1175/JAS3771.1.
- Thompson, D. W. J. and S. Solomon, 2002: Interpretation of recent southern hemisphere climate change. *Science*, **296**, 895–899.
- Thompson, D. W. J. and J. M. Wallace, 2000: Annular modes in the extratropical circulation. Part I: Month-to-month variability. *J. Climate*, **13**, 1000–1016.
- Thompson, D. W. J., J. M. Wallace, and G. C. Hegerl, 2000: Annular modes in the extratropical circulation. Part II: Trends. *J. Climate*, **13**, 1018–1036.
- Thorncroft, C. D., B. J. Hoskins, and M. E. McIntyre, 1993: Two paradigms of baroclinic wave life-cycle behaviour. *Quart. J. Roy. Meteor. Soc.*, **119**, 17–55.
- Toggweiler, J. R., J. L. Russell, and S. R. Carson, 2006: Midlatitude westerlies, atmospheric CO₂, and climate change during the ice ages. *Paleoceanography*, **21**, PA2005.
- Trenberth, K. E., G. W. Branstator, D. Karoly, A. Kumar, N. Lau, and C. Ropelewski, 1998: Progress during TOGA in understanding and modeling global teleconnections associated with tropical sea surface temperatures. *J. Geophys. Res.*, **103**, 14291–14324.
- Uppala, S. M. and coauthors, 2005: The ERA-40 re-analysis. *Quart. J. Roy. Meteor. Soc.*, **131**, 2961–3012, doi:10.1256/qj.04.176.

- Vallis, G. K., 2006: *Atmospheric and Oceanic Fluid Dynamics: Fundamentals and Large-Scale Circulation*. Cambridge University Press, Cambridge, U.K., 745 pp.
- Vallis, G. K. and E. P. Gerber, 2007: Local and hemispheric dynamics of the North Atlantic Oscillation, annular patterns and the zonal index. *J. Atmos. Sci.*, in press.
- Vallis, G. K., E. P. Gerber, P. J. Kushner, and B. A. Cash, 2004: A mechanism and simple dynamical model of the North Atlantic Oscillation and Annular Modes. *J. Atmos. Sci.*, **61**, 264–280.
- Williams, G. P., 2006: Circulation sensitivity to tropopause height. *J. Atmos. Sci.*, **63**, 1954–1961.
- Wittman, M., L. M. Polvani, and A. J. Charlton, 2007: The effect of lower stratospheric shear on baroclinic instability. *J. Atmos. Sci.*, **64**, 479–496, doi:10.1175/JAS3828.1.
- Yin, J. H., 2005: A consistent poleward shift of the storm tracks in simulations of 21st century climate. *Geophys. Res. Lett.*, **32**, L18701, doi:10.1029/2005GL023684.
- Yu, J.-Y. and D. L. Hartmann, 1993: Zonal flow vacillation and eddy forcing in a simple GCM of the atmosphere. *J. Atmos. Sci.*, **50**, 3244–3259.